Icarus 421 (2024) 116239

Contents lists available at ScienceDirect

Icarus

journal homepage: www.elsevier.com/locate/icarus

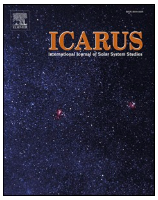

Crustal origin for olivine in the lunar Shioli crater ejecta boulders: Insights from the geological setting of Theophilus crater and Nectaris basin

P. Senthil Kumar [a,b,*], Abhisek Mishra [a,b], Vivek Krishnan [a,b], Netra S. Pillai [c], Sumit Pathak [d,e], Sriram S. Bhiravarasu [f], Shyama Narendranath [c], K. Jaya Prasanna Lakshmi [a], Satadru Bhattacharya [f]

[a] CSIR-National Geophysical Research Institute, Hyderabad, India
[b] Academy of Scientific & Innovative Research, Ghaziabad, India
[c] UR Rao Satellite Centre, Bengaluru, India
[d] Indian Institute of Technology, Kharagpur, India
[e] Department of Geology, Parul University, Vadodara, India
[f] Space Applications Centre, Ahmedabad, India

ARTICLE INFO

Keywords:
Moon
Impact cratering
Ejecta boulders
Theophilus crater
Shioli crater
Landing site analysis

ABSTRACT

On the Moon, impact craters and basins expose a wide range of crustal and mantle rocks that provide excellent opportunity for sampling them, understanding their origins and reconstructing spatial and temporal evolution of lunar interior. The previous studies detected olivine-bearing mantle rocks in and around large impact craters and basins. The Japanese SLIM mission landed on the ejecta of a ~ 280-m-diameter Shioli crater that was emplaced on the ejecta blanket of ~ 103-km-diameter Theophilus crater, for characterizing potential mantle-derived olivine in the Shioli crater ejecta boulders. To test this hypothesis, we studied the geological setting of Shioli crater, host Theophilus crater and Nectaris multi-ring basin using the orbiter data from Chandrayaan-1 and 2, Lunar Reconnaissance Orbiter, and Kaguya missions and the earth-based Arecibo radar observation. The asymmetrically distributed secondary craters and impact melt ponds around Theophilus crater suggests that a northeast-directed oblique impact produced this crater. Composition of Theophilus crater and surrounding region indicates that the crater excavated a heterogeneous target composed of a thin layer of high-Al olivine basalt (Mare Nectaris) underlain by anorthositic highland rocks possibly intruded by Mg-suite plutons; layers of Cyrillus crater ejecta blanket and Nectaris basin materials (both ejecta and impact melt sheets) were also present beneath the mare basalt flows. Hence, the Theophilus ejecta blanket is a mixture of all these materials. Our dating of Theophilus crater suggests that it is a ~ 2 Ga Eratosthenian crater. Shioli is a fresh simple crater that was formed at ~ 1 Ma on the uprange ejecta blanket of Theophilus, where the Arecibo radar data indicated the presence of abundant buried Theophilus ejecta boulders. An ESE-directed hypervelocity oblique impact event produced the elongated Shioli crater and its asymmetrically distributed bright ejecta. Shioli is a primary impact crater indicating the role of impact spallation processes associated with this hyper-velocity impact in producing thousands of ejecta (or spall) boulders around Shioli crater, displaying their asymmetric dispersal pattern and spatial variation of boulder sizes and shapes. The larger and elongated boulders are concentrated near the crater rim, while their size and axial ratio gradually decreases outward from the crater rim. The SLIM mission landed on a thin downrange ejecta of Shioli crater, where fewer large-size boulders are present. Our compositional study suggests that the Shioli ejecta boulders are composed of olivine basalt (Mare Nectaris) mixed with highland anorthositic fragments, including the reworked Cyrillus ejecta and Nectaris basin materials. The Shioli ejecta boulders were produced by complex impact fragmentation of already existing, buried Theophilus ejecta boulders. The regional crustal structure of Nectaris basin and its petrological composition suggest that both Nectaris basin and Theophilus crater did not excavate the lunar mantle. Therefore, the Shioli ejecta boulders are of crustal origin, including the olivine minerals present in them. Our results have important implications for the origin of olivine in the Shioli crater boulders being investigated by the SLIM mission.

---

* Corresponding author at: CSIR-National Geophysical Research Institute, Hyderabad, India.
E-mail address: senthil@ngri.res.in (P.S. Kumar).

https://doi.org/10.1016/j.icarus.2024.116239
Received 15 April 2024; Received in revised form 26 July 2024; Accepted 30 July 2024

1. Introduction

Since the formation of Moon, the entire lunar surface has been being bombarded by asteroids, comets and other impactors (e.g., the left-out moon-forming planetesimals), resulting in significant modification of primordial lunar crust. The long-lived bombardment produced impact craters and basins of diverse sizes and shapes: simple craters (bowl-shaped craters), complex craters (craters containing central peaks), flat-floored craters, peak-ring basins, multi-ring basins, and large impact basins. The simple craters are limited to a few kilometers in size, while the large impact basins reached a maximum size of several hundred kilometers. Depending on the size, these impact structures penetrated different depth levels in the lunar crust and mantle. For example, the largest simple crater excavated only an upper few hundred meters, while the largest basin (e.g., the South-Pole Aitken basin) excavated the entire lunar crust and even believed to have penetrated the lunar mantle (e.g., Potter et al., 2012). Thus, the impact craters and basins expose lunar rocks formed at different crustal and mantle depths, and thus they are windows into the lunar interior (e.g., Yamamoto et al., 2023). Interestingly, some large impact craters formed on the mare basalt areas also exposed the underlying highland crust on the crater interiors (e.g., Mustard et al., 2011). Similarly, some craters excavated the crypto-mare deposits that are concealed underneath the ejecta deposits of craters (e.g., Kaur et al., 2015). The impact structures exhibit a diverse mineralogical and geochemical composition reflecting a variation in the crustal and mantle petrology, and therefore provide a unique opportunity for understanding various crust and mantle forming petrological processes and reconstructing the geologic history of the Moon. On the other hand, the ejecta materials originated from the impact craters and basins ballistically travelled to a range of radial distances far away from the

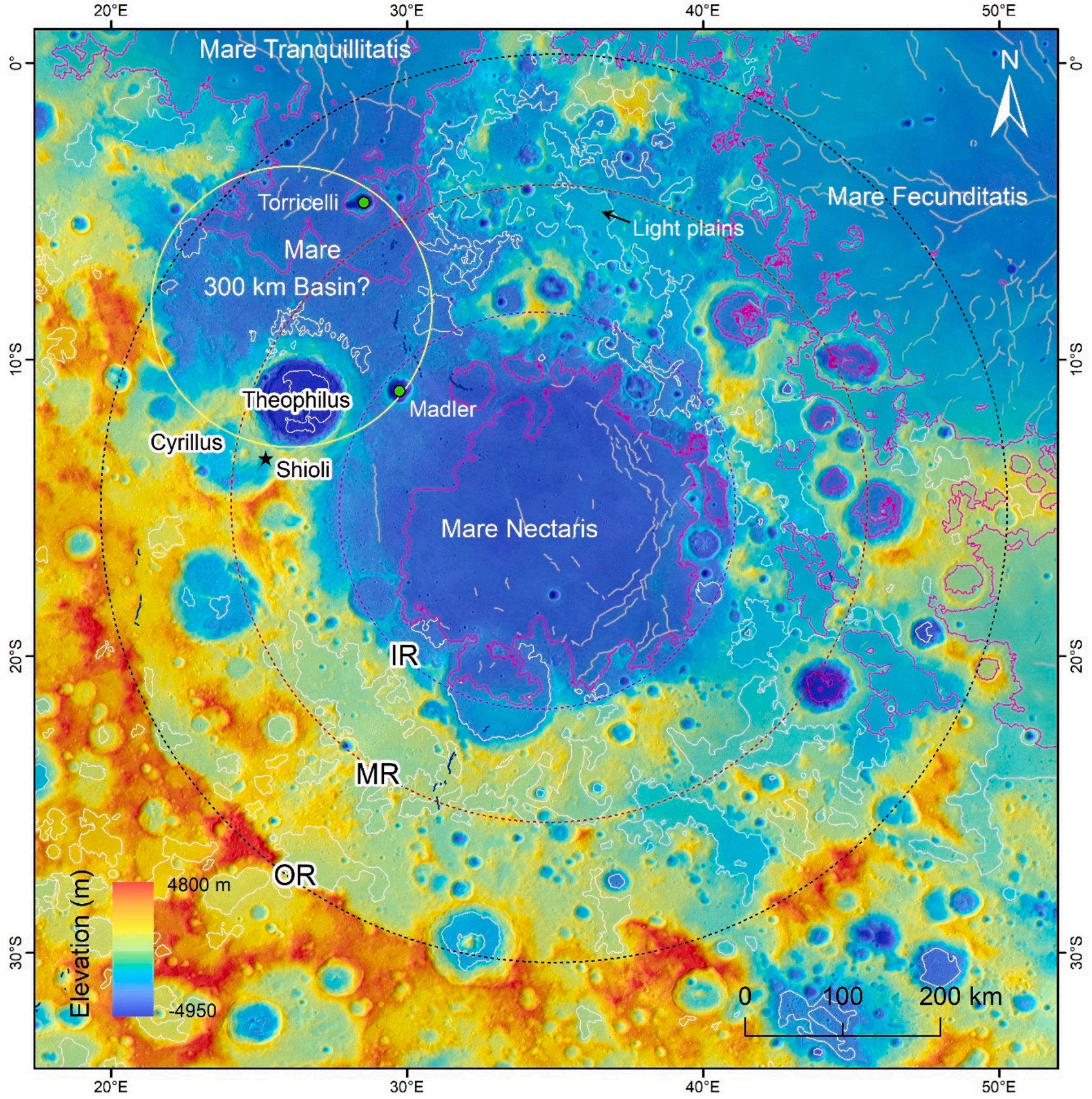

Fig. 1. Geological context map of Nectaris multi-ring basin showing Theophilus crater and Shioli crater. The Nectaris basin is composed of three rings (dotted circles): OR – Outer Ring, MR – Middle Ring and IR – Inner Ring. The Mare Nectaris is made up of basaltic flows with their boundaries are defined by pink polygons. The white polygons are global light plains mapped by Meyer et al. (2020). We inferred a ~ 300-km-diameter impact basin (yellow circle) in the north-western part of Nectaris basin, where it removed the highland materials, and is characterized by circular low crustal thickness anomaly (Fig. 34). Theophilus crater is located in the southern part of 300-km basin and postdates it; it also occurs between the MR and IR, in the north-western part of the Nectaris basin. Torricelli is an elliptical impact crater formed by high-angle oblique impact event, in which the projectile arrived from ENE-WSW direction. The LROC WAC image mosaic overlain by LOLA DEM data are in the background. (For interpretation of the references to colour in this figure legend, the reader is referred to the web version of this article.)

source craters. The ejecta materials emplaced from the simple craters are deposited within a few tens of kilometers range, while those from the large impact basins traversed the entire lunar surface. Hence, the ejecta deposits also provide unique opportunity for sampling the rock materials originated from different depth levels within the lunar crust and mantle.

As millions of impact structures were formed on the Moon since the Moon formation, the ejecta deposits from them covered the entire lunar surface, and formed the global mega-regolith layer overlain by a thin surface regolith layer (e.g., Richardson and Abramov, 2020). The global layer of surface regolith consists of ejecta materials of diverse sources, and are made up of finer lithic fragments, shock materials and agglutinates, that make up the upper few meters of the lunar mega-regolith (e.g., McKay et al., 1991). Though the surface regolith cover the entire lunar surface, large blocks of rocks, known as boulders, are also present on the lunar surface. A majority of these boulders are present on the ejecta blankets surrounding young impact craters (e.g., Bart and Melosh, 2010; Krishna and Kumar, 2016). The interiors of old craters and basins also produced boulders on the steep slopes due to later surface modifications caused by impact events, moonquake shaking and physical weathering (e.g., Kumar et al., 2016; Mohanty et al., 2020). Therefore, the fresh impact craters provide great opportunity to sample fresh ejecta boulders around them. Geological mapping of lunar surface showed spatial and temporal distribution of impact craters and basins and their ejecta materials (e.g., Wilhelms, 1987; Fortezzo et al., 2020) and some of these craters and basins (e.g., Copernicus, Imbrium and Nectaris) served as stratigraphic time markers of the lunar geologic history. The Apollo returned samples contained a diverse lunar regolith and rock materials originated from various sources, including impact craters and basins. Origins of rock samples collected from the landing sites, requires precise determination of provenance of these samples in terms of source impact structures (e.g., Petro and Pieters, 2006).

The global study of mineralogy and geochemistry revealed that the mare regions are made up of basaltic materials of diverse sub-groups, for example, low- and high-Ti basalts, low- and high-Al basalts, and olivine bearing picritic basalts (e.g., Lucey, 2004; Prettyman et al., 2006; Lemelin et al., 2019). These lava flows are characterized by emplacement ages ranging from 4 to 1 Ga, though some are shown to have emplaced in the last 100–50 Ma as well (Head et al., 2023). Similarly, the highland regions are composed of pure anorthosite, ferroan anorthosite, norite, gabbro, and other similar rock types (Jeffrey Taylor et al., 1991). Mg-suite of rocks (e.g., dunite, pyroxenite, periodotite and spinel-bearing rocks) are also found in the collections of Apollo samples (e.g., Shearer et al., 2015). The impact craters and basins occurring in the highland regions showed that the lunar crust and mantle are characterized by compositional variation with depth reflecting the petrogenetic processes in the lunar global magma ocean and subsequent mantle overturning (e.g., Elkins-Tanton et al., 2011; Moriarty III and Pieters, 2018). Since the Apollo, Luna and Chang-E programs, large quantities of lunar regolith and rocky materials were brought back to Earth from a diverse landing sites on the Moon. These materials contained mixtures of ejecta of diverse impact craters, ranging from the largest impact basin on the Moon (e.g., South-Pole Aitken basin) to centimetre to kilometer-scale impact craters (e.g., Copernicus) occurring in and around the sampling sites. The scientific importance of the returned samples depends on the provenance history of the rock materials collected at the sampling sites. The samples collected from the Apollo landing sites that are situated both on mare and highland areas showed a large diversity. Though the samples from the highland sites contained predominantly the local highland materials, they also contained samples from the adjoining mare basalt regions supplied by impact craters (e.g., Petro and Pieters, 2006). Hence, geological mapping is a fundamental science analysis that determines the provenance of samples collected at the landing sites and their relationship with various source craters or basins that are located globally on the Moon.

The Japan Aerospace Exploration Agency (JAXA) launched the Smart Lander for Investigating Moon (SLIM) mission on 6 September 2023, which landed on the lunar surface on 19 January 2024. The landing site is near the 280-m diameter Shioli crater, which was emplaced on the southwestern ejecta blanket of 103 km diameter complex crater, Theophilus (Fig. 1) (Ohtake et al., 2019). The previous studies suggested that the ejecta boulders of Shioli crater contain abundant olivine minerals that are interpreted to have originated from the lunar mantle (Ohtake et al., 2019). Wang et al. (2024) suggested that the Shioli ejecta materials in the SLIM landing site are composed of reworked Nectaris basin ring materials mixed with mantle rock materials. The Multi-Band Camera (MBC) onboard SLIM determines the composition of olivine in the Shioli boulders using the reflectance spectroscopic method (Nakauchi et al., 2019). It also determines the magnesium number of the olivine grains (Mg# = Mg/(Mg + Fe) atomic ratio) so that their crustal or mantle origins can be distinguished (e.g., Saiki et al., 2021). More importantly, the SLIM mission also demonstrated its capability to land on a hazardous surface containing abundant ejecta boulders of Shioli crater. Considering the geological setting of Shioli crater and its relationship with the host Theophilus crater, it is possible to determine whether the olivine-bearing ejecta boulders are products of impact excavation of lunar mantle or crustal rocks. It is a major objective of this study.

In this study, we carried out the context geological analysis of the SLIM landing site for understanding the origins of boulders and ejecta materials surrounding Shioli crater. We also characterized Theophilus crater and its ejecta to understand the provenance of Shioli crater materials. Understanding the regional geology of Nectaris multi-ring basin *vis-à-vis* Theophilus crater is also important to determine whether the Shioli crater materials are of crustal or mantle origins. Using the datasets from the Lunar Reconnaissance Orbiter, Kaguya, GRAIL, Chandrayaan-1, and Chandrayaan-2 missions and earth-based Arecibo polarimetric SAR data, we addressed the following outstanding questions in this work: (1) What are different morphological, mineralogical and geochemical characteristics of ejecta deposits and boulders in and around Shioli crater in general and at the SLIM landing site in particular? (2) What are the morphological, mineralogical and geochemical characteristics of the crater interior, ejecta deposits and secondary craters of Theophilus crater? (3) What is the stratigraphic relationship between Theophilus crater and Shioli crater? (4) What is the lithological composition of target materials that compose Theophilus and Shioli craters? (5) How does composition of these craters depend on the geology of Nectaris impact basin? (6) When did Theophilus and Shioli impact craters form? (6) What are the impact parameters and trajectories of impact events that produced Theophilus and Shioli craters? (7) What is the regional crustal structure underneath Nectaris basin and Theophilus crater? (8) Did Theophilus impact event excavate the lunar mantle? Finally, we provide important insights into the provenance of ejecta boulders of Shioli crater, as to whether these boulders were formed from lunar crust or mantle.

2. Geology of study area

The ejecta of Shioli crater was the landing target of the SLIM mission. Hence, an in-depth understanding of the geological setting of this crater is essential. Secondly, the location of Shioli crater suggests that the southwestern ejecta blanket of Theophilus crater was the target of Shioli impact event, indicating that the fragmental ejecta layer of Theophilus was involved in the Shioli cratering event. Therefore, geology of Theophilus crater and its relation to Shioli crater is also required to be understood. Thirdly, Theophilus crater is also related to the geology of Nectaris multi-ring basin as it was emplaced between the inner and middle basin rings of Nectaris (Fig. 1). The geological setting of Nectaris basin has been described by several workers (e.g., Whitford-Stark, 1981; Wilhelms, 1987; Spudis et al., 1989). The basin has three major rings: ~930 km diameter Outer Ring (OR), ~650 km diameter Middle Ring (MR) and ~ 400 km diameter Inner Ring (IR) (Fig. 1). The age of this

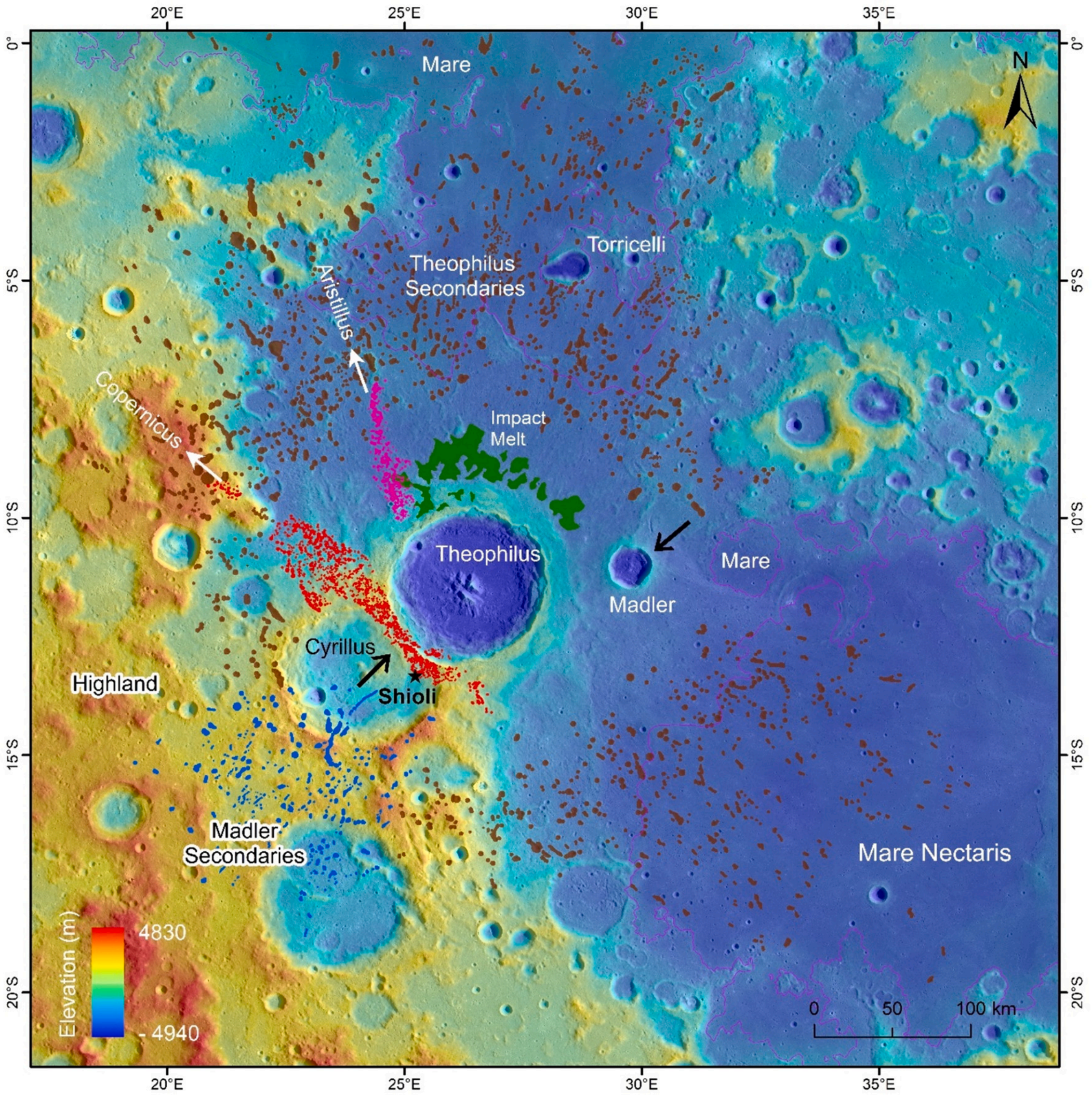

Fig. 2. Geological context map of Theophilus crater (diameter 103 ± 1.7 km) surrounded by its own secondary crater chains and clusters (brown polygons). The secondary crater chains of Copernicus crater (red polygons), Aristillus (pink polygons) and Madler (blue polygons) are superimposed on the Theophilus crater ejecta. The black arrows show the impact direction of Theophilus and Madler craters. The impact melt deposits produced by the Theophilus impact event (green polygons) are found between north-western and north-eastern part of Theorphilus crater ejecta blanket. Theophilus crater ejecta filled the interior of Cyrillus crater and postdates it. Madler crater is stratigraphically younger than Theophilus crater. The asymmetric distribution of secondary crater chains of Theophilus crater points to oblique impact origin for this crater, in which the projectile arrived from the south-western direction of the crater (see the direction shown by a black arrow). The north-eastern crater rim marks the downrange direction of the oblique impact event. (For interpretation of the references to colour in this figure legend, the reader is referred to the web version of this article.)

basin is also considered to be an important stratigraphic time marker that divides the Nectarian and pre-Nectarian periods. The age of this basin is found to be varying between different authors: 4.21 Ga (Baldwin, 1974), 4.07 Ga (Baldwin, 1987), 3.92 (Wilhelms, 1987), 4.10 Ga (Neukum, 1983), and 3.92 (Stöffler and Ryder, 2001), and Hiesinger et al. (2011) assigned the basin age to be 4.1 Ga, considering Neukum and Ivanov (1994) chronology system. The basin is highly degraded due to the superimposition of many large complex craters, flat-floored craters and simple craters, and the central basin floor is entirely embayed by the mare basalt flows (Mare Nectaris). Some of the large craters present on the Nectaris basin interior are Theophilus, Cyrillus, Catherina, Fracartorius, Piccomini, Gutenberg, Colombo, Santbech, Beaumont, and Madler. The global geological map of Fortezzo et al. (2020) showed that the highland surrounding the Mare Nectaris are overlain by the Nectaris basin ejecta deposits, including impact melt sheets, which are generally classified to be the Nectarian terra, plains, basin and crater units. These units are overlain by the ejecta materials and melt sheets from the Imbrium basin, which are generally classified to be the Imbrian terra, plains, basin and crater units. The Eratosthenian and Copernican aged impact craters and their ejecta materials are also superimposed on the highland and Mare Nectaris materials in the study area. The global lunar light plains are also found on the interior of Nectaris basin and the surrounding highland areas (Fig. 1; Meyer et al., 2020) and most of these light plains are impact melt sheets of Nectaris basin.

Theophilus and Cyrillus craters are located in the northwestern interior of the Nectaris basin. Theophilus crater is located between the IR and MR, and it overlies another complex crater Cyrillus, which is located to the southwest of Theophilus and is superimposed on the MR. The southwestern crater rim of Theophilus crater and its ejecta blanket fully buried the Cyrillus crater interior (Fig. 2). In the geological map of

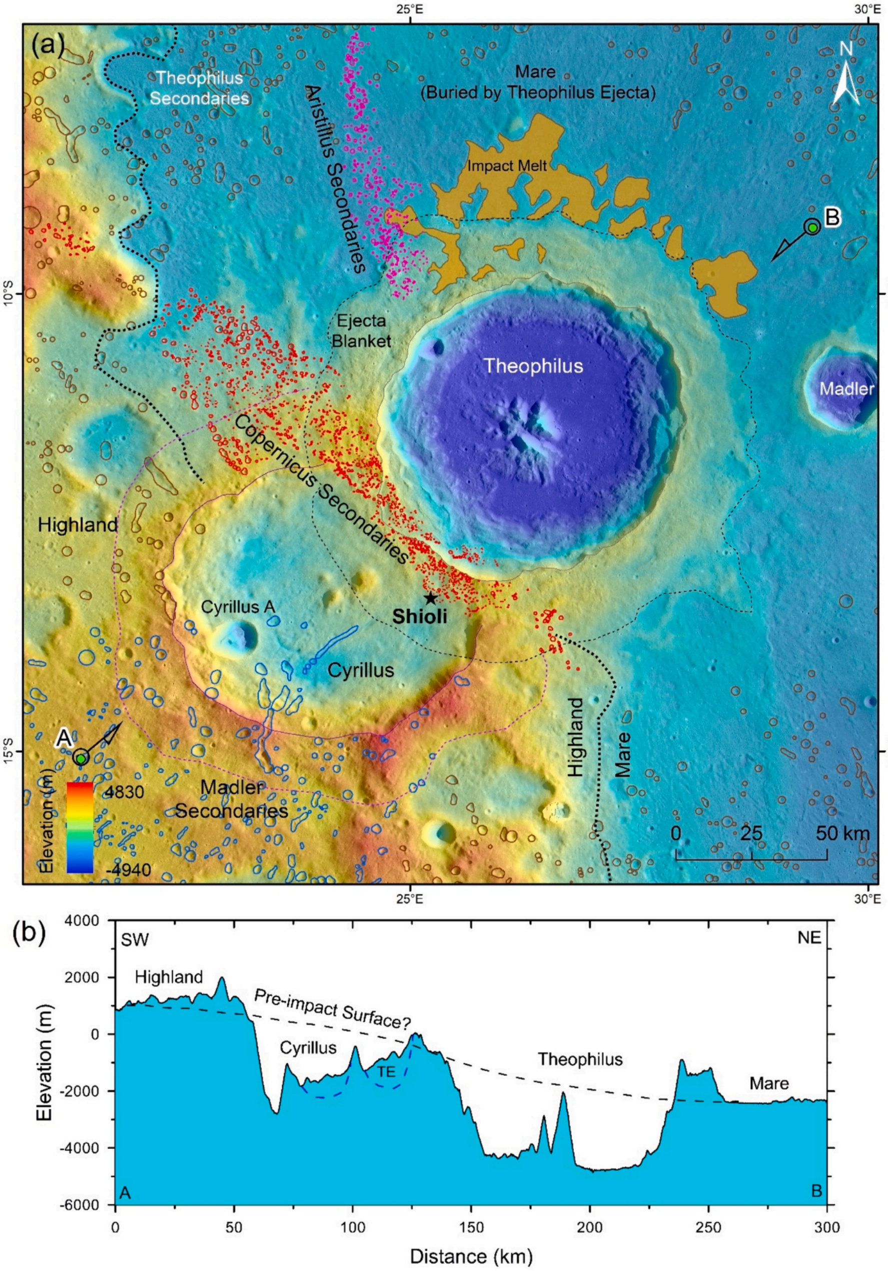

Fig. 3. (a) Geologic context map of Shioli crater showing its location at the south-western ejecta blanket of Theophilus crater. The impact melt deposits of Theophilus crater are found near its northern ejecta blanket boundary. A tentative contact between the highland and mare basalts is shown as thick dotted line. A tentative boundary of ejecta blankets of Theophilus and Cyrillus craters is shown as thin dotted line. While Cyrillus crater is superimposed on the highland-mare contact, Theophilus was fully formed in the mare region and its ejecta buried the mare surface. Cyrillus A is present on the Cyrillus floor and excavated the Theophilus ejecta. A topographic profile between the A and B was obtained. (b) A NE-SW oriented topographic profile between A and B (see Fig. 3a for location) shows the topographic characteristics of Theophilus and Cyrillus craters. The interior of Cyrillus crater was filled by Theophilus crater ejecta (TE). Theophilus crater interior is characterized by deeper and wider north-eastern crater floor when compared to the south-western crater floor.

Fortezzo et al. (2020), the crater materials of Cyrillus are shown to be of Nectarian age. Hence, these materials not only underlie Theophilus crater, but also the mare basalt flows (Imbrian age) in the Nectaris basin. Shioli crater is located on the southwestern ejecta blanket of Theophilus. Theophilus crater and its ejecta are shown to be Copernican crater materials in the geological map of the Moon by Fortezzo et al. (2020). However, it is shown to be an Eratosthenian crater by Wilhelms (1987). The central peak of this crater contains olivine, pyroxene, pure anorthosite and Mg-spinel bearing mafic rocks (Ohtake et al., 2009; Yamamoto et al., 2010; Pieters et al., 2011; Dhingra et al., 2011). Mg-spinel mineralogy was also detected on the floor and wall of this crater (Dhingra et al., 2011). These authors also confirmed the presence of shocked anorthosite. The mafic-free anorthosite was found to be the most dominant rock type that compose the central peak. Dhingra et al. (2011) suggested that the Mg-Spinel bearing lithology could have existed as a lateral unit in the target before the Theophilus impact. It was also found that the central peak containing hydroxyl absorption features, indicative of hydrous minerals or inclusions of magmatic water (e.g., Bhattacharya et al., 2015). The anorthosites, anorthositic norite, noritic anorthosites and norites were also suggested to be present in the highlands surrounding the Mare Nectaris (Spudis et al., 1989; Tompkins and Pieters, 1999).

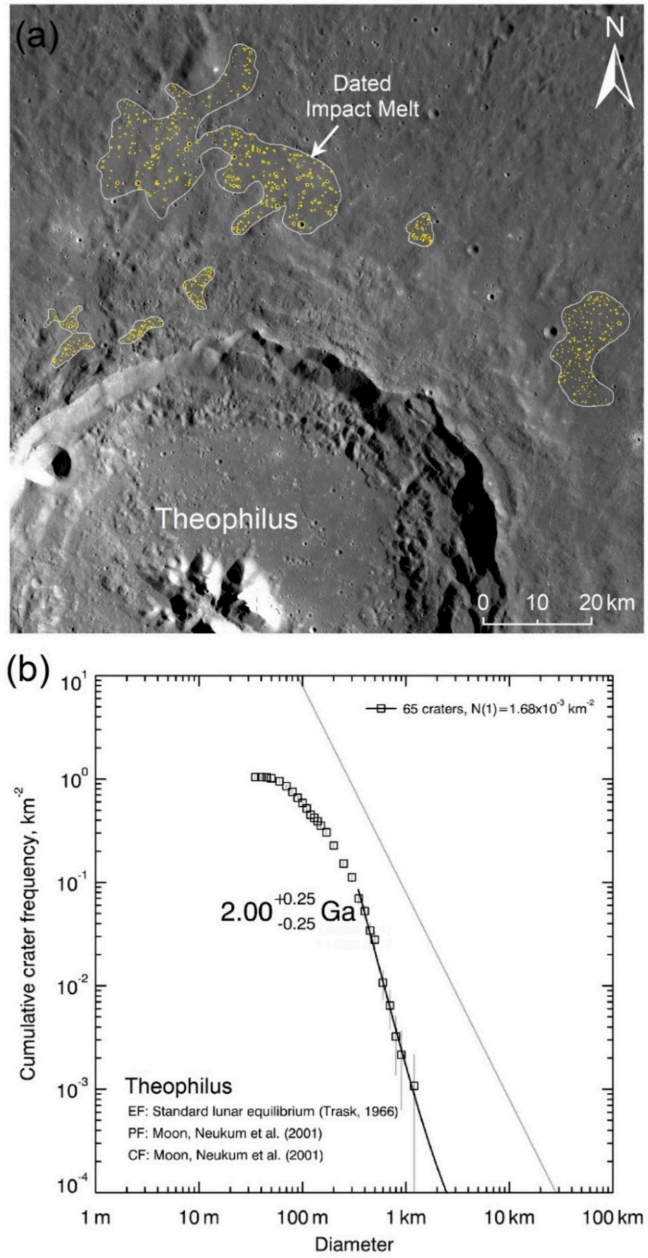

Fig. 4. (a) The Kaguya TC image mosaic showing the impact melt ponds (white polygons), where counting of superimposed impact craters was performed for determining the absolute formation ages of the ponds. (b) The cumulative size-frequency distribution of counted impact craters yielding an absolute model formation age of Theophilus impact crater to be 2 Ga, confirming that it is an Eratosthenian crater.

The central depression of the Nectaris basin is filled by mare basalt flows. A 300-km-diameter near-circular depression is also filled by the mare basalt flows that connect both the Mare Tranquiltatis and Mare Nectaris (Fig. 1). This circular depression may be a 300-km-diameter impact crater, comparable to the size of Schrödinger basin. The geological map of Fortezzo et al. (2020) showed that it is a Nectarian aged depression that may be filled by the ejecta and impact melt sheets of Nectaris basin, beneath the mare basalt top layer. De Hon (1974) determined the thickness of Mare Nectaris basalt flows based on the topography of mare filled craters. Approximately 1700 m thick basalt flows were suggested to be present at Torricelli crater. In the central part of Mare Nectaris, the flow thickness shown to be varying from 1000 to 1500 m, while along the Mare Nectaris boundary, the basalt thickness could be <500 m. Because the mare basalt units in the Mare Nectaris are contaminated by the ejecta rays and secondary craters from Theophilus, Madler and other craters, the Mare Nectaris basalt flows have not yet been dated by the previous workers so far, using the conventional crater counting method. Only the southern part of Mare Tranquilitatis, known as the T3 unit, was dated to be ~3.75 Ga (Hiesinger et al., 2000). Because this unit extends to the Mare Nectaris, we assign 3.75 Ga to be the age of the Mare Nectaris basalt flows and those surrounding Theophilus crater. Fortezzo et al. (2020) showed these basalt flows to be Imbrian mare, upper unit (Im2). Kramer et al. (2008) identified two distinct Nectaris mare units: the “Iltm” is an early Imbrian, low Ti, low Fe and high Al mare basalt unit, while the other “Imtm” is characterized by late Imbrian, medium Ti, medium Fe mare basalt unit. These authors suggested that high aluminium basalts are vastly present in the Iltm unit. Kaur et al. (2015) reported the presence of olivine minerals in the dark-haloed Beaumont L crater and many other nearby small fresh craters near the central part of Nectaris basin. Also, Corley et al. (2018) identified several mare basalt exposures containing olivine that are confined to the rims of many small craters (<5 km diameter), and the olivine was suggested to be a constituent of the mare basalt units. Several detections of olivine minerals from the Mare Nectaris suggests that the olivine mare basalt is the most predominant basalt type in the study area.

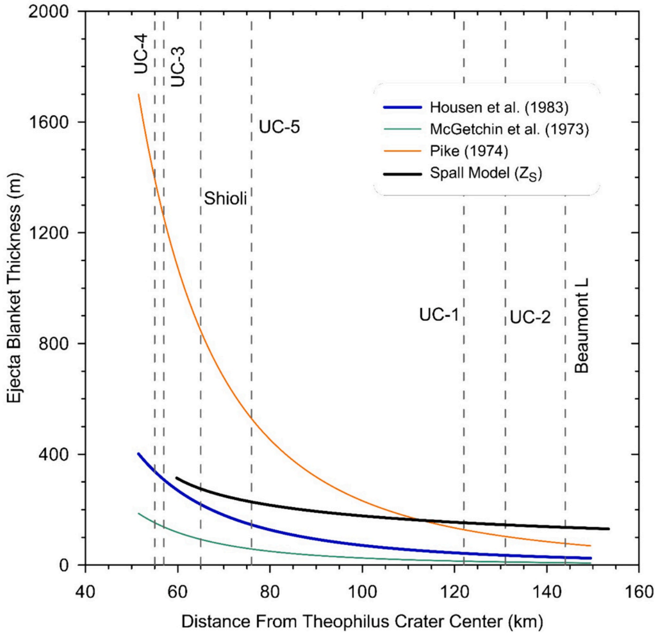

Fig. 5. Radial variation of ejecta blanket thickness of Theophilus crater as per equations provided by Housen et al. (1983), McGetchin et al. (1973) and Pike (1974). The thickness values (thick blue line) pertaining to Housen et al. (1983) are adapted in this work. Theoertical spallation model (estimated boulder size, Z_S) (Melosh, 1984) applied to Theophilus crater is also shown as black line. (For interpretation of the references to colour in this figure legend, the reader is referred to the web version of this article.)

3. Data and methods

3.1. Morphological studies

In this work, we carried out morphologic, mineralogic and geochemical analysis of the study area using the datasets from various missions. We used the 100 m/pixel Lunar Reconnaissance Orbiter Camera Wide Angle Camera (LROC WAC) image mosaic (Robinson et al., 2010) and 10 m/pixel Kaguya Terrain Camera (TC) panchromatic image mosaic (Haruyama et al., 2008) for performing geological analysis of Nectaris multi-ring basin, Theophilus, and Shioli craters. Lunar

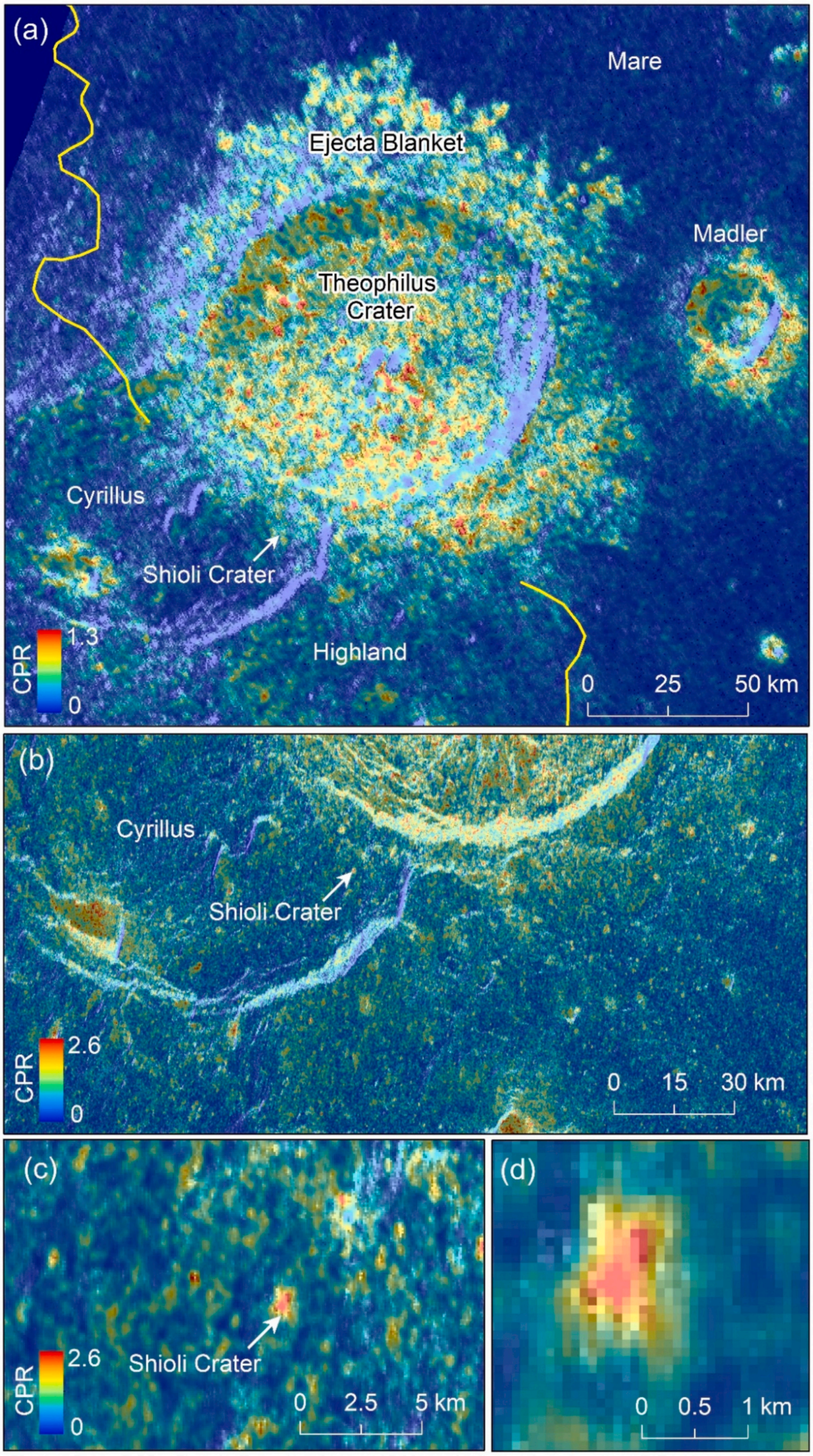

Fig. 6. Arecibo radar observations of Theophilus and Shioli crater regions: (a) A P-band Arecibo circular polarization ratio (CPR) map showing the blocky nature of Theophilus ejecta blanket. At Theophilus proximal ejecta, the blocks (boulders) are interpreted to be buried up to a few meters in the regolith and also in the underlying ejecta blanket, while those on the surface were already destroyed by micro-meteoroid bombardment. (b-d) S-band Arecibo CPR maps showing the blocky nature of Shioli crater. The elevated CPR values in and around Shioli crater is due to presence of thousands of boulders present on the ejecta blanket and crater interior.

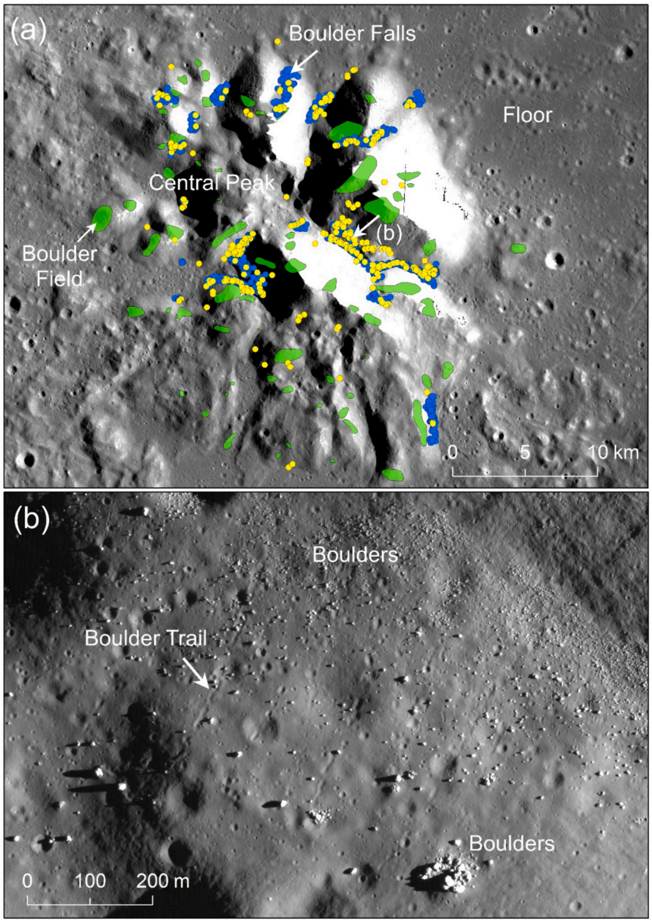

Fig. 7. (a) The Kaguya Terrain Camera mosaic showing the Theophilus central peak containing the boulder fields (green polygons). The yellow dots (not to scale) are boulder falls with trails, and blue dots (not to scale) are boulder falls without trails. (b) A close view of boulder falls on the central peak walls. More than one generation of boulder falls are recognized. The LROC NAC image M192774546LE is in the background. See Fig. 7a for the location of the boulder fall site at the central peak. (For interpretation of the references to colour in this figure legend, the reader is referred to the web version of this article.)

Reconnaissance Orbiter Camera Narrow Angle Camera (LROC NAC) images were used for studying the morphology of Shioli crater. Similarly, the Kaguya TC image mosaic was used for dating of the Theophilus crater impact melt ponds. The 0.25 m/pixel Orbiter High Resolution Camera (OHRC) images (Chowdhury et al., 2020) obtained by Chandrayaan-2 Orbiter were used for studying the morphology and mapping of the ejecta boulders in and around Shioli crater. For morphometric analysis, we used 512 pixels per degree merged Kaguya-LOLA digital terrain model (Barker et al., 2016). ESRI's ArcGIS desktop software was used for geological and topographic analysis. We used the lunar crustal thickness map (model 1) derived from the inversion of Bouguer gravity anomalies obtained by the Gravity Recovery and Interior Laboratory (GRAIL) mission (Wieczorek et al., 2013).

3.2. Mineral detections

We used the mineral abundance maps of plagioclase, clinopyroxene, orthopyroxene, olivine, and FeO derived from the Kaguya Multiband Imager (MI) and Spectral Profiler (SP) data (Lemelin et al., 2019). We also derived mineralogical information from the Chandrayaan-1 Moon Mineralogy Mapper (M^3) data with a spatial resolution of ~140 m/pixel (Goswami and Annadurai, 2009; Green et al., 2011). To understand the mineralogical diversity in the study area, a false colour composite (FCC) image was generated by assigning the red, green and blue channels to the 930 nm, 1249 nm and 2149 nm of M^3 bands, respectively. This FCC image highlights the presence of pyroxenes in green shade, olivine exposures in light to dark brown shade and spinel in yellowish to orange shades. The representative reflectance spectra of the associated minerals in the study area have been clipped at 2500 nm to overcome the effect of thermal residue at the higher wavelengths. Furthermore, to study the relative strength of the spectral absorption features near 1000 and 2000 nm, an integrated band depth (IBD) image was generated by following Mustard et al. (2011). To depict the first-order mineralogical variations in the study area, a FCC image was prepared using 1000-nm IBD, 2000-nm IBD and 1578-nm M^3 albedo band in the red, green and blue channels, respectively. The pyroxene-bearing outcrops exhibit hues ranging from pink to magenta on the IBD map, while olivine is represented by shades of orange and spinel by greenish tones. In order to enhance the distinction between the mineralogical compositions of lunar mafic rocks in the study area, a rock-type composite map (RCM) was prepared by following Pieters et al. (2014). This map represents areas containing pyroxene, spinel, and plagioclase minerals, represented by shades of red to pink, green, and blue, respectively. The derived maps offer useful information regarding the mineral distribution to select the region of interest (3 × 3 pixels) in the study area to acquire the mean reflectance spectra for further spectroscopic analysis.

3.3. Geochemical data

We used Chandrayaan-2 Large Area Soft X-ray Spectrometer (CLASS) data to get the weight percentage of different elements such as Al, Fe, Mg. The CLASS payload is a non-imaging spectrometer that measures the Moon's X-ray Fluorescence (XRF) spectra and detects these elements by measuring the characteristic X-rays that are emitted by the lunar surface, when excited by the solar X-ray emission. The CLASS detector has the ground resolution of 12.5 km × 12.5 km at the 100 km altitude lunar orbit (Radhakrishna et al., 2020; Narendranath et al., 2024).

3.4. Radar data analysis

We utilized the Arecibo 12.6 cm (S-band) and 70 cm (P-band) radar data (Campbell et al., 2007, 2010) to understand the physical properties of the Theophilus and Shioli crater regions. The radar backscatter is composed of both (a) a specular component from both the space-surface interface as well as subsurface layers in the crater floor and ejecta, and (b) a diffuse component caused by surface and subsurface rock fragments, especially the rock boulders (Thompson et al., 2011). The Arecibo transmits circularly polarized waves and receives echoes from the lunar surface at the Arecibo observatory (for P-band) as well as the Green Bank Telescope (for S-band) that are in both senses of circular polarization. The received echoes in the opposite sense as that transmitted waves (OC or "polarized") arise in part from mirror-like echoes from the large, flat (≥ 10 radar wavelengths) smooth surfaces, with some component due to diffuse reflections (at larger incidence angles). The echoes in the same sense as that transmitted (SC or "depolarized") are attributed to scattering from wavelength-sized (one-tenth to 10 wavelengths) rock boulders, present either on the lunar surface or buried in the subsurface up to the radar's penetration depth, which is on the order of ten wavelengths in the maria and up to forty wavelengths in the highland regions (Campbell and Hawke, 2005). The received radar echoes at a particular wavelength represent the depth-integrated regolith properties over the radar path length (e.g. Thompson et al., 2011), and the relative contribution of each of these components as a function of radar wavelength, surface roughness, surface and volume rock boulder populations, the depth and dielectric properties of the regolith and bedrock (e.g. Ghent et al., 2005). The circular polarization ratio (CPR), which is a ratio of the SC and OC echoes, provides a robust measure of roughness (or boulder abundance) at the lunar surface or sub-surface within the probing depth of the radar signals.

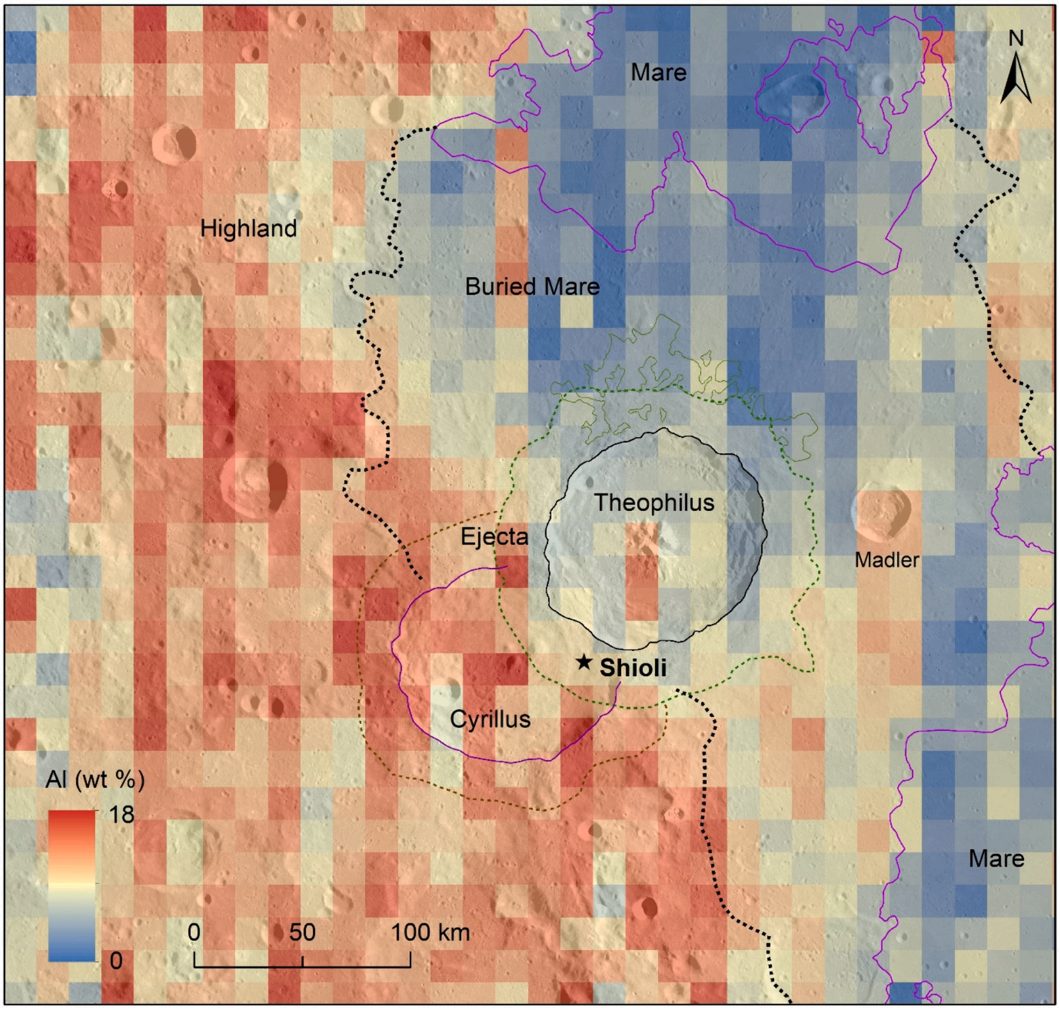

Fig. 8. A map showing the variation of aluminium (wt%) abundance in the study area, derived from the Chandrayaan-2 CLASS data. The highland area is characterized by higher abundance of aluminium compared to the mare basalt areas. The Kaguya TC image mosaic is in the background.

3.5. Crater counting ages

The formation ages of Theophilus crater impact melt ponds and Shioli crater ejecta blanket were determined using the conventional crater counting method. It involves demarcation of crater counting area and measurements of diameters of superimposed primary impact craters on the ejecta blanket or melt ponds within the counting area. We used the *CraterTools* software for mapping the craters within the given counting areas (Kneissl et al., 2011). We used Kaguya Terrain Camera (TC) images for dating the Theophilus crater impact melt ponds and Chandrayaan-2 Orbiter High Resolution Camera (OHRC) images for dating the Shioli crater ejecta blanket. The crater counting data (.scc files) were then imported into the *Craterstat* software (Michael and Neukum, 2010), for performing the statistical analysis of the mapped craters and deriving the cumulative size-frequency distributions (CSFDs) of the mapped craters. The lunar production and chronology functions (Neukum et al., 2001) were applied for obtaining the absolute model ages.

4. Results

4.1. Study of Theophilus crater

4.1.1. Morphology of Theophilus crater

Theophilus is a typical complex crater characterized by a near-circular rim, terraced wall, flat floor with a central peak complex (Figs. 2 and 3). An average rim-to-rim diameter of Theophilus is ~103 ± 1.7 km, rim-to-floor depth is ~4.1 km, and central peak height is ~2.5 km above the surrounding floor. The radial width in the northeastern crater floor is ~26 km, while it is ~20 km in the southwestern side. Hence, the central peak is shifted towards the southwestern rim. The central peak is also split into four unequal blocks, in which the northern block is massive and curved with its concave side facing the northeastern rim. The southwestern floor is at a higher elevation (~200 m) than at the northeastern floor. The northeastern floor is smooth because of a pool of impact melt, produced by the Theophilus impact. The northeastern crater rim is about ~800 m lower than the southwestern rim, suggesting that the crater was formed on the target surface having a slope towards northeast (Fig. 3b). A 7 km diameter simple impact crater was emplaced on the northwestern crater wall. Theophilus crater is surrounded by a well-developed ejecta blanket that extends to an average radial distance of ~25 km from the rim. Beyond this distance, the ejecta blanket is less conspicuous but has many radial lineaments and subtle grooves on the surface that extend up to a radial distance of ~50 km from the outer edge of ejecta blanket. The impact melt ponds of variable sizes and shapes, produced by the Theophilus impact, are observed in the zone surrounding the ejecta blanket, while larger impact melt ponds are found along the northern periphery (Fig. 3a). These ponds are characterized by smooth and flat surfaces exhibiting embayment relationship with the surrounding ejecta materials.

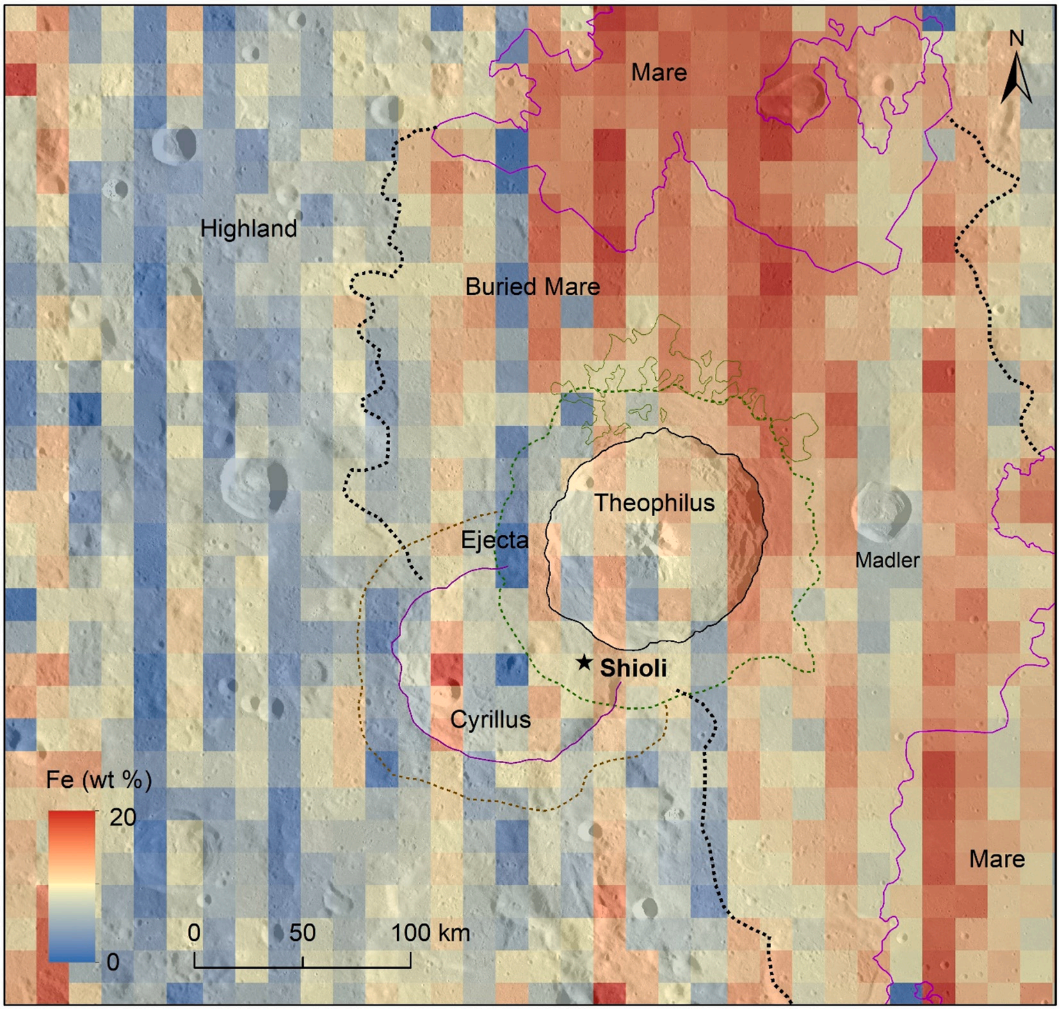

Fig. 9. A map showing the variation of iron (wt%) abundance in the study area, derived from the Chandrayaan-2 CLASS data. The mare basalt areas are characterized by higher abundance of iron than the highland areas. The Kaguya TC image mosaic is in the background.

The secondary craters of Theophilus are found beyond 50–75 km radial distance from the crater rim. We mapped >2000 secondary craters around the Theophilus ejecta blanket, displaying an overall asymmetry in their distribution pattern (Fig. 2). These craters occur in the form of clusters and chains. The shapes of secondary craters are elongated towards Theophilus crater. The asymmetric distribution of secondary craters suggest that Theophilus crater was formed by an oblique impact event. A lack of secondary craters in the southwestern side of the ejecta, defines the forebidden zone, suggesting that it is the uprange side of the oblique impact. In the northeastern side, the secondary craters are found up to a distance of >350 km, while in the southeastern and northwestern parts, they traversed up to ~300 km and ~ 250 km, respectively. The asymmetric distribution of secondary craters, shifting of central peak position towards the southwest crater rim, the concave curvature of central peak opening towards the northeastern rim, and the distribution of impact melt ponds are consistent with the northeast-directed oblique impact event.

The 28 km diameter Madler crater is located about 50 km east of Theophilus crater rim. The ejecta blanket of this crater overlies the ejecta of Theophilus crater and hence it postdates Theophilus crater. The secondary craters of Madler are notably superimposed on the southwestern (uprange) ejecta of Theophilus and we mapped ~300 craters of them; these are generally distributed as a broad cluster oriented in NE-SW direction (Figs. 2 and 3). To the northeast of Madler, its ejecta developed a chevron-shaped forebidden zone, suggesting southwest-directed oblique impact. A large number of secondary crater chains from distant primary craters traverses the Theophilus crater ejecta. We mapped >1500 secondary craters of Copernicus crater that are superimposed on the southwestern ejecta of Theophilus (Figs. 2 and 3) and these form a chain oriented in NW-SE direction for a length of ~300 km and a width of ~50 km. We also traced a linear cluster of >300 secondary craters of Aristillus crater on the northwestern ejecta of Theophilus (Figs. 2 and 3) and these are aligned in NNW-SSE direction, for a distance of >100 km.

4.1.2. *Age of Theophilus*

An outstanding question of whether Theophilus is a Copernican or Eratosthenian crater is remain unresolved. Therefore, we dated the surfaces of six impact melt ponds (Fig. 4a), which may provide the formation age of Theophilus crater. The previous studies suggested that dating of impact melt deposits of impact craters may provide more reliable ages than the fragmental ejecta surfaces (e.g., Hiesinger et al., 2011). Theophilus crater and its ejecta blanket are superimposed by many small fresh impact craters containing radial bright ejecta rays, suggesting that these are primary impact craters. We counted these craters from the selected counting areas covering the impact melt ponds on the ejecta blanket. Because the secondary craters of Copernicus, Aristillus, Madler, and Cyrillus A are also superimposed on Theophilus crater ejecta (Figs. 2 and 3), we carefully eliminated these secondary craters while counting the primary craters. We counted 974

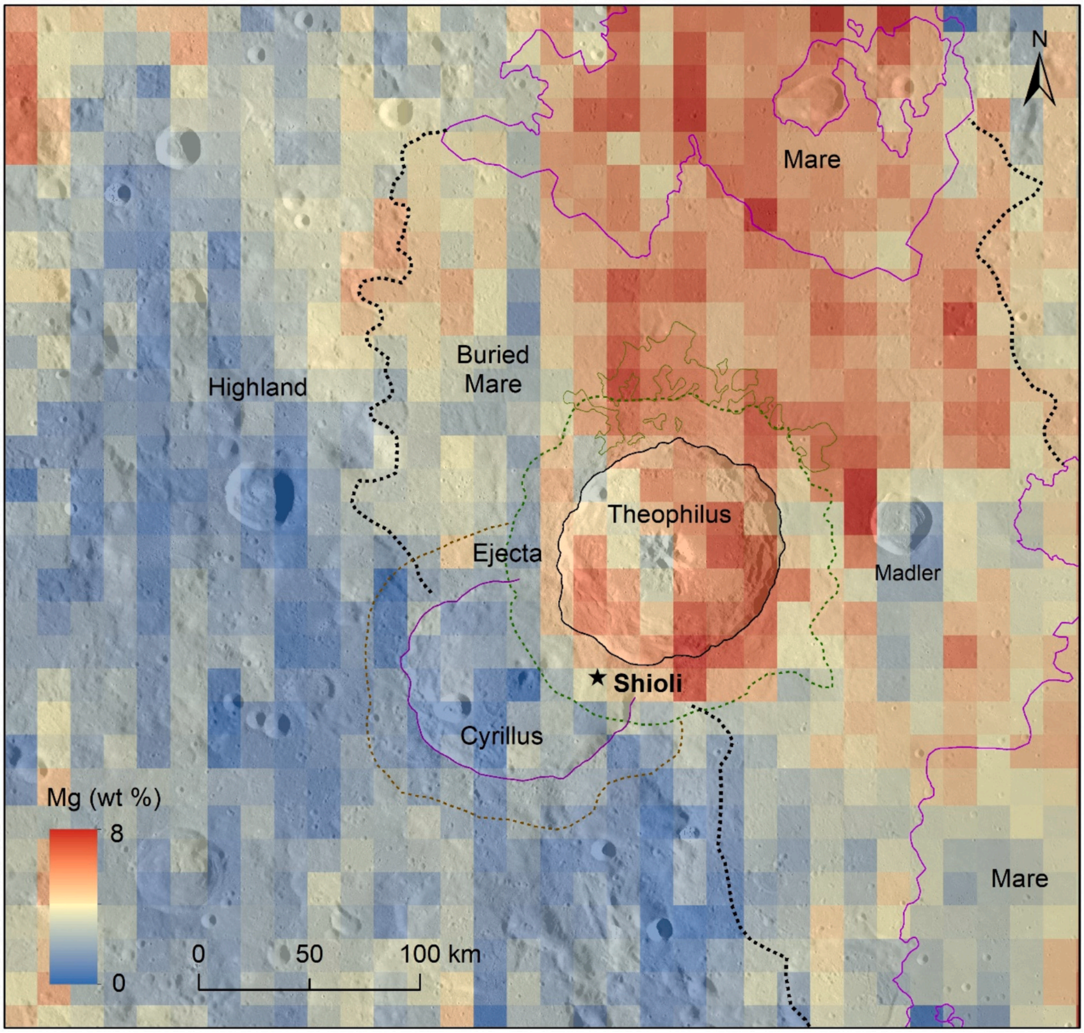

Fig. 10. A map showing the variation of magnesium (wt%) abundance in the study area, derived from the Chandrayaan-2 CLASS data. The mare basalt areas have higher magnesium content than the highland areas. The Kaguya TC image mosaic is in the background.

superimposed impact craters in the diameter range of 38.6 m to 1.23 km from a total counting area of 941.2 km^2 covering the six impact melt ponds. The cumulative size-frequency distribution of the counted craters is shown in Fig. 4b. We fitted an isochron to a diameter range of 350 m–1.23 km, which yielded a N (1) value of 1.68×10^{-3} and an absolute model age of 2 ± 0.25 Ga, which suggests that Theophilus is an Eratosthenian crater, as earlier suggested by Wilhelms (1987).

4.1.3. *Ejecta thickness*

Theophilus crater has a rim height of ~2 km above the surrounding plains, accounting for rim upliftment and ejecta blanket thickness. A gradual decrease of elevation from the crater rim towards the edge of ejecta blanket indicates a gradual decrease of both rim uplift and ejecta thickness. Because the ejecta thickness variation cannot be measured directly, we calculated it using various empirical equations given by Pike (1974), Housen et al. (1983) and McGetchin et al. (1973) (see Supporting Information). The plots are shown in Fig. 5. As per Pike (1974) model, the ejecta thickness at the crater rim is 1700 m, which gradually decreases to 865 m at a distance of Shioli crater. On the other hand, the model by Housen et al. (1983), simplified by Petro and Pieters (2006), suggests a thickness of 402 m at the crater rim which decreases to 223 m at the Shioli crater. The model by McGetchin et al. (1973) gives the lowest estimate of 186 m at the crater rim and 95 m at the Shioli crater. Therefore, considering the three models, thickness of ejecta blanket of Theophilus crater at the distance of Shioli crater would vary between 95 m and 865 m. However, many workers suggested that the model by Housen et al. (1983) is more suitable to complex impact craters (e.g., Ivanov et al., 2018; Krasilnikov et al., 2023). Therefore, the ejecta thickness of 223 m for Theophilus crater may be considered beneath Shioli crater.

4.1.4. *Buried and exposed boulders*

The polarimetric radar observations provide important insights into the nature of ejecta blanket surrounding the Theophilus crater, especially the presence of ejecta boulders, both on the ejecta surface and buried in the subsurface (Fig. 6). A previous study using 70-cm wavelength radar observations of Theophilus crater indicated very strong depolarized (SC) echoes with echo strengths an order of magnitude larger than the surrounding plains (Thompson, 1987). Fig. 6 shows the P- and S-band CPR maps of Theophilus crater and the surrounding ejecta. Both the crater interior and ejecta blanket are characterized by high backscattered power and high circular polarization ratios (Fig. 6), implying abundant rocky ejecta either on the surface or buried within the penetration depth of the radar. While vast areas on the crater floor have the P-band CPR values >1, some regions have average CPR values in the range of 0.5–0.6, coinciding with the impact melt ponds in the northeastern floor. The high interior S- and P-band CPR values are attributed to the presence of numerous small fresh impact craters as well

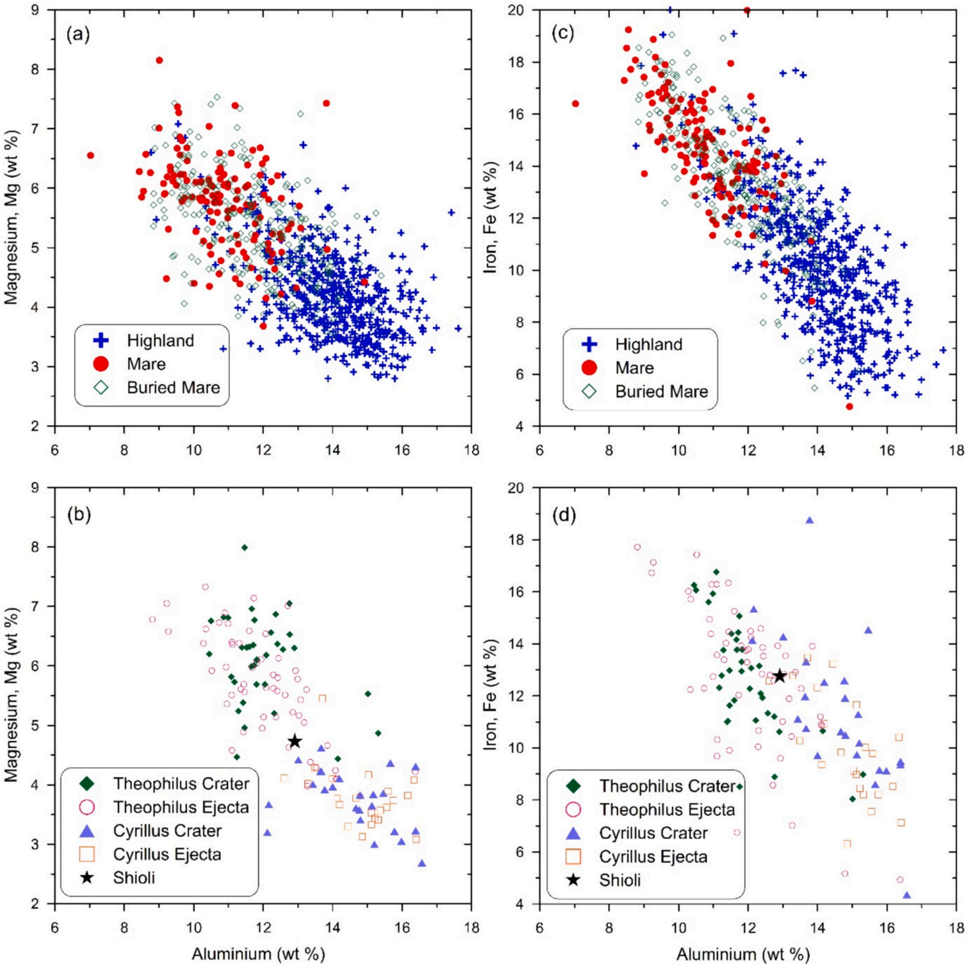

Fig. 11. Correlation between different elemental abundances of various geological units such as highland, mare, buried mare, Theophilus crater and its ejecta blanket, Cyrilus crater and its ejecta blanket, and the area covering the Shioli crater, as defined in Figs. 6 to 8. The highland pixels are characterized by higher Al, lower Fe, and lower Mg contents compared to the mare basalt pixels. The buried mare pixels are more similar to the exposed mare basalt pixels. Interestingly, the pixels covering Cyrillus crater and its ejecta blanket are comparable to the highland, while Theophilus crater and ejecta blanket are characterized by higher Mg and Fe than Cyrillus.

as boulder fields and boulder falls containing rolled boulders with a minimum diameter of about one-tenth of the radar wavelength and larger (Fig. 7). Our study of Kaguya TC and LROC NAC images provided a map of boulder fields and boulder falls on the central peak of Theophilus crater (Fig. 7). Considering the mineral detections from the central peak (e.g., Dhingra et al., 2011), these boulders may contain minerals such as olivine, pyroxene and Mg-spinel. Some boulders may be composed of pure anorthosite as well. The crater wall also contains some sporadic occurrences of boulder fields, locally occurring debris flows and boulder falls.

In the P-band data (Fig. 6a), the Theophilus ejecta blanket is characterized by high CPR values similar to those in the crater interior, reaching as high as 1.3. Shioli crater is located within the Theophilus ejecta blanket and is associated with higher S- and P-band CPR values (Fig. 6a-d). Moreover, P-band radar data reveals that the proximal ejecta blanket associated with Theophilus crater has distinctly higher CPR values (in the range of 0.5–1.3) than the background regolith when compared to the S-band radar data (Fig. 6a). For example, the south-eastern ejecta blanket of Theophilus has higher (>1) CPR values (along with enhanced SC backscatter) that grades into low CPR values on the surrounding plains at a radial distance of ~40 km from the Theophilus crater rim, indicating the radial extent of ejecta blanket. In other parts of the ejecta blanket, the transition occurs between 25 and 35 km (Fig. 6a). Our examination of LROC WAC and NAC images in the Quickmap browser revealed absence of boulders on the surface of Theophilus ejecta blanket. Thus, the enhanced CPR should originate from the subsurface. The radar data suggest significant diffuse scattering of radar waves in the ejecta possibly due to a significant component of subsurface volume scattering from the buried ejecta boulders. The dry lunar regolith within the Theophilus ejecta blanket would permit greater radar penetration and volume scattering, enhancing the probability of subsurface multiple scattering events that further increase the CPR values, as observed. Therefore, ~100–400 m thick ejecta blanket around Theophilus crater contributes to high CPR values, especially due to the buried ejecta boulders that were deposited during the Theophilus cratering event. Beyond 25–40 km radial distance from the crater rim, high CPR values gradually decreases to low CPR values (<0.3) in the surrounding distal ejecta deposits. Interestingly, the CPR values are low in the impact melt ponds that occur along the northern ejecta blanket (Fig. 3) and are indistinguishable from the background regolith. Similar to Theophilus crater, the Madler crater interior and its ejecta blanket are also characterized by high P-band CPR values (>1). We noticed fewer boulders on the Madler ejecta blanket surface. Therefore, high CPR values observed from its ejecta blanket are interpreted to be related to the buried boulders. In contrast, the central peak of Madler is characterized by many boulder fields on the surface, giving rise to elevated high CPR values. It is also noted that Cyrillus crater and the surrounding ejecta are characterized by low CPR values, indicating paucity of boulders both on surface and subsurface.

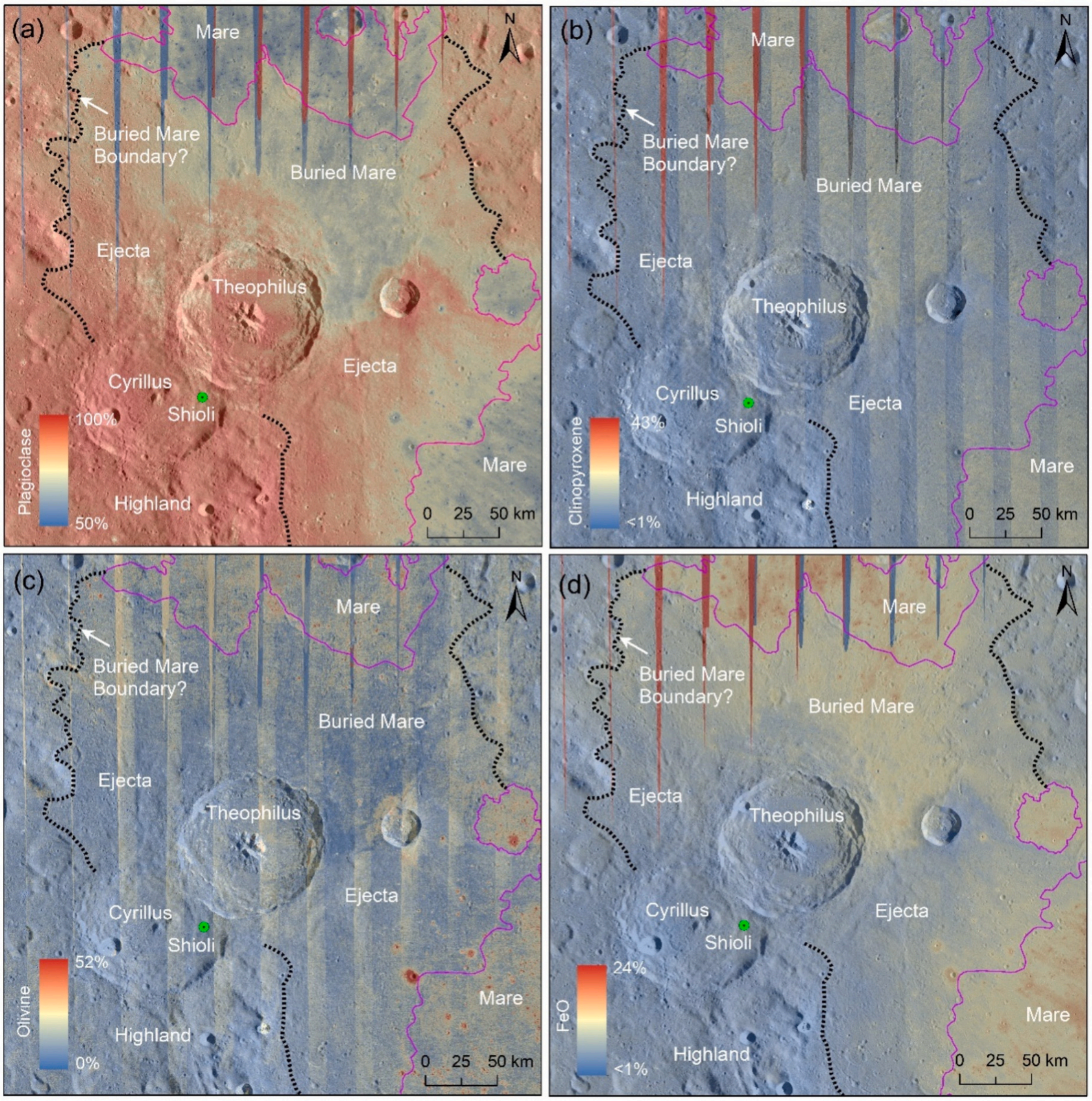

Fig. 12. Kaguya mineral maps of the study area: (a) plagioclase, (b) clino-pyroxene, (c) olivine and (d) FeO contents in various geological units in the study area.

4.1.5. The geochemical maps

Using the CLASS data, we prepared the elemental abundance maps of Al, Fe and Mg for the study area (Figs. 8–10). These elemental abundances reflect the composition of the lunar regolith and the underlying bedrocks. In many cases, the locally formed regolith is mixed with the ejecta from the craters and basins occurring at different distances. The ejecta from young impact craters also bury the regolith layer, leading to formation of a new regolith layer on top of the underlying regolith. The interior of craters and basins exposes fresh bedrocks. Therefore, the elemental maps not only provide compositional information about the local bedrock but also the ejecta deposits ballistically derived from various impact craters. Hence, the interpretation of CLASS elemental maps requires an in-depth understanding of local and regional geology that takes in account of stratigraphic relations between the ejecta materials of diverse impact crater sources and the insitu rock types (e.g., basalt and anorthosite). We interpret the CLASS elemental maps in terms of lithology using the geochemical data obtained from various Apollo returned lunar rocks (Table S1; Fig. S1). The mineralogical maps derived from the Kaguya multispectral and Chandryaan-1 M^3 hyperspectral datasets were also used. The CLASS elemental maps of the study area are divided in to eight morphological units as per Figs. 2 and 3. These units are: highland, mare, buried mare, Theophilus crater, Theophilus ejecta blanket, Cyrillus crater, Cyrillus ejecta and Shioli crater. The variation of Al, Fe and Mg abundances within these units and the mean elemental abundances (Table S1) were studied for understanding the nature of lunar source rocks that make up these units.

The elemental maps (Figs. 8–10) of the Mare Nectaris plains and the buried mare units (crypto mare) are characterized by lower abundances of Al and higher abundances of Fe and Mg than the surrounding highlands. The pixels covering the mare basalt and buried mare basalt units have comparable mean abundances of 10.9–11.7% Al, 13.5–14.7% Fe and 5.3–5.8% Mg, respectively. Strikingly, these mare units have higher abundances of Al compared to the typical mare basalts elsewhere on the Moon (Table S1). The mare basalt units in the study area are similar to the very low-Ti, high aluminium basalts in the Apollo 16 collections (sample # 60053,2–9; Zeigler et al., 2006). This is consistent with the study by Kramer et al. (2008) that showed a majority of areas covering the Mare Nectaris is composed of the map unit “Iltm” which is interpreted to be a candidate rock type typical for Early Imbrian, low-Ti, low-Fe and high-Al basalt. Fig. 11 reveals the overall elemental distribution within the mare and buried mare basalt pixels. Though these units are comparable to each other in terms of overall elemental distribution, a

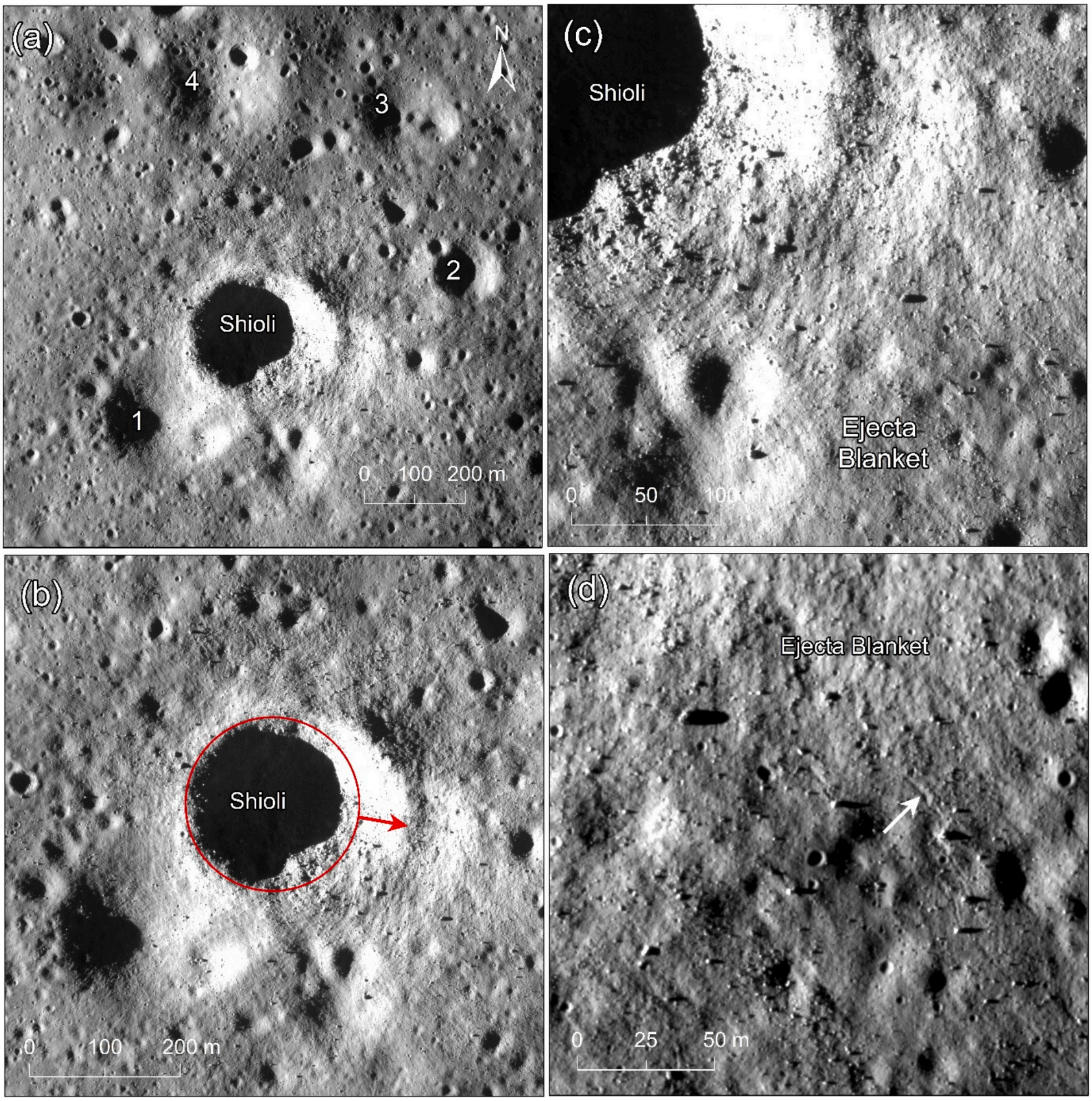

Fig. 13. Morphological characteristics of Shioli crater. The OHRC image (20210401T235737–6656) is in the background. (a) Superimposition of Shioli crater on another similar sized crater (1) and the Shioli ejecta blanket fills the interior of this crater. The Shioli crater ejecta and boulders are found on the interiors of other prominent craters (2, 3 and 4) in the vicinity. (b) A close view of Shioli crater and the underlying degraded crater to the southwest. The ejecta blanket of Shioli partially fills the interior of degraded crater. A red-circle fitted to the crater rim suggests that its shape deviates from the circularity with an elongation roughly towards east, indicating an oblique impact towards E or ESE. Also, the E to ESE crater wall is more diffusive than the western rim, where it is crisp. (c) The southeastern part of the Shioli crater showing diffusive crater rim and well-developed ejecta blanket overlain by boulders. (d) The south-eastern ejecta blanket of Shioli showing the ejecta boulders and associated trails (also see Mohanty et al., 2023). (For interpretation of the references to colour in this figure legend, the reader is referred to the web version of this article.)

significant number of pixels from both units have greater Fe (15–20%) and Mg (6–8%) compared to the mean elemental abundances. These pixels are considered to be the original mare surfaces with the least contamination from the ejecta deposits from the nearby highland craters. The Kaguya mineral maps (Fig. 12) suggest that the mare and buried mare units consist of mineralogical assemblage typical of olivine basalts (e.g., Lemelin et al., 2019; Kaur et al., 2015; Corley et al., 2018). On the other hand, some pixels are comparable to the highland pixels (12–14% Al, <12% Fe and < 5% Mg) indicating some contamination from the ejecta materials of Theophilus and Madler craters that excavated abundant highland materials.

The elemental maps (Figs. 8–10) reveal that the highland materials have distinctly higher mean abundances of Al (14%), but lower abundance of Fe (10.2%) and Mg (4.2%) than the mare and buried mare units. A few 15–40 km diameter impact craters emplaced on the highland do not show any distinct elemental variation compared to the surrounding highland pixels, suggesting homogeneous highland composition at these impact sites. The highland areas close to the mare and buried mare units have slightly lower abundance of Al and enhanced Fe and Mg abundances, possibly because of contamination caused by the basaltic ejecta materials from nearby craters in the mare areas. Fig. 11 provides the elemental variation within the highland, where a significant number of pixels have higher Al abundances (15–17%) than the average Al value (14%), implying presence of rock types such as pure anorthosite, ferroan anorthosite, troctolitic anorthosite, anorthositic norite and noritic anorthosites (Table S1). A few

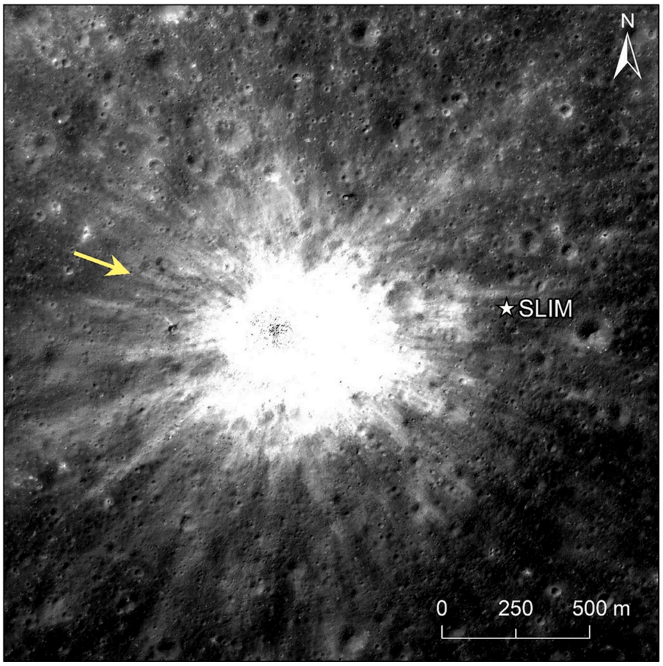

Fig. 14. An asymmetric heart-shaped ejecta pattern around Shioli crater indicating the oblique impact event in which the projectile arrives from roughly west-northwest direction (pale yellow arrow indicates the direction of impact). The white star shows the location of SLIM landed site. The LROC NAC image (M1328124899RE) is in the background. A general slope of the Theophilus crater exterior at the Shioli impact site is south-west. (For interpretation of the references to colour in this figure legend, the reader is referred to the web version of this article.)

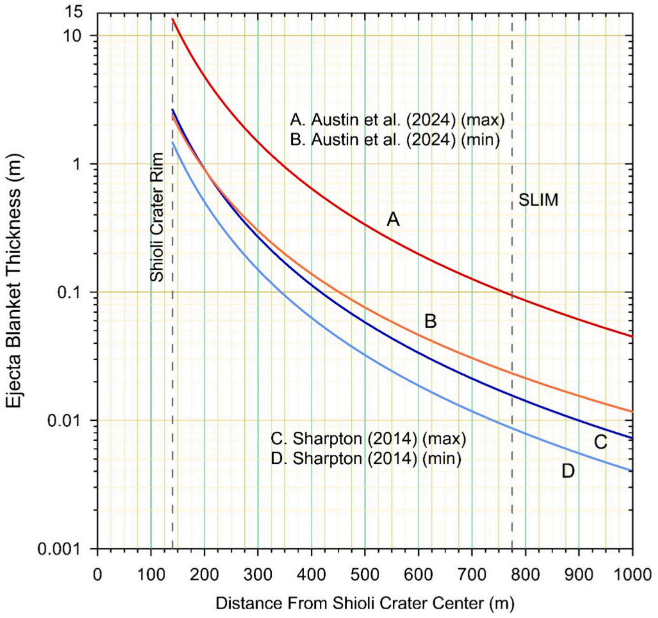

Fig. 15. The radial variation of ejecta blanket thickness of Shioli crater as per equations provided by Sharpton (2014) and Austin et al. (2024). The models 1 (5.14) and 2 (2.76) provide ejecta thicknesses to be 0.22 m and 0.12 m, respectively, at the SLIM landing site.

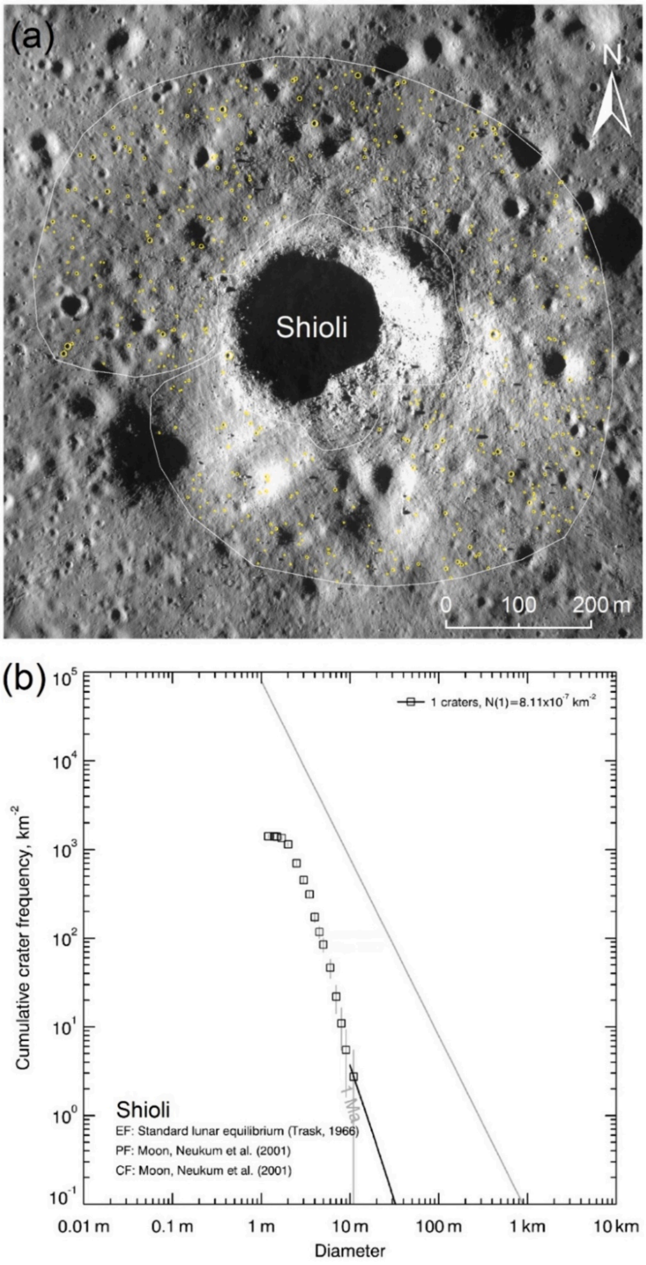

Fig. 16. (a) The OHRC image (ID No. 20210401T2357376656) showing the ejecta blanket of Shioli crater (white polygon), where counting of superimposed impact craters was performed. (b) The cumulative size-frequency distribution of counted impact craters defining an absolute model formation age of Shioli impact crater.

highland pixels are characterized by lower Al (10–14%), and higher abundances of Fe (>10%) and Mg (>5%), which may be related to the exposures of norite and gabbroic norite. Our interpretations are consistent with the Kaguya mineral maps, which confirm that the highland areas are characterized by higher abundance of plagioclase and lower abundances of clinopyroxene and olivine than the mare and buried mare units (Fig. 12). Considering Fortezzo et al. (2020), the CLASS elemental abundances of highland would reflect the composition of ejecta and impact melt deposits of Nectaris and Imbrium basins as well.

The elemental maps clearly demarcate the boundary between the highland and mare/buried mare units (Figs. 8–10). These maps confirm that Theophilus, Madler and Torricelli craters excavated the mare basalt and the underlying highland bedrocks, while Torricelli crater fully excavated the mare basalt, indicating thicker mare units underneath, where De Hon (1974) estimated the basalt thickness to be >1500 m. Theophilus crater and its ejecta are characterized by higher Al (~12%)

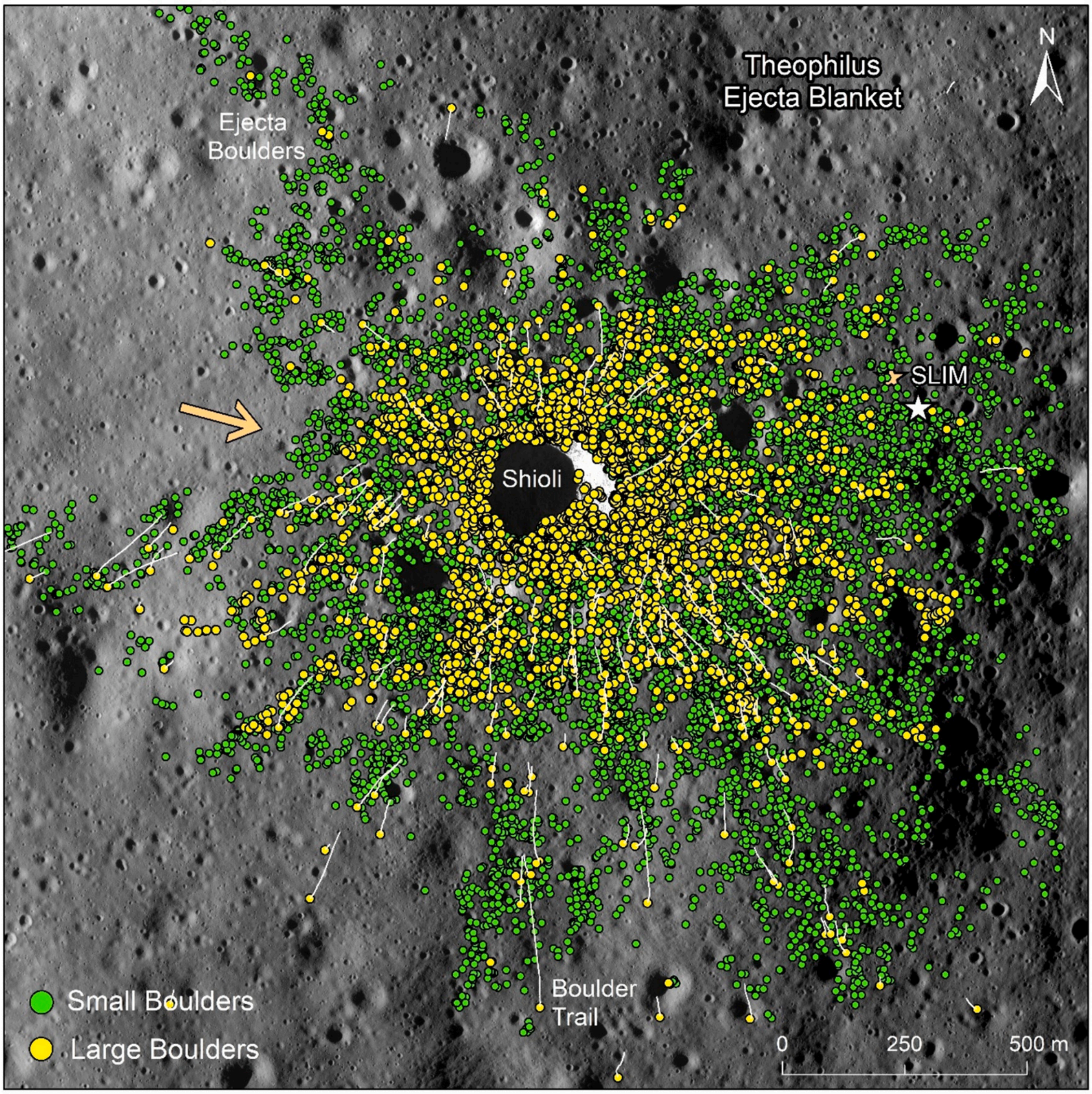

Fig. 17. The OHRC image (ID No. 20210401T2357376656) showing distribution of ejecta boulders in and around Shioli crater. We mapped 2341 boulders with diameters ≥1.5 m (yellow dots; not to scale) and 7881 boulders with diameters ≤1.5 m (green dots; not to scale). Some ejecta boulders produced trails (white lines) along transport paths. The asymmetric distribution of boulders and trails suggest that Shioli crater was formed by an oblique impact, in which the projectile roughly arrived from WNW direction (pale yellow arrow). Shioli crater was formed on the southwestern ejecta blanket of Theophilus crater (see Fig. 3). The SLIM landing site is shown to be white star. (For interpretation of the references to colour in this figure legend, the reader is referred to the web version of this article.)

and lower Fe (>12%) than those of mare and buried mare units, while the Mg map does not show any trend. Fig. 11 suggests that the Theophilus ejecta is a mixture of mare basalt and highland anorthositic materials with a minor component of high-Mg suite rocks. The elemental characteristics of Theophilus crater interior are similar to the ejecta (a mixture of mare basalt and highland anorthositic materials), while some pixels have Mg >6.5%, Fe >12% and Al <12% suggesting the presence of mafic rock types. A minor component of pure anorthosite is also present. Because the Theophilus excavation depth may exceed 8 km (Melosh, 1989) or 2.5 km (Sharpton, 2014), the impact should have fully penetrated the thin layer of mare basalt (~500 m; De Hon, 1974) and excavated the underlying highland bedrock, including the Cyrillus ejecta and Nectaris basin materials (both ejecta and impact melt sheets). These interpretations are broadly consistent with the Kaguya mineral maps (Fig. 12). Shioli crater is characterized by 12.9% Al, 12.8% Fe and 4.7% similar to the Theophilus ejecta. It is noted that the elemental abundance of Shioli crater is an average of two pixels (25 km × 12.5 km), which therefore cannot resolve the original composition of Shioli crater and its ejecta covering a maximum of 4 km × 4 km area. Madler crater is also comparable to the composition of Theophilus. In contrast, Cyrillus crater and its ejecta are more enriched in Al (>14% Al) but more depleted in Fe (<11%) and Mg (<4%) than Theophilus and Madler craters, suggesting anorthositic composition.

4.2. *The study of Shioli crater*

4.2.1. *Crater and ejecta morphology*

Shioli crater is located on the uprange Theophilus ejecta blanket at ~12 km radial distance from the southwestern crater rim of Theophilus. Beneath Shioli crater, the Theophilus ejecta blanket is underlain by the Cyrillus crater floor. Shioli crater is surrounded by many small impact craters, including a 280 m diameter degraded crater that underlies Shioli crater (see Crater 1 in Fig. 13a). Shioli crater is slightly more elongated in ESE direction possibly indicating its oblique impact origin. Shioli crater has a well-developed bright ejecta blanket and distal rays around it (Fig. 14). The ejecta rays exhibit an asymmetric distribution,

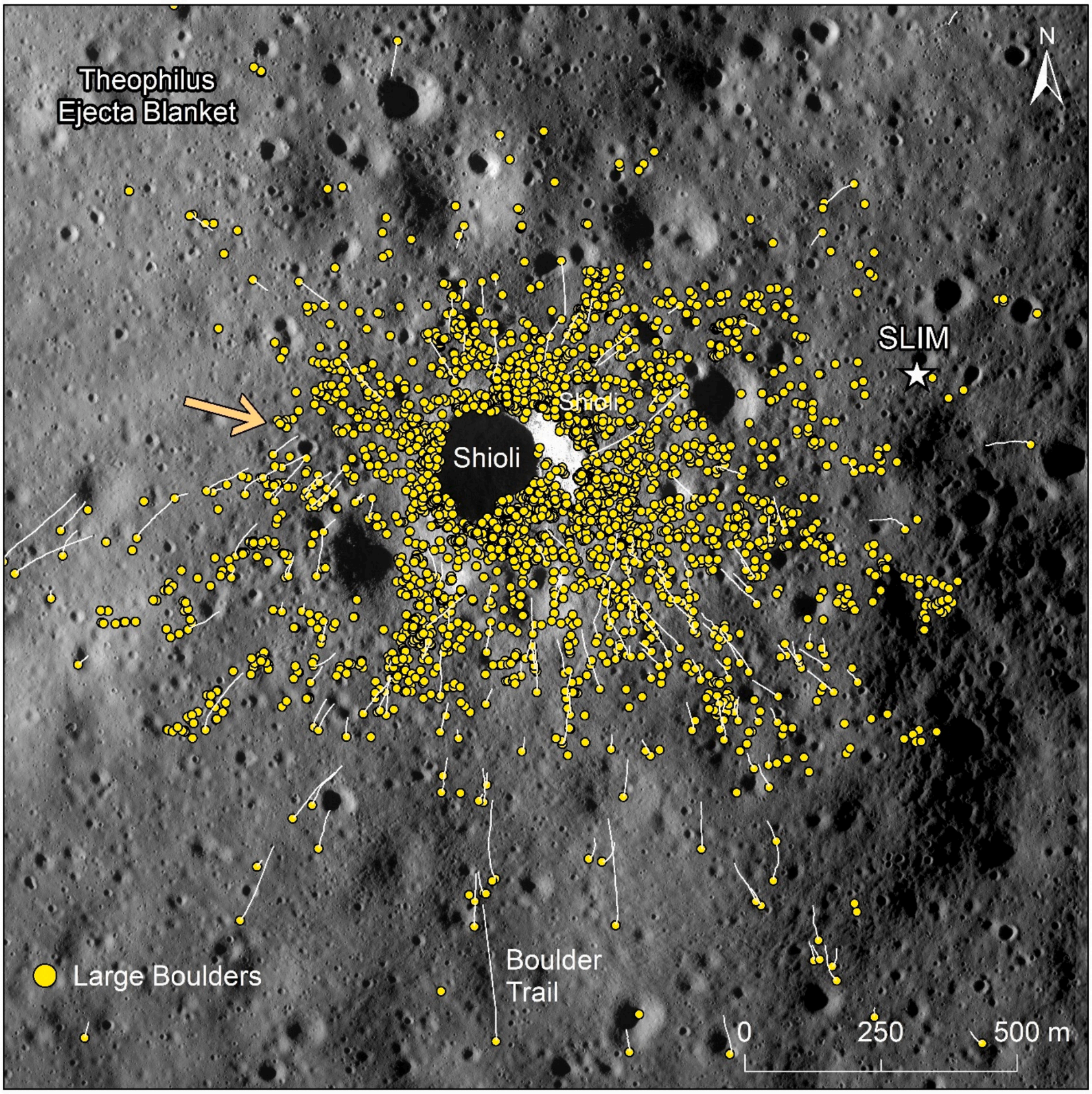

Fig. 18. The OHRC image (ID No. 20210401T2357376656) showing distribution of large ejecta boulders (yellow dots; not to scale) in and around Shioli crater, revealing asymmetric distribution in which the uprange boulders are characterized by short runout distances. The arrow shows the impact direction in which the projectile roughly arrived from WNW direction. The SLIM landing site is shown to be white star. (For interpretation of the references to colour in this figure legend, the reader is referred to the web version of this article.)

exhibiting a forebidden zone in the WNW direction. The ejecta blanket is characterized by many radial striations and lineations and abundant fresh ejecta boulders of diverse size and shape (Fig. 13c). Some ejecta boulders are associated with trails indicating that these ejecta boulders rolled on the surface of ejecta blanket (Mohanty et al., 2023). Using Sharpton (2014) and Austin et al. (2024), we calculated the ejecta thickness of Shioli crater (Fig. 15) (see Supporting Information). These models provide both maximum and minimum ejecta thickness values depending on errors in the constants used in these equations. As per the model of Sharpton (2014), the ejecta thickness at the crater rim is 2.65–1.47 m, which systematically decreases to 0.05–0.03 m at 400 m away from the rim (roughly the edge of the ejecta blanket). At the SLIM landing site (~635 m from the crater rim), the ejecta thickness is 0.02–0.01 m. As per Austin et al. (2024), the ejecta thickness at the crater rim is 13.48–2.36 m, which systematically decreases to 0.27–0.06 m at 400 m away from the rim (roughly the edge of the ejecta blanket). At the SLIM landing site (~635 m from the crater rim), the ejecta thickness is 0.09–0.02 m. While the model of Sharpton (2014) is applicable to 2.2–17 km diameter simple craters, Austin et al. (2024) model is applicable to smaller simple impact craters in the diameter range of 0.1–4.8 km. Hence, the ejecta thickness values derived using the model of Austin et al. (2024) is considered in the study. Shioli crater and its ejecta blanket are overlain by many small fresh primary impact craters. Counting of these craters was performed in a selected area on the ejecta blanket (Fig. 16a). We counted 515 superimposed impact craters in the diameter range of 1.5 m to 11.8 m, in a total counting area of 0.3656 km^2. As we found only one crater above 10 m size, the crater counts did not yield a meaningful age. However, given the alignment of cumulative size frequency distribution with the 1 Ma isochron, we assign the age to be 1 Ma with an unknown error (Fig. 16b).

4.2.2. *Study of ejecta boulders*

Because the SLIM mission has been studying the ejecta boulders of Shioli crater, we characterized all these boulders around the crater.

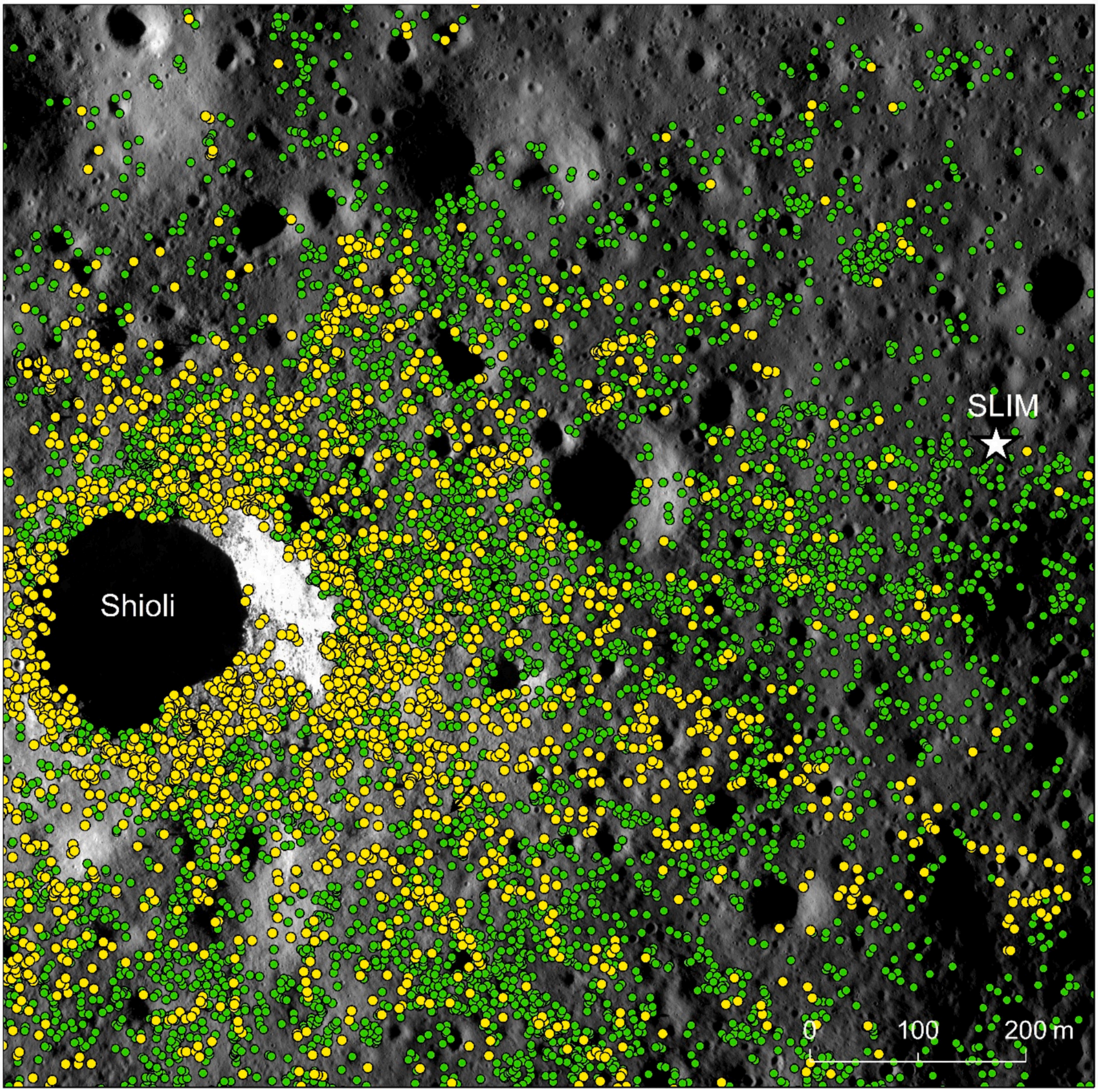

Fig. 19. The OHRC image (ID No. 20210401T2357376656) showing distribution of ejecta boulders in and around Shioli crater and its ejecta blanket. The yellow and green dots (not to scale) are larger (≥1.5 m) and smaller boulders (≤1.5 m), respectively. The SLIM landing site (white star) is located ~775 m ENE of Shioli crater and is at the northern edge of an ejecta ray containing abundant boulders. (For interpretation of the references to colour in this figure legend, the reader is referred to the web version of this article.)

Using the OHRC image, we mapped 2341 boulders with diameters ≥1.5 m (yellow dots; these are grouped as larger boulders) and 7881 boulders with diameters <1.5 m (green dots; these are grouped as smaller boulders) (Fig. 17). The resolution of the OHRC image (25 cm) allows measurement of diameter and aspect ratio of boulders above 1.5 m confidently, while the smaller boulders are only detected. The Arecibo data also suggests abundant boulders in and around Shioli crater giving rise to high CPR values (Fig. 6). Similar to the ejecta (Fig. 14), the boulder dispersal pattern also exhibits a broad asymmetry in which only fewer boulders are found in the WNW side, where the boulders define a V-shaped forebidden zone. Around Shioli crater, the smaller boulders are distributed over a long radial distance (>1000 m from the rim), while a majority of larger boulders are restricted to the ejecta blanket, within ~500 m from the rim. The larger boulders also display the asymmetric distribution pattern with fewer boulders in the WNW side, while the larger boulders are more abundant up to >1 km in ESE direction. We interpret this boulder distribution pattern (Figs. 17 and 18) is due to an ESE directed oblique impact, which is consistent with the elongated crater shape and asymmetric ejecta pattern of Shioli crater (Figs. 13 and 14). Fig. 19 shows the boulder distribution in the eastern part of Shioli ejecta including the SLIM landing site, which is located about 775 m ENE of Shioli crater. Overall the population density of boulders around the crater gradually decreases away from the crater rim. Fig. 20 shows that the SLIM landing site is located near the southwestern rim of a ~ 50 m diameter degraded impact crater, which predates the Shioli ejecta. Though the Shioli ejecta is present at the SLIM landing site, the ejecta of the 50 m underlying crater may also be mixed with it. Just 20 m south of this crater, a prominent Shioli ejecta ray having a width of 20–30 m contains many smaller boulders. We suggest that the SLIM landing site may contain abundant sub-meter sized boulders, but not larger boulders.

Fig. 21 shows how boulder sizes decrease with increasing distance from the crater center. The largest boulders are concentrated near the crater rim. The size of the largest boulder is 12.4 m. We found 26

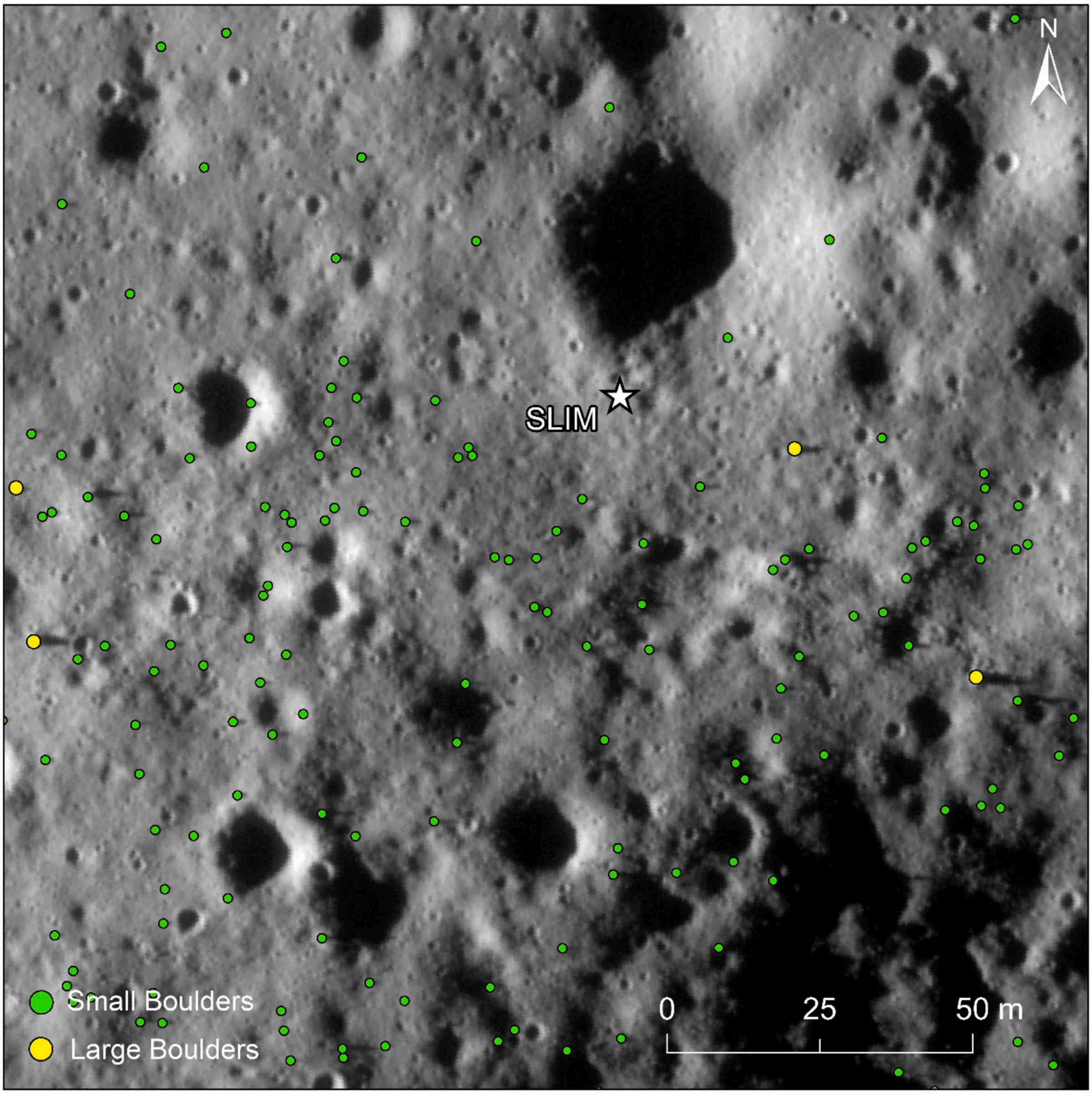

Fig. 20. The OHRC image (ID No. 20210401T2357376656) showing the details of SLIM landing site and the surrounding plains. The landing site is located on the south-western edge of a ~ 50 m diameter impact crater and the distal ejecta rays from Shioli including a few boulders overlie the crater.

boulders with diameters ≥5 m, while the remaining 2315 boulders are in the range of 1.5 to <5 m. In the ejecta blanket, the boulder size varies from ~1.5 m to 12.4 m. At the range of SLIM landing site, boulder size is in 1.5–4 m range. The shapes (aspect ratio = long axis ÷ short axis) of the boulders were also measured, following the methodology given by Krishna and Kumar (2016). As in many impact craters on the Moon (Krishna and Kumar, 2016), Mars and Earth (Lakshmi and Kumar, 2020), the aspect ratios of boulders are large near the crater rim (range = 1–2.75), while it decreases to 1–2.25 at the SLIM landing site range, and it further decreased to 1–1.75 away from this site. We plotted the cumulative size frequency distribution (CSFD) of Shioli ejecta boulders in Fig. 22. A power-law fit to the CSFD of the boulders in the diameter range of 2–8.5 m yielded a b-value of −4.06. Bart and Melosh (2010) also documented higher b-values from many small lunar impact craters. The b-value of boulders reflect the amount of complex impact fragmentation in the boulders (e.g., Kumar et al., 2014); an increase in b-value implies greater complex fragmentation in the ejecta boulders. Since the Shioli boulders were produced from the fragmentation of already existing buried Theophilus ejecta boulders, multiple cycles of impact fragmentation led to a higher b-value at Shioli crater.

The sizes of ejecta boulders also provide an insight into whether the host Shioli crater is primary or secondary impact origin. To determine this, Bart and Melosh (2007) provided the relationship between the crater diameter and the average size of five largest ejecta boulders in the host crater ejecta: ejecta boulder diameter = K × crater diameter $^{2/3}$ (K = 0.29 for primary craters and 0.46 for secondary craters). When a primary and secondary crater of equal size are compared, the ejecta boulder sizes around the primary crater are generally smaller than those around the secondary crater. We measured the diameters of five largest ejecta boulders from Shioli crater to be 12.4, 10.7, 8.5, 8.3, and 7.8 m, which yielded a mean diameter of 9.5 m. Considering the Shioli crater diameter to be 280 m, Fig. 23 suggests that Shioli crater is a primary crater, and is similar to many small primary craters in the Orientale basin (Mohanty et al., 2023).

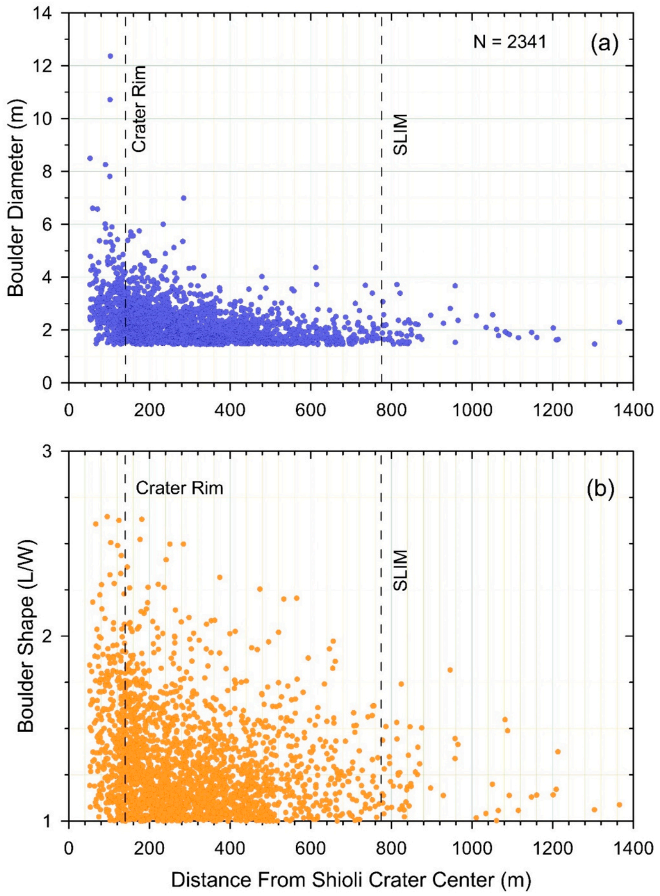

Fig. 21. Size and shape of ejecta boulders in and around Shioli crater. (a) A radial variation of ejecta boulder sizes (diameters ≥1.5 m) in and around Shioli crater. Larger size boulders are concentrated near the crater rim. A gradual decrease in the boulder size is observed from the crater rim to the edge of ejecta blanket. At the distance of SLIM landing site, the boulders are smaller than 4 m. (b) A radial variation of ejecta boulder shapes (length ÷ width of boulders) showing a gradual decrease of aspect ratio from the crater rim to the edge of ejecta blanket. At a distance of SLIM landing site, the aspect ratio is <2.

4.2.3. Impact conditions

Because Shioli is a primary crater, it should have formed by a hypervelocity impact. Therefore, for calculating various impact parameters such as projectile size, projectile penetration depth in target, transient crater diameter, ejection velocity, ejection angle, spall plate thickness (spall boulder sizes), and final range of ejected boulders, we assumed an impact velocity of 16 km/s, which is a median value for the impact velocity distribution on the Moon (Yue et al., 2013), and vertical angle of impact (90°). The physical properties of projectile and target and the equations used in these calculations are given in the Supporting Information. Because the target for Shioli crater is the Theophilus crater ejecta blanket, we assigned the values of density, compressional-wave velocity and dynamic tensile strength to be 1500 kg/m^3, 800 m/s and 27 MPa, respectively, as suitable for the fragmental target. On the other hand, we assumed the density of projectile to be 2900 kg/m^3 (intact basalt). The projectile diameter was calculated to be 3 m and the diameter of transient Shioli crater to be 224 m. Because the spall (or ejecta) boulders were derived from the transient crater, within the radial distance of ~10–112 m from the impact point, we calculated the ejection velocity, ejection angle and spall size for boulders originated from these initial launch positions (10–112 m). The excavation depth was determined to be 6.8 m (Sharpton, 2014) or 22.4 m (Melosh, 1989), depending on the model. Hence, the Shioli boulders were derived from the upper few meters of pre-impact target made up of Theophilus ejecta with a model thickness of ~223 m at this location (Fig. 5).

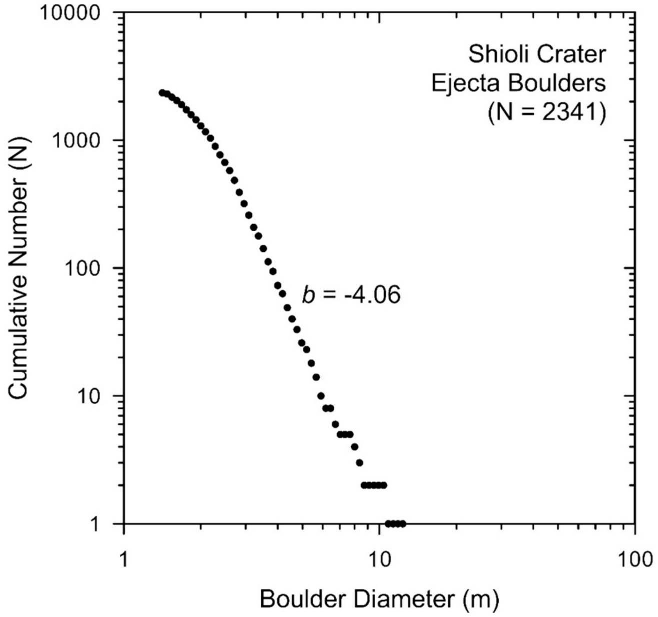

Fig. 22. The cumulative size-frequency distribution of ejecta boulders of Shioli impact crater characterized by steeper power-law b-value (−4.06) suggesting complexly fragmented ejecta boulders, as these were derived by impact fragmentation of already existing ejecta boulders of Theophilus crater.

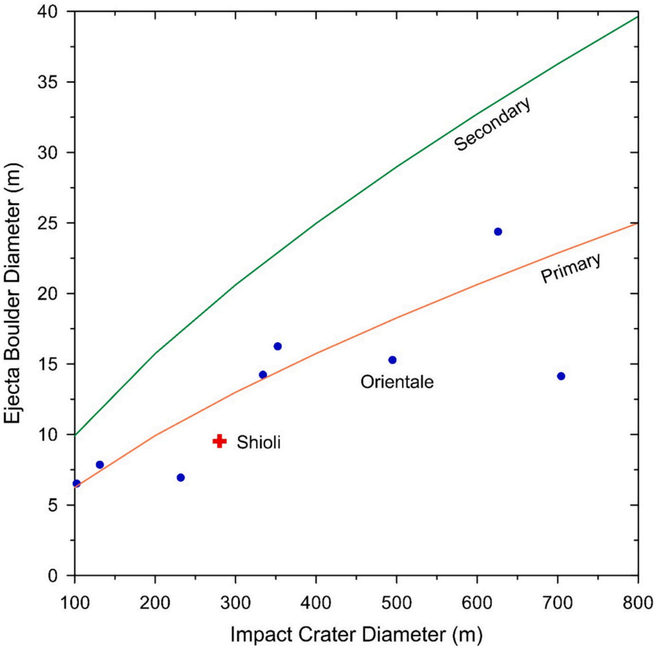

Fig. 23. Relationship between the Shioli crater diameter and average diameter of five largest ejecta boulders in its ejecta blanket suggests that the Shioli crater is a primary impact crater, which is similar to the ejecta boulder fall bearing fresh impact craters in the Orientale basin (Mohanty et al., 2023). The relationship is based on the datasets from Bart and Melosh (2007).

The ejection velocity of boulders originated from the transient cavity ranges from 1290 m/s to 7.4 m/s. The boulders composing the ejecta blanket (~150–1400 m distance range from the crater center) are characterized by the ejection velocity of 7.4–47.4 m/s (Fig. 24a). The ejection angle of spall boulders varies from 57.4° near the impact point to 41.8° near the edge of transient crater. However, the boulders fallen

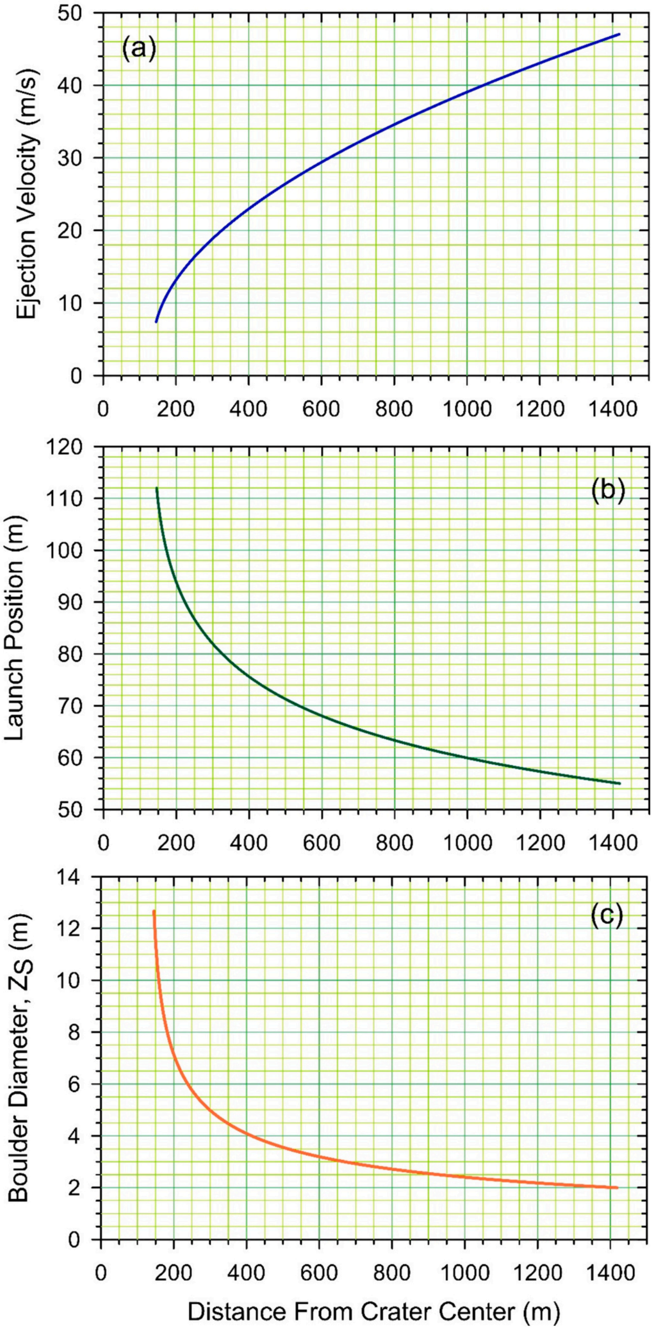

Fig. 24. The plots showing the variation of (a) ejection velocity or fall velocity of ejecta boulders deposited within the Shioli ejecta blanket, (b) relationship between initial range (launch position) of Shioli ejecta boulders within the transient cavity and their final positions in the ejecta blanket, and (c) theoretical boulder size distribution in the Shioli ejecta blanket (orange line) as per the theoretical spallation model (Z_S = short axis of the ejecta boulder) (Melosh, 1984).

on the ejecta blanket are likely to have ejected at 41.8–43.1° range. The ejection angles and ejection velocities of boulders were used for calculating their final destination points (final range). The boulders ejected near the impact point travelled over distance 944 km from the crater center, while those originated near the edge of transient cavity were fallen near the crater rim, ~150 m radial distance from the crater center. The boulders ejected from the initial range of 55–112 m within the transient crater were ballistically deposited on the ejecta blanket (Fig. 24b). Fig. 24c gives the theoretical boulder size (spall thickness) variation on the ejecta blanket. The maximum calculated boulder size near the crater rim is 12.5 m, which is similar to the observed maximum boulder size (12.4 m) near the crater rim. At the SLIM landing site distance (~775 m), the maximum calculated boulder size is ~2.75 m, whereas the observed maximum boulder size is ~4.0 m. At a radial distance of 1400 m from the crater rim, the calculated boulder size is further reduced to ~2 m. Though the theoretical boulder sizes (Fig. 24c) are broadly match with the observed maximum boulder sizes at different radial distances, a majority of boulders in the ejecta are smaller than the calculated values (Fig. 21a). We attribute this observation to the involvement of complex fragmentation (crushing) associated with the impact spallation, excavation, collision between fragments during ballistic sedimentation (e.g., Kumar et al., 2014; Krishna and Kumar, 2016). Our interpretation is consistent with the observed large b-value for the mapped Shioli boulders (Fig. 22).

4.2.4. *Composition of Shioli boulders*

The Kaguya mineral maps suggests that the Shioli crater ejecta boulders are characterized by distinct mineralogical composition than the surrounding area (Fig. 25). The plagioclase content in the Shioli boulders is lower (60–70%) than the surrounding area (70–90%). In contrast, the olivine content in the boulders (5–11%) is higher than the surrounding area (<5%). Similarly, clinopyroxene content is also higher (15 to 37%) than the surrounding area (15%). Therefore, the Shioli crater ejecta boulders are more mafic in composition than the surrounding materials. We suggest that the bulk mineralogy of these boulders is comparable to the high aluminium olivine basalt (Mare Nectaris) that was present on top of the pre-impact Theophilus target. Alternatively, there could be some mixed contributions from the Mg-suite mafic rocks and highland materials present in the pre-impact target, beneath the surficial mare layer.

In order to confirm the findings from the Kaguya mineral maps, we analysed the hyperspectral data (M^3) of the Chandrayaan-1 mission, which provided a set of maps showing the mineralogical diversity in the study area (Figs. 26–30). Though the Theophilus ejecta contains mature surface regolith showing featureless M^3 spectra, a few superimposed fresh impact craters and their surrounding bright ejecta provided M^3 spectra containing characteristic absorption features that can be used for identifying mafic minerals present in these crater materials (Fig. 31). We studied seven fresh small impact craters that are superimposed on the Theophilus ejecta, including Shioli (Table S2). The craters UC-1, UC-2 and Beaumont L are superimposed on a thin Theophilus distal ejecta (Table S2). These craters not only fully excavated the Theophilus ejecta but also penetrated the underlying Mare Nectaris basalt flows, leading to the formation of dark-haloed ejecta around these craters (Figs. 26–30). In the Kaguya mineral maps, the dark-haloes are characterized by distinct mineral composition than the surrounding materials (Fig. 32). The reflectance M^3 spectra from UC-1 and UC-2 craters show dual absorption features near 1000 nm and 2000 nm (Figs. 31a-b). The band center values for absorption bands I and II range from 970-1000 nm and 2000–2100 nm, respectively, which correspond to high-calcium pyroxene (HCP) and the band center shift due to olivine. Also, the spectrum of Beaumont L is characterized by a prominent absorption near 1050 nm followed by a minor absorption near 2000 nm (Figs. 31a-b), indicating the predominant olivine in the ejecta. The marginal absorption at 2000 nm may be attributed to a small quantity of pyroxenes in neighbouring pixels (Figs. 31a-b). Therefore, both the M^3 and Kaguya data confirm that the dark-haloed craters are made up of crypto-mare materials with higher abundances of olivine and FeO, but are depleted in plagioclase minerals (Fig. 32). These mineralogical characteristics are consistent with the olivine bearing basalt that are present elsewhere in the Mare Nectaris.

The Shioli and the other nearby craters UC-3, UC-4 and UC-5 are superimposed on thick Theophilus ejecta blanket and only excavated its upper part (Table S2). These craters are characterized by bright ejecta deposits, but they lack dark-haloes around them. The mineral diversity

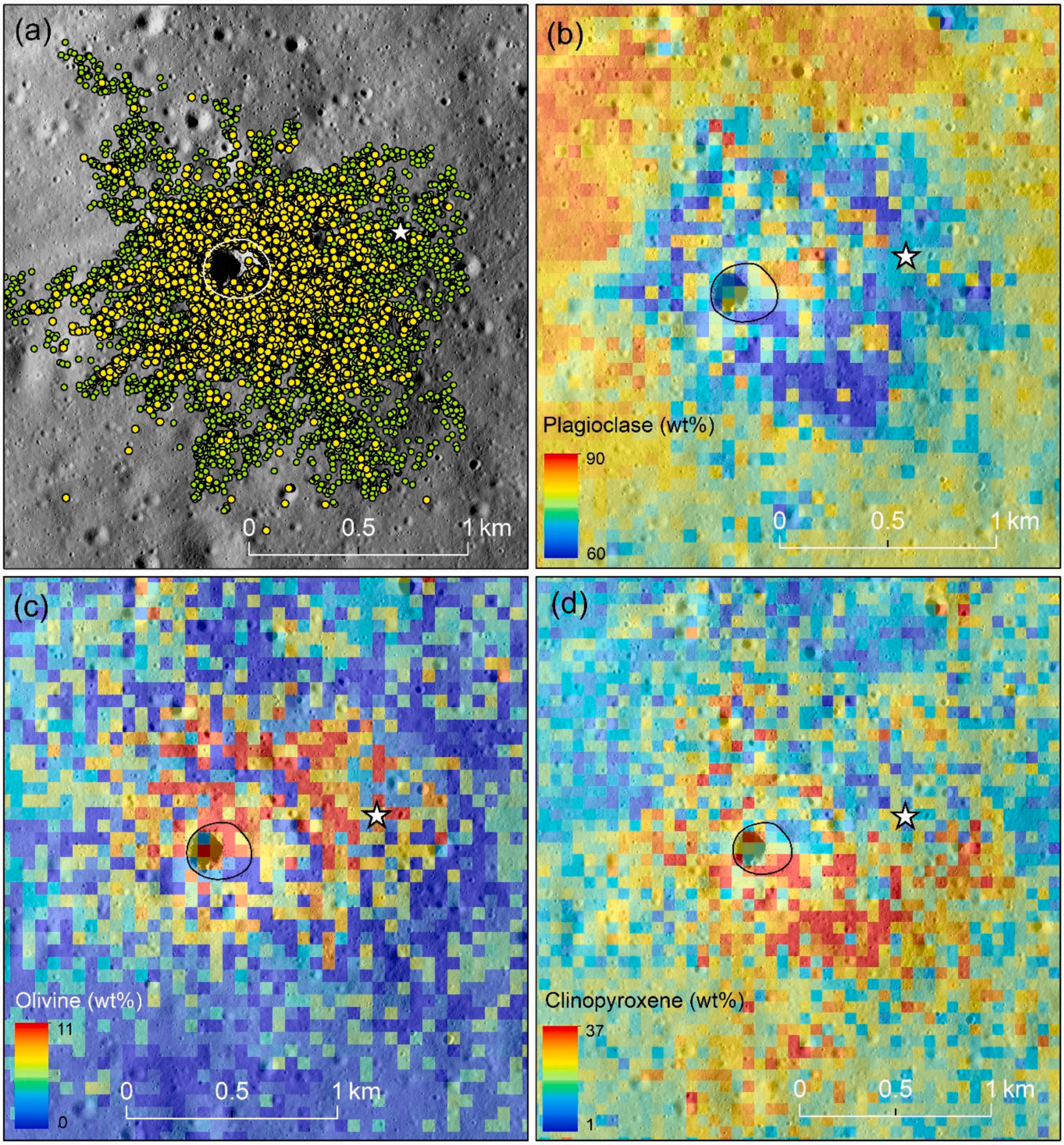

Fig. 25. Kaguya mineral maps of Shioli crater and its ejecta boulders (Lemelin et al., 2019). (a) Ejecta boulders in and around Shioli crater. LROC NAC image (M1188200376RE) is in the background. (b) Plagioclase abundance map, (c) olivine abundance map and (d) clinopyroxene abundance map of Shioli crater and surrounding regions. The Shioli ejecta is characterized by higher abundance of olivine and clinopyroxene and lower abundance of plagioclase with respect to the surrounding plains. The white star is the SLIM landing site.

in and around Shioli, UC-3, UC-4 and UC-5 craters are shown in Figs. 26–30 and representative M^3 spectra in Fig. 31c-d. The M^3 spectra of Shioli crater area reveals significant spectral absorptions at approximately 1030 nm and 2090 nm (Figs. 31c-d). The strong absorption at 1030 nm is attributed to the presence of olivine, while the absorption at 2000 nm may be indicative of pyroxenes in the area or adjacent pixels. The craters UC-3, UC-4, and UC-5 (Figs. 26–30) display bimodal spectral absorptions in their reflectance spectra at approximately 1000 and 2000 nm (Figs. 31c-d). The band-I absorption varies from 950 to 989 nm, and band-II from 2000 to 2100 nm, suggesting the occurrence of more HCP-bearing exposures (Figs. 31c-d) than in the Shioli crater ejecta.

The M^3 pixels encompassing the SLIM landing site in conjunction with its surrounding pixels were analysed and the spectra of these individual pixels are given in Fig. 33. Determining the specific mineralogical characteristics from these pixels is challenging, as these have featureless spectra with a minimal noise near 1000 nm. Given the spatial resolution of M^3 data (140 m/pixel), our analysis provides a useful mineralogical overview of the landing site, which is characterized by mafic components such as olivine and pyroxenes. Notably, adjacent pixels to the west of the landing site display conspicuous spectral signatures indicative of olivine-bearing mineralogy, possibly stemming from the ejected material of Shioli crater. Conversely, the M^3 pixels situated to the east of the landing site exhibit spectra devoid of distinct features, likely obscured by the presence of mature lunar regolith in them. Hence, we suggest that landing site may contain the ejecta material of Shioli crater mixed with the underlying ejecta substrate of the 50 m diameter crater that excavated the Theophilus ejecta (Fig. 20).

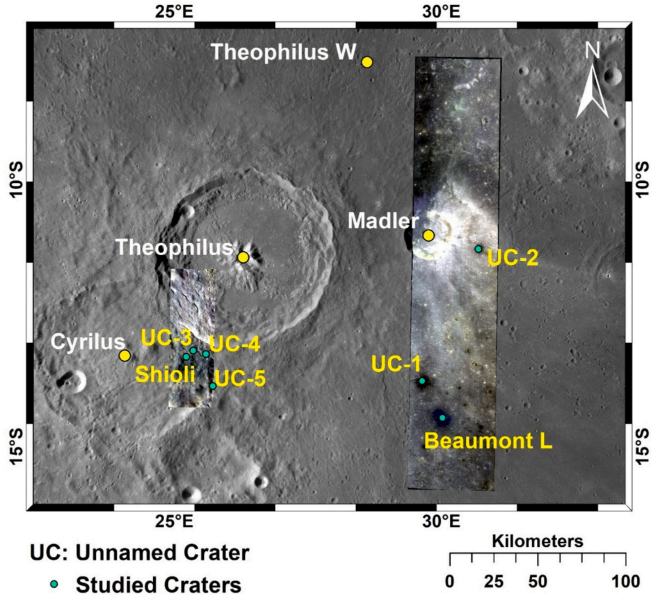

Fig. 26. The False Colour Composite of M^3 image prepared by assigning the red, green and blue channels to the 930 nm, 1249 nm and 2149 nm of M^3 bands, overlaid on LROC-WAC global mosaic. The studied sites have been marked by cyan dots. (For interpretation of the references to colour in this figure legend, the reader is referred to the web version of this article.)

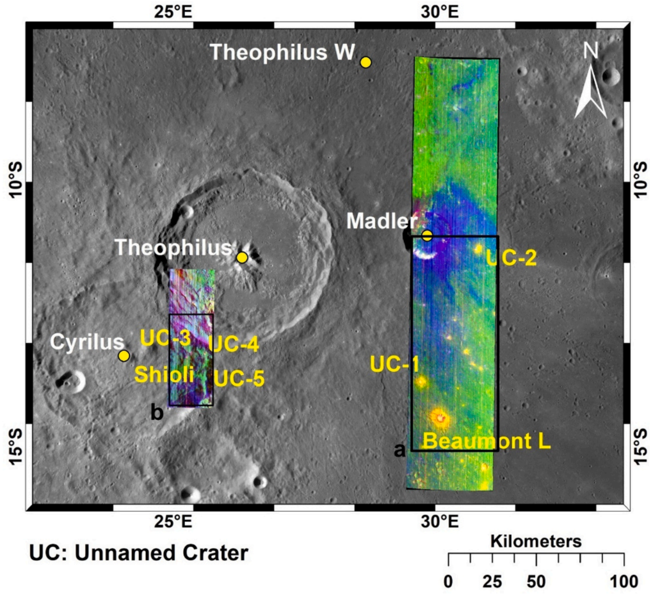

Fig. 27. The IBD-FCC map generated by using 1000-nm IBD, 2000-nm IBD and 1578-nm M^3 albedo band in the red, green and blue channels, respectively. The map is overlaid on the LROC-WAC global 100 m data. (For interpretation of the references to colour in this figure legend, the reader is referred to the web version of this article.)

5. Discussion

The determination of whether the olivine detected in the Shioli ejecta boulders was derived from crust or mantle is one of the major goals of the SLIM mission. Our detailed geological, geochemical, mineralogical and geophysical characterization of Theophilus crater and the surrounding regions provided important constraints on the geological setting of Shioli crater and the source of olivine in its ejecta boulders. A basic requirement of mantle-derived olivine to be present in the

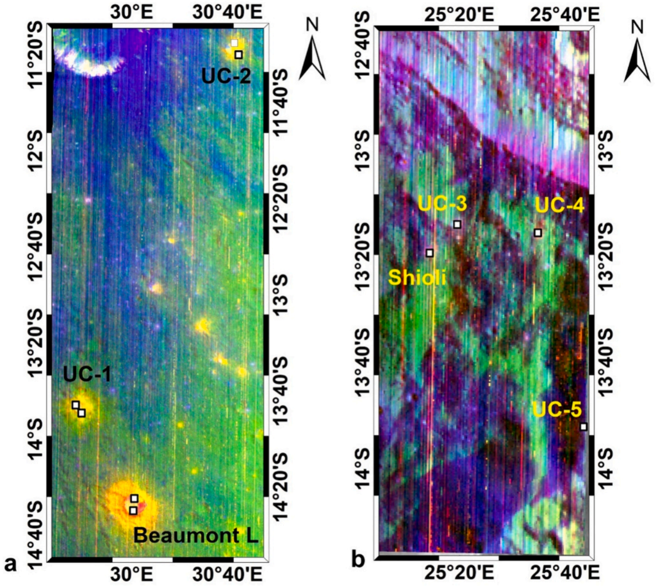

Fig. 28. The 1000–2000 nm IBD-FCC map of (a) Beaumont L region including craters UC-1 and UC-2 and (b) Shioli crater area including the adjacent UC-3, UC-4 and UC-5 craters. The locations of Regions of Interests (ROIs) from which M^3 spectra were obtained for mineralogical investigation are demarcated by white squares.

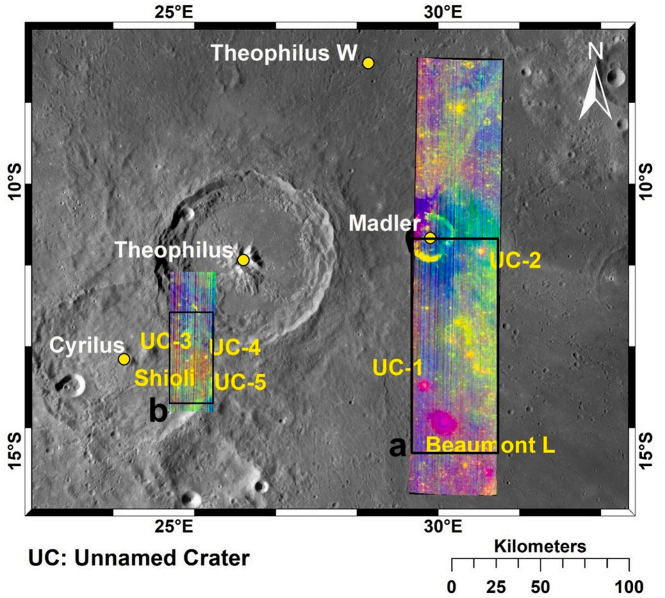

Fig. 29. The rock-type composite map prepared using the similar band math [R: float (b5 + b30)/b17), G: float (b40 + b41)/(b52 + b53), B: float (b20 + b45)/(b32) given by Pieters et al. (2014).

Shioli crater boulders is that Theophilus crater should have excavated the olivine-bearing lunar mantle at the impact site. In addition, the olivine bearing mantle rocks should also be present in the near-surface depth (a few ten to hundred meters) so that the impact spallation processes associated with the Theophilus impact would be able to generate spall boulders out of them. Several previous studies showed the ejecta boulder distribution around impact craters on the Moon and quantified the impact conditions and modelled the theoretical boulder sizes (e.g., Melosh, 1984; Bart and Melosh, 2010; Krishna and Kumar, 2016). The lithological assemblage present in the excavation zone of Theophilus crater mainly controls the compositional diversity in the Theophilus

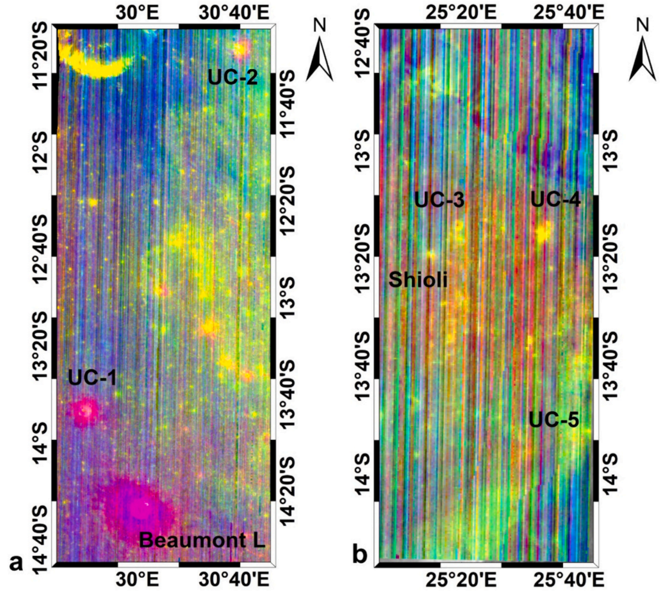

Fig. 30. The Rock-type composite map showing the mineralogical distribution within the (a) Beaumont L region, including craters UC-1 and UC-2 and (b) Shioli crater area, including the adjacent UC-3, UC-4 and UC-5 craters.

ejecta. The excavation depth of Theophilus crater is ~8.2 km, considering the relation 0.1 × transient crater diameter (=82.4 km) (Melosh, 1989) or it could be 2.5 km, assuming 0.03 × 82.4 km (Sharpton, 2014).

5.1. *Crustal structure beneath the Theophilus crater*

The crustal configuration and petrological assemblage in the Nectaris multi-ring basin have important implications for compositional diversity in the Theophilus crater and its ejecta deposits. Therefore, we prepared a regional geological cross-section along NW-SE direction (Figs. 34 and 35) for a distance of 1000 km, starting from the area outside the outer ring of basin in the northwestern side (X in Fig. 34) to the middle ring in the southeastern side of the basin (Y in Fig. 34). Another section AB for a distance of 300 km was prepared across the Theophilus crater (Figs. 34 and 35), parallel to the XY profile. We combined the topography, surface geology, petrological model derived from the CLASS, Kaguya and M^3 datasets, and the crustal thickness variation given by the GRAIL data. Overall, the crustal thickness variation beneath the Nectaris basin (Fig. 34) resembles the general characteristics of multi-ring basins on the Moon, for example, the Orientale basin (e.g., Zuber et al., 2016). The crust beneath the central part of basin (mare Nectaris) has a minimum thickness of ~10 km, implying that the Nectaris basin forming impact did not excavate the lunar mantle. The crust underneath the basin rings are substantially thicker than the central part. In the southeastern side, the crustal thickness abruptly increases from ~20 km beneath the inner ring to ~35 km beneath the middle ring. In contrast, the crustal thickness beneath the basin rings in the northwestern part of the basin, especially beneath the 300 km crater floor, is thinner (~15–20 km) (Fig. 35). We ascribe this crustal thinning to the formation 300-km impact crater, which should have removed the highland upper crust.

The highland crust outside the Nectaris basin has a maximum thickness of 48 km. Along the XY section (Fig. 35), we found a crustal downwarping up to a depth of ~22 km between the inner and middle rings in the northwestern side, which coincides with a NE-SW oriented topographic ridge at the contact between the rim of 300 km crater and the inner ring of Nectaris basin. We suggest that this ridge may have existed at the Theophilus impact site before the impact. The AB section also confirms the presence of crustal down-warping (up to a depth of 28 km) beneath Theophilus crater (Fig. 35). If we assume that the Theophilus impact excavated the upper 8.2 km of the crust, the remaining 20 km thick crust is still preserved beneath Theophilus crater. Therefore, considering the presence of crust-mantle boundary is at ~28 km depth beneath Theophilus crater (Fig. 35), we conclude that the Theophilus crater did not excavate the lunar mantle.

The crustal configuration of the Nectaris basin and the surrounding areas (Fig. 35) suggests that the basin forming impact significantly modified the crust in the study area. Before the Nectaris basin forming impact, the region would have been similar to the highland crust outside the basin, especially outside the western, southern, and eastern boundary of the basin, where the crustal thickness is of the orders of 40–50 km. In the areas covered by the basin rings, an average of 10–15 km thick crust may have been removed by Nectaris impact, while in the northwestern side, the 300 km diameter crater removed 10–15 km crust more, leading to the exposure of lower crust on the crater floor (Fig. 35). In the areas covered by the inner and middle rings, where crustal downwarping is observed, traces of upper crust may still be present. Therefore, arguably, the pre-impact Theophilus target crust may have contained ~2–3 km highland upper crust on the top, underlain by the entire highland lower crust. In the central basin (mare Nectaris area), ~30 km crust was removed by Nectaris impact, leading to the exposure of the middle part of the lower crust beneath the Mare Nectaris.

The emplacement of mare basalt in the Nectaris basin occurred around 3.8 Ga, about ~100–300 million years after the Nectaris basin forming impact. The mare volcanism occurred in the central basin floor and in the 300-km crater floor (Fig. 35), as the lavas may have erupted through dikes that are connected to the subjacent magma chambers and reservoirs (e.g., Head and Wilson, 2017; Head et al., 2023). In these areas, the mare basalt flows of variable thickness constitute the surface of the Mare Nectaris (Fig. 35). Therefore, in the XY and AB crustal sections (Fig. 35), we included a ~ 500 to ~1500 m thick olivine mare basalt top-layer, underlain by 2 km highland upper crust and 20 km lower crust. These lava flows may still be present beneath the Theophilus ejecta blanket, except in the southwestern side where Theophilus ejecta blanket is underlain by Cyrillus crater. It is also noted that, at the Theophilus impact site, the mare basalt layer was underlain by the ejecta blanket of Cyrillus crater (see Fortezzo et al., 2020; Fig. 3), with its thickness varying between ~400 and 10 m (Fig. 5), by adapting similar ejecta thickness profile of Theophilus (Cyrillus diameter is almost equal to Theophilus). Considering the CLASS elemental data (Fig. 11), the Cyrillus ejecta blanket is made up of anorthositic highland materials. In addition, layers of Nectaris basin ejecta and impact melt sheets are also envisaged to be present beneath the Cyrillus ejecta blanket.

Considering the crustal thickness map (Fig. 34), no impact craters in the Nectaris basin, including in the central mare region, would have excavated the lunar mantle. We also suggest that the Nectaris basin forming impact did not excavate the lunar mantle. Considering the Kaguya mineral maps and M^3 mineral detections, the mare basalts in the Nectaris basin are enriched in olivine. In addition, the Theophilus central peak also contains some exposures of olivine that could be related to Mg-suite plutons at the mid crustal levels (e.g., Shearer et al., 2015; Fig. 35). These could be other possible sources of olivine in the Theophilus and Shioli ejecta deposits. Differentiation of enormous volume of impact melt sea was also suggested to produce a thick bottom layer of olivine (e.g., Vaughan et al., 2013), but this possibility was greatly debated (e.g., Spudis et al., 2014). Whether the Nectaris impact melt sheets underwent differentiation or not, is unknown.

5.2. *Provenance of Theophilus and Shioli boulders*

The olivine-bearing Shioli boulders are products of impact spallation processes, meaning that these boulders were originated from the upper few meters thick surficial layer of >200-m-thick Theophilus ejecta blanket present at the Shioli crater site. The Shioli boulders were produced by the complex fragmentation of buried Theophilus ejecta

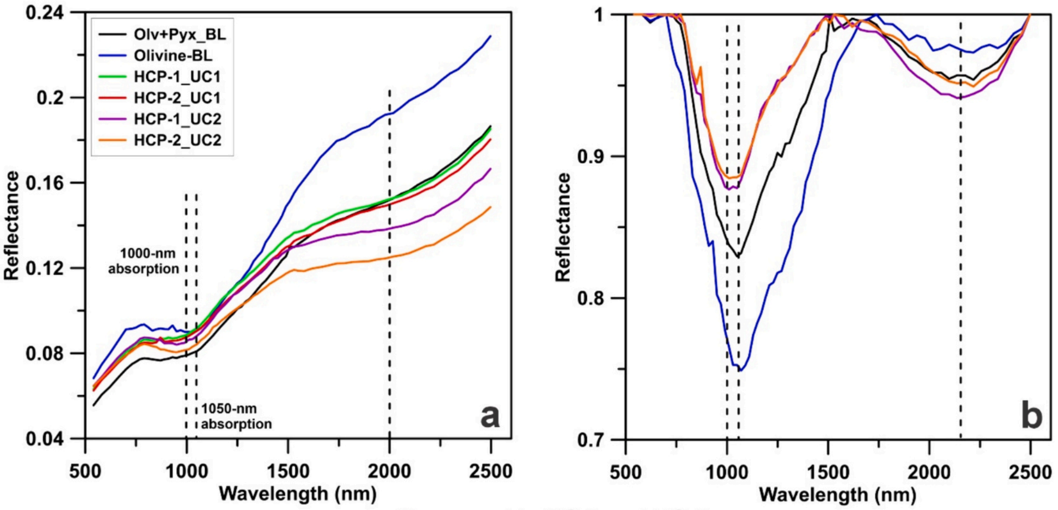

Beaumont L, UC-1 and UC-2

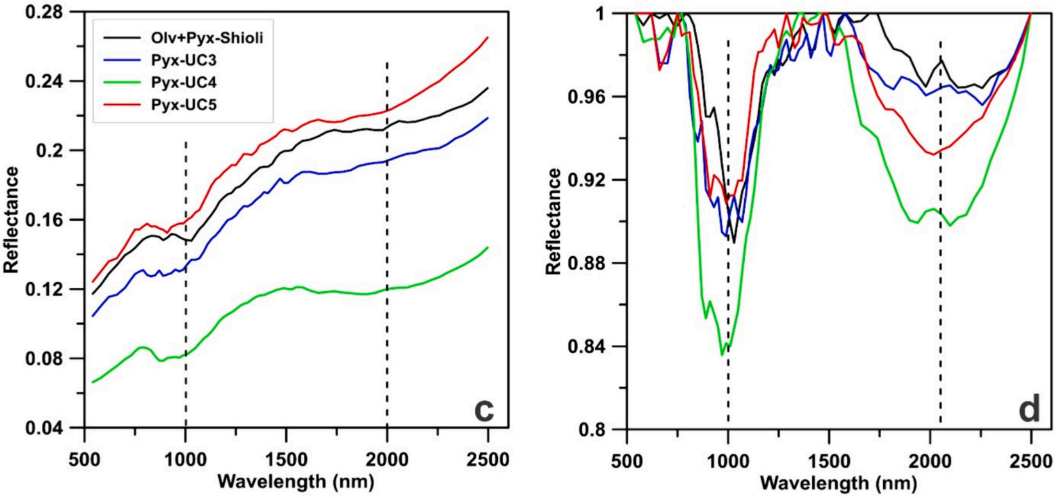

Shioli, UC-3, UC-4 and UC-5

Fig. 31. (a) The representative reflectance spectra of various minerals present in the study area and corresponding (b) continuum-removed spectra. Locations of these spectra are shown in Fig. 27. (c) The representative reflectance spectra of various minerals present in the study area and corresponding (d) continuum-removed spectra. Locations of these spectra are shown in Fig. 27.

boulders made up of olivine mare basalt mixed with the highland anorthositic materials, including Mg-suite mafic lithology and reworked Nectaris basin materials. A minor component of reworked Cyrillus ejecta may also be present. Therefore, the lithological diversity in the Shioli ejecta boulders represents the composition of buried Theophilus ejecta boulders. To understand the possible sizes of source Theophilus ejecta boulders, we performed the theoretical spallation modelling that provides a range of spall boulder sizes that may have originated from the Theophilus target (see Supporting Information). We assumed a model in which a basalt-like projectile with a density of 2.9 g/cm^3, a radius of 3538 m, and impact velocity of 17.4 km/s impacted the lunar target having a bulk density of 2.9 g/cm^3, compressional wave velocity of 6 km/s and dynamic tensile strength of 150 MPa. Considering these parameters, the Theophilus impact would have produced spall boulders in the size range of 70–314 m. The boulders in the Theophilus ejecta blanket (Fig. 5) have diameters in the range of 314 m (at the crater rim) to 192 m (at the edge of ejecta blanket). These boulders were originated from the initial range (or launch position) of 31 to 37 km from the center of transient crater (~37 km radius), which coincides with the south-western terraced wall of Theophilus crater.

We envisage that the Theophilus pre-impact target in this launch zone (31 to 37 km) was composed of ~500 m thick olivine basalt top-layer underlain by a layer of ~400 m thick Cyrillus anothositic ejecta. Below these two layers, middle to lower crustal highland crust coated with the Nectaris basin ejecta and impact melt sheets were present (Fig. 35). The impact spallation processes would have produced basaltic boulders from the near-surface layer of the target, and ballistically deposited on the Theophilus ejecta blanket. It is noted that the basalt layer thickness in the pre-impact target is unknown. It is possible that the thickness of mare basalt may be varied spatially, and may be thinner than 500 m as well. Under these circumstances, the basement highland crust beneath this basalt layer would have been subjected to impact spallation and production of anorthositic materials. The Kaguya mineral maps (Fig. 12) suggest that olivine exposures are absent in the south-western terraced wall of the Theophilus crater implying that the olivine basalt is the likely major source of olivine in the Shioli boulders, though some amount of underlying highland rocks (including the Cyrillus and Nectaris ejecta) may also have been incorporated into the ejected boulders. Beneath the spall zone, the target materials in the excavation zone are highland rocks that would have subjected to high-levels of shock, pulverisation, melting and shock materials. These finer highland fragmental and shocked materials were also incorporated into the Theophilus ejecta. Therefore, we envisage that the Shioli crater ejecta deposits are made up of olivine mare basalt boulders that are embedded

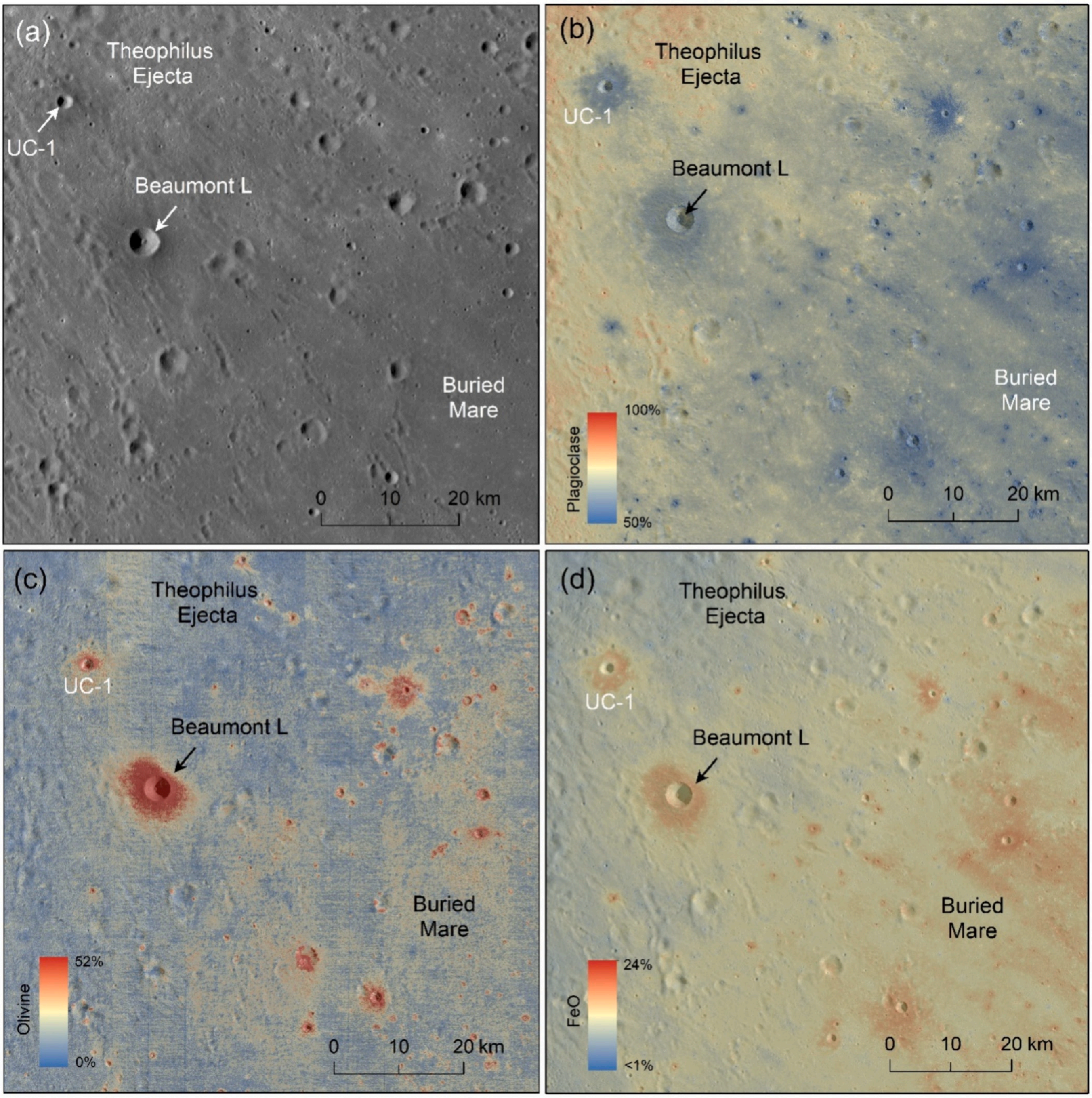

Fig. 32. (a) Kaguya TC image showing the halo bearing impact craters located on the south-eastern distal ejecta rays of Theophilus crater. Mineralogical abundance maps (in wt%) of the halo-bearing craters showing (b) plagioclase (c) olivine, and (d) FeO content, suggesting that the halo-bearing craters penetrated through the Theophilus ejecta and excavated the underlying mare basalt flows (crypto-mare).

in fine-grained and shocked highland crustal rock materials.

The Theophilus central peak exposes olivine, pyroxene and Mg-spinel lithologies, engulfed in the highland anorthositic rocks. These rocks may have originated from the bottom of the excavation zone, at ~8.2 or 2.5 km depth (AB section in Fig. 35). As suggested by Dhingra et al. (2011), a layer of Mg-suite mafic rocks containing olivine, pyroxene and Mg-spinel may have existed beneath Theophilus crater and were uplifted during impact and now exposed on the central peak. Considering the pre-impact target lithology in the central peak zone within a radius of 15 km, it is possible that the top layer of target may have composed of ~500 m thick mare basalt, underlain by highland anorthositic materials, including Mg-suite plutonic rocks, extending up to a depth 28 km (Fig. 35). As per the theoretical spallation model, the spall boulders do not form within the 15 km radius projectile contact zone, where hyper-velocity impact would have caused very high shock levels leading to melting and vapourization of both target and projectile (e.g., Melosh, 1984). Even if we assume that some spall boulders did form within 20 km radius from the impact point, their spall sizes would be of the orders of ~70 m, which would have ejected at <1 km/s velocity and higher ejection angles (~60°), and ballistically deposited at distance of >400 km outside Theophilus crater. Therefore, we suggest that the olivine basalt boulders present in the Shioli crater ejecta were originated near the edge of the Theophilus transient crater (31–37 km launch range). Considering the 2 Ga age of Theophilus crater, it is likely

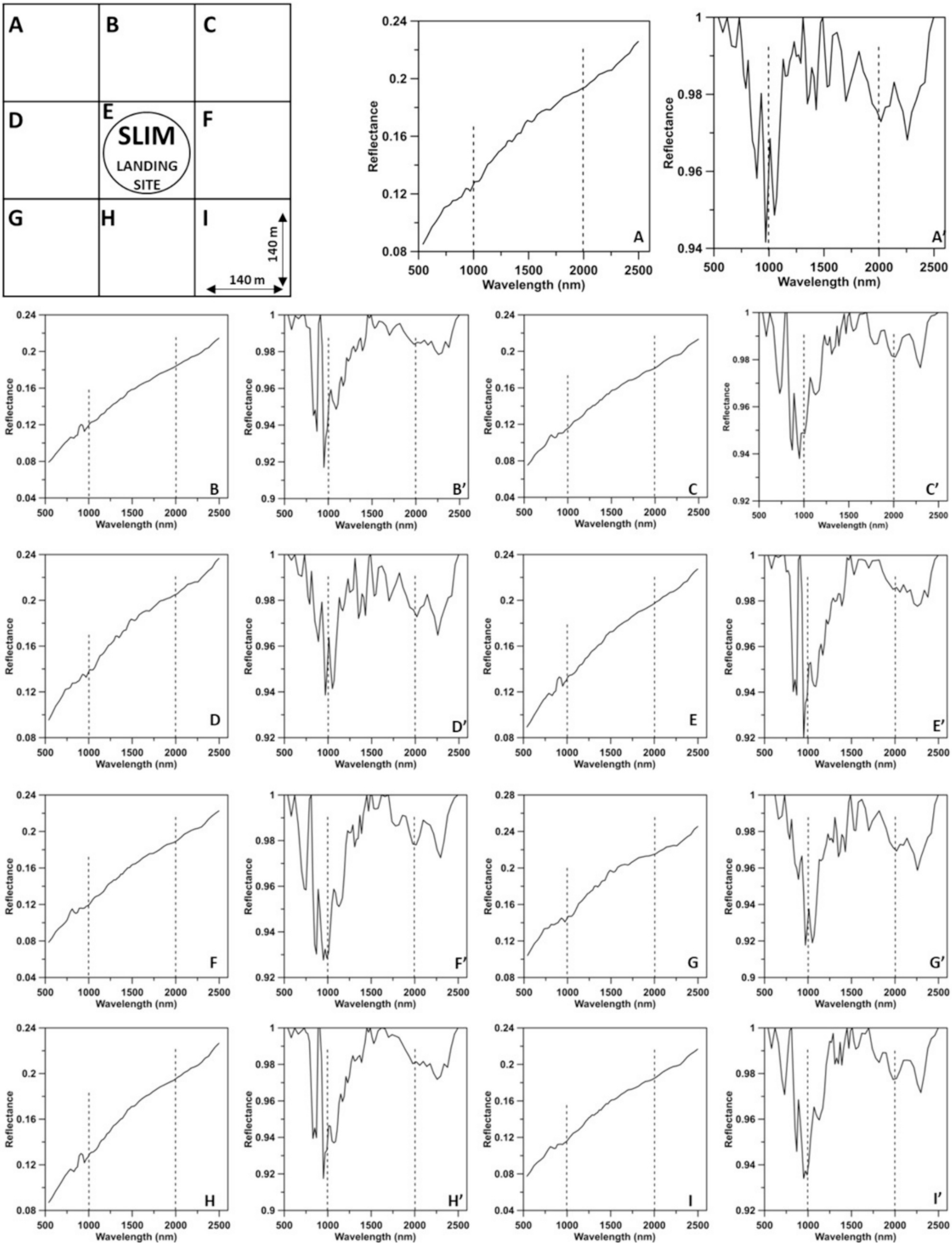

Fig. 33. The M^3 data analysis of 3 × 3 pixels covering the SLIM landing site which is divided into 9 pixels from A to I, and for each pixel, both reflectance spectrum and continuum-removed spectrum are provided.

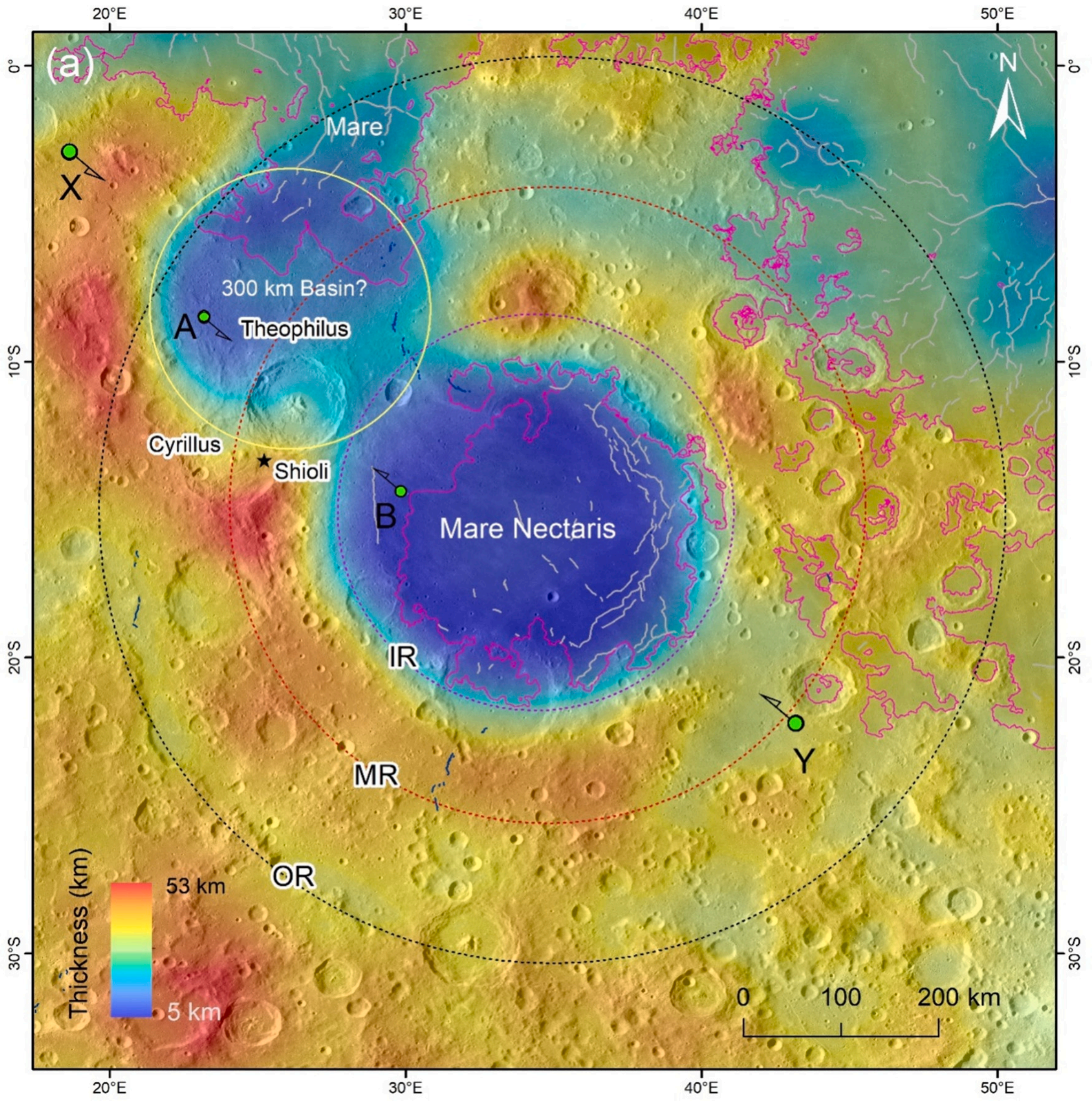

Fig. 34. The GRAIL crustal thickness map of Nectaris multi-ring basin showing Theophilus crater and Shioli crater. The crustal cross-sections across X-Y and A-B are shown in Fig. 35.

that the boulders exposed on the ejecta blanket surface would have been fully destroyed by the subsequent meteoroid impacts. On the other hand, the boulders buried in the ejecta blanket are survived now, as shown by the Arecibo radar data (Fig. 6). These buried boulders were subjected to the subsequent impact spallation due to the Shioli impact, which produced smaller boulders that became the part of Shioli crater ejecta. The SLIM mission has been investigating the composition of these Shioli boulders at the landing site.

5.3. *Implications for Apollo 16 samples*

The Apollo 16 is the only landing site that is located on the lunar highland. The samples collected from this site contain a variety of rock samples originated from different impact basins (Petro and Pieters, 2006). The previous studies showed that the geology of Apollo 16 landing site is largely influenced by the Nectaris basin materials (e.g., Spudis, 1984; Spudis et al., 1989). Zeigler et al. (2006) characterized one of the Apollo 16 samples, containing a coarse-grained high-aluminium basalt fragment (sample # 60053, 2–9) with 8.15% Al, 13.99% Fe and 2.05% Mg. The Mare Nectaris/Sinus Asperitatis (~220 km east of the landing site) was suggested to be the most likely source for this basaltic sample and one of the craters, Theophilus, Madler, and Torricelli could have ejected this basalt sample from the mare region. Fig. 36 shows the secondary craters of Theophilus crater that are distributed up to the radial distance of the Apollo 16 landing site, which is located about 325 km WNW of Theophilus crater. Considering the theoretical spallation model for Theophilus crater and its secondary crater distribution (Fig. 36), we suggest that the Mare Nectaris flows on top of the pre-impact target at the Theophilus impact site was the source for the Apollo 16 basalt sample. According to the model, ~80 m size basalt boulders were originated at a radial distance of 23 km from the impact point within the Theophilus transient crater, were ejected at a velocity of ~750 m/s, and ballistically deposited at the Apollo 16 landing site. Since 2 Ga, the basalt boulders at the landing site were subjected to further micro-meteoroid impacts and broke down into finer fragments (e.g., Basilevsky et al., 2013), one of which was found in the samples collected by the Apollo 16 crew.

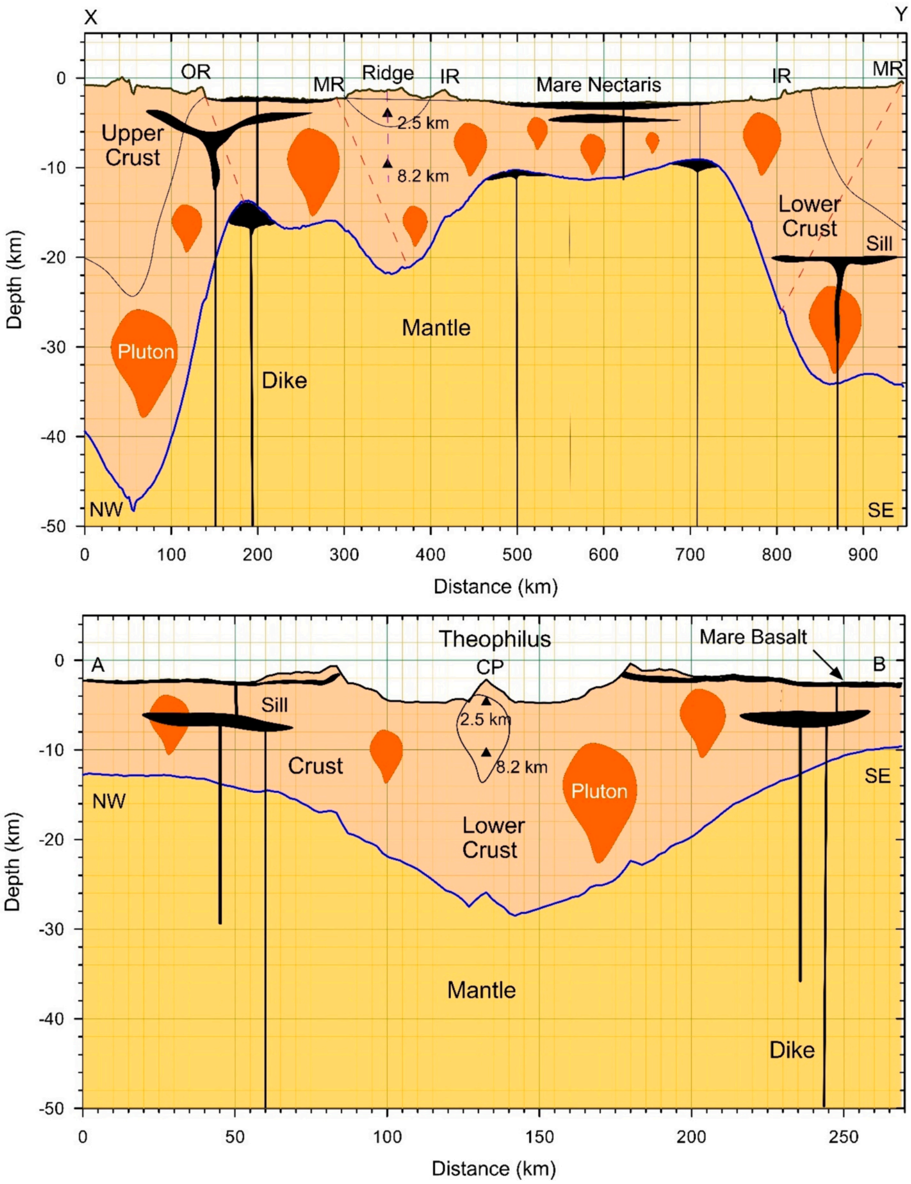

Fig. 35. The crustal cross-sections across X-Y (upper) and A-B (lower) showing the variation of surface topography and GRAIL crustal thickness across the Nectaris impact basin and Theophilus crater, respectively. The upper crust in the Nectaris basin interior was eroded by the basin forming impact event and that of a 300-km size impact basin (see Fig. 34). The Mg-suite plutons intruded the lower crust (orange blobs) and sills-like bodies fed-by dikes (black lines and sheets) are postulated to be the suppliers of mare basalt flows on the surface.

6. Conclusions

The present study leads to the following major conclusions:

1. For understanding the origin of Shioli crater and provenance of its ejecta boulders, we studied the geological setting of Theophilus crater and the host Nectaris multi-ring basin. Our mapping of >2000 secondary craters of Theophilus revealed their asymmetric distribution pointing to the northeast directed oblique impact event. Hundreds of secondary craters from other primary impact craters such as Madler, Copernicus and Aristillus criss-cross the Theophilus ejecta blanket.
2. The ejecta blanket thickness variation around Theophilus crater was modelled. The age of Theophilus crater was determined using the conventional crater counting method that yielded 2 ± 0.25 Ga, suggesting that it is an Eratosthenian crater. This finding is contrary to Fortezzo et al. (2020) but is consistent with Wilhelms (1987).
3. The Arecibo radar data analysis suggested that the Theophilus ejecta contains abundant buried ejecta boulders, while those boulders on the ejecta surface were completely destroyed since Theophilus formation, in the last 2 billion years. The abundant boulder fields, boulder falls and debris flows in and around the Theophilus central peak points to recent surface modification in the crater.
4. The Chandrayaan-2 CLASS data provided the elemental maps of Al, Mg and Fe for the study area, which suggested the presence of high aluminium mare basalt flows in Mare Nectaris and around Theophilus crater. These maps also delineated the highland-mare contact in the study area and the presence of anorthosite and mafic-rich highland rock units in the northwestern Nectaris basin. The crater interior of Thophilus and Madler expose

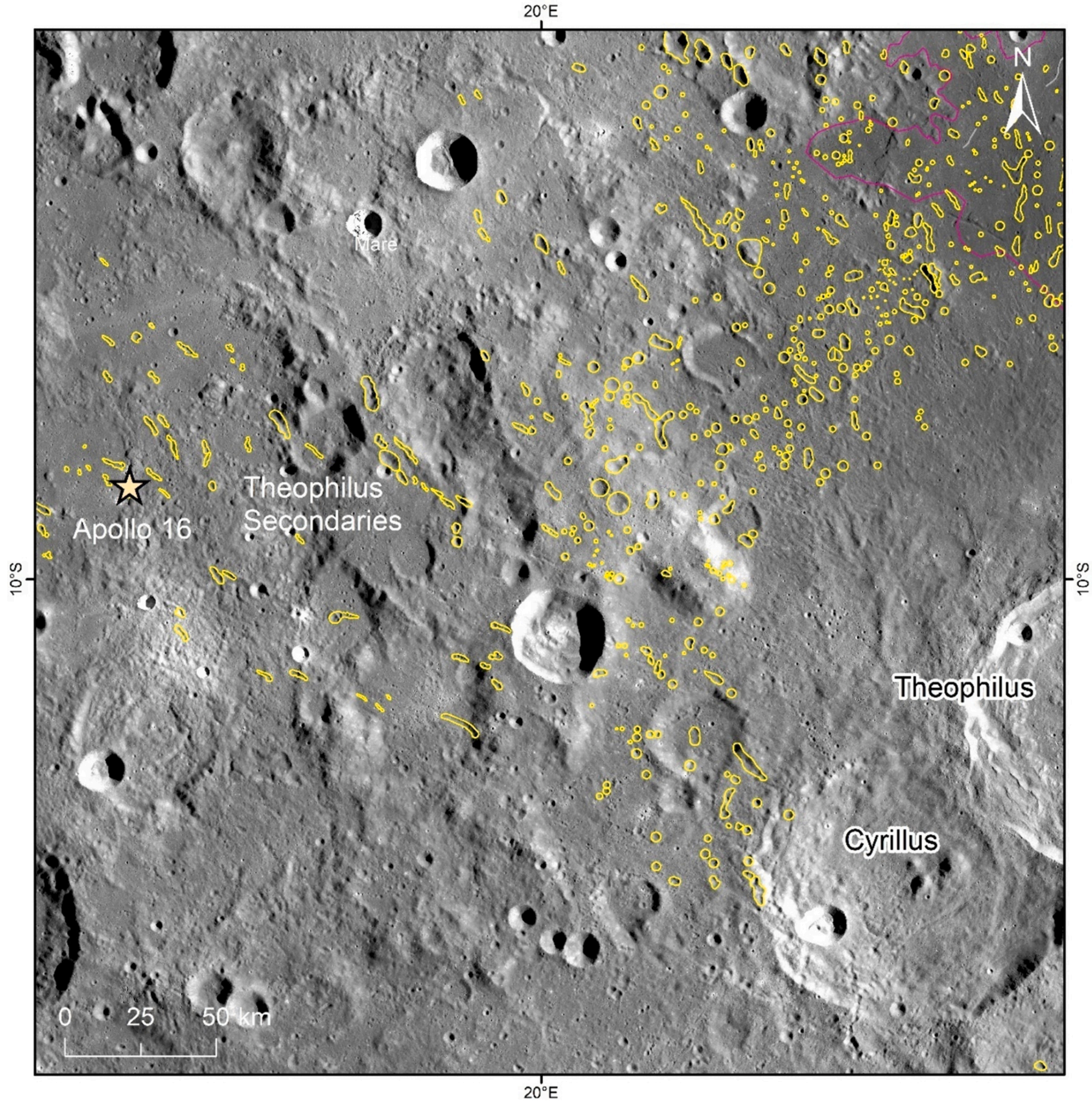

Fig. 36. The Kaguya TC image mosaic showing the distribution of secondary craters of Theophilus crater up to the Apollo 16 landing site.

highland anorthositic bedrocks mixed with some mafic rocks (including olivine bearing mare basalts).

5. The pre-impact target in the excavation zone of Theophilus crater was composed of ~500 m thick olivine basalt top-layer, underlain by a layer of ~400–10 m thick Cyrillus anothositic ejecta blanket. Below these two layers, middle to lower crustal anorthositic highland crust coated with the Nectaris basin ejecta and impact melt sheets on the top, was present. These rock materials were excavated by the Theophilus impact and became the part of fragmental ejecta blanket layer of Theophilus crater.
6. Shioli impact crater is located on the uprange ejecta blanket of Theophilus crater. We characterized the Shioli crater interior and exterior (surrounding ejecta) and mapped >2300 large ejecta boulders (≥1.5 m) and > 7800 small ejecta boulders (<1.5 m), and measured their sizes and shapes. The asymmetric dispersal pattern of ejecta blanket and ejecta boulders surrounding Shioli crater points to ESE directed oblique impact. The dating of Shioli crater ejecta blanket using the conventional crater counting method yielded ~1 Ma formation age for the crater.
7. The Shioli ejecta boulders show spatial variation of size and shape with more concentration of larger boulders near the crater rim and gradual radial decrease of size and aspect ratio outward from the crater rim. The observed ejecta boulder size varies between 12.4 and 1.5 m, while the aspect ratio varies between 2.6 and 1. The SLIM mission landed 775 m ENE of Shioli crater, where less than a meter thick Shioli ejecta may be present, and contain fewer large-size boulders.
8. The size distribution of Shioli ejecta boulders suggests that the host crater was formed by a primary impact event. The observed boulder sizes are consistent with a theoretical spallation model, in which a ~ 3 m diameter basaltic projectile impacted the Theophilus ejecta at a velocity of 16 km/s. The physical properties of fragmental target (density: 1500 kg/m^3; compressional wave velocity: 800 m/s; dynamic tensile strength: 27 MPa) best explains the observed Shioli boulder sizes.
9. The theoretical spallation model for Shioli crater provided the maximum boulder diameter near the crater rim to be 12.5 m, which is similar to the maximum observed boulder diameter of 12.4 m. Though the theoretical boulder sizes broadly match with the observed boulder sizes, a majority of boulders in the ejecta are smaller than the theoretical values, indicating more complex fragmentation and size reduction during emplacement, ballistic

transport and deposition. It is consistent with a larger b-value (−4.06) provided by the cumulative size-frequency distribution of Shioli boulders. We suggest that the Shioli boulders were produced from the complex impact fragmentation of already existing buried Theophilus ejecta boulders.

10. The Shioli ejecta boulders are composed of olivine basalt (Mare Nectaris) and highland anorthositic fragments, including reworked Cyrillus ejecta. Fragments of Nectaris ejecta and impact melt materials may also be incorporated in the Shioli ejecta. These reflect the composition of the underlying buried Theophilus ejecta boulders underneath Shioli crater.
11. The regional crustal structure of Nectaris basin and Theophilus crater and the petrological make-up suggest that Theophilus crater did not excavate the lunar mantle. Therefore, the Shioli boulders are of crustal origin. The predominant olivine minerals present in the Shioli ejecta boulders may belong to the olivine bearing Mare Nectaris, but these materials may be mixed with highland rock materials including Mg-suite mafic rocks.
12. The map of secondary craters of Theophilus crater suggests that its crater materials ballistically deposited at the Apollo 16 landing site and the basalt sample (60,053, 2–9) recovered by the Apollo crew was originally originated from the Mare Nectaris by Theophilus impact event at ~2 Ga ago.

CRediT authorship contribution statement

P. Senthil Kumar: Writing – review & editing, Writing – original draft, Methodology, Investigation, Formal analysis. **Abhisek Mishra:** Writing – review & editing, Writing – original draft, Methodology, Investigation, Formal analysis, Data curation. **Vivek Krishnan:** Writing – review & editing, Writing – original draft, Investigation, Formal analysis, Data curation. **Netra S. Pillai:** Writing – review & editing, Writing – original draft, Methodology, Investigation, Formal analysis, Data curation. **Sumit Pathak:** Writing – review & editing, Writing – original draft, Methodology, Investigation, Formal analysis, Data curation. **Sriram S. Bhiravarasu:** Writing – review & editing, Writing – original draft, Methodology, Investigation, Formal analysis, Data curation. **Shyama Narendranath:** Writing – review & editing, Writing – original draft, Investigation, Formal analysis. **K. Jaya Prasanna Lakshmi:** Writing – review & editing, Writing – original draft, Investigation, Formal analysis. **Satadru Bhattacharya:** Writing – review & editing, Writing – original draft, Investigation, Formal analysis.

Declaration of competing interest

The authors declare that they have no known competing financial interests or personal relationships that could have appeared to influence the work reported in this paper.

Data availability statement

The Lunar Reconnaissance Orbiter Camera (LROC) Wide Angle Camera (WAC) and Narrow Angle Camera (NAC) images and Lunar Orbiter Laser Altimeter (LOLA) and SLDEM topographic data used in this paper are available at NASA Planetary Data System Geosciences Node at Washington University at St. Louis (https://pds-geosciences.wustl.edu/dataserv/moon.html) and the United States Geological Survey (https://pilot.wr.usgs.gov/) website. The Chandrayaan-1 Moon Mineralogy Mapper (M3) data, Chandrayaan 2 Large Area Soft X-ray Spectrometer (CLASS) calibrated data and Orbiter High Resolution Camera (OHRC) images can be downloaded from the ISRO website (https://pradan.issdc.gov.in/ch2/protected/payload.xhtml). The Kaguya (SELENE) Terrain Camera (TC) images and Kaguya Mineral maps used in this paper is available in SELENE Data Archive website (https://darts.isas.jaxa.jp/planet/pdap/selene/index.html.en). The Gravity Recovery and Interior Laboratory (GRAIL) crustal thickness data used in this work is taken from Wieczorek et al. (2013). The original data generated in this work are available freely in Kumar et al. (2024).

Acknowledgements

P. Senthil Kumar acknowledges Council of Scientific & Industrial Research (India) for financial support. Abhisek Mishra acknowledges JRF/SRF Fellowship offered by Council of Scientific & Industrial Research (India) and Vivek Krishnan acknowledges the INSPIRE Fellowship offered by Department of Science & Technology, Government of India. Prakash Kumar, Director, CSIR-NGRI is thanked for granting permission to publish this paper (Ref. No. NGRI/Lib/2024/Pub-77). R.P. Rajasekhar is acknowledged for providing the crustal thickness map. The authors thank the editor Brandon Johnson and two reviewers, including Joseph Boyce, for useful suggestions. The authors also thank Makkio Ohtake for a generous and insightful discussion on the preliminary results from the SLIM mission.

Appendix A. Supplementary data

Supplementary data to this article can be found online at https://doi.org/10.1016/j.icarus.2024.116239.

References

Austin, T., Mark Robinson, M., Mahanti, P., 2024. Ejecta blankets at small craters on the Moon. Planet. Sci. J. 5, 114.

Baldwin, R.B., 1974. On the accretion of the Earth and Moon. Icarus 23, 97–107.

Baldwin, R.B., 1987. On the relative and absolute ages of seven lunar front face basins. I. From viscosity arguments. Icarus 71, 1–18.

Barker, M.K., Mazarico, E., Neumann, G.A., Zuber, M.T., Haruyama, J., Smith, D.E., 2016. A new lunar digital elevation model from the lunar orbiter laser altimeter and SELENE terrain camera. Icarus 273, 346–355. https://doi.org/10.1016/j.icarus.2015.07.039.

Bart, G.D., Melosh, H.J., 2007. Using lunar boulders to distinguish primary from distant secondary impact craters. Geophys. Res. Lett. 34, L07203. https://doi.org/10.1029/2007GL029306.

Bart, G.D., Melosh, H.J., 2010. Distribution of boulders ejected from lunar craters. Icarus 209, 337–357. https://doi.org/10.1016/j.icarus.2010.05.023.

Basilevsky, A.T., Head, J.W., Horz, F., 2013. Survival times of meter-sized boulders on the surface of the Moon. Planet. Space Sci. 89, 118–126. https://doi.org/10.1016/j.pss.2013.07.011.

Bhattacharya, S., Lal, D., Chauhan, M., Chauhan, P., Ajai, Kiran Kumar, A.S., 2015. Detection of hydroxyl-bearing exposures of possible magmatic origin on the central peak of crater Theophilus using Chandrayaan-1 Moon Mineralogy Mapper (M3) data. Icarus 260, 167–173. https://doi.org/10.1016/j.icarus.2015.07.013.

Campbell, B.A., Hawke, B.R., 2005. Radar mapping of lunar cryptomaria east of Orientale basin. J. Geophys. Res. 110, E09002. https://doi.org/10.1029/2005JE002425.

Campbell, B.A., Campbell, D.B., Margot, J.L., Ghent, R.R., et al., 2007. Focused 70-cm wavelength radar mapping of the moon. IEEE Trans. Geosci. Remote Sens. 45 (12), 4032–4042. Dec. 2007. https://doi.org/10.1109/TGRS.2007.906582.

Campbell, B.A., Carter, L.M., Campbell, D.B., Nolan, M., Chandler, J., Ghent, R.R., Hawke, B.R., Anderson, R.F., Wells, K., 2010. Earth-based 12.6-cm wavelength radar mapping of the moon: new views of impact melt distribution and mare physical properties. Icarus 208 (2), 565–573. https://doi.org/10.1016/j.icarus.2010.03.011.

Chowdhury, A.R., Saxena, M., Kumar, A., Joshi, S.R., Amitabh, Dagar, Mittal, M., Kirkire, S., Desai, J., Shah, D., Karelia, J.C., Kumar, A., Jha, K., Das, P., Bhagat, H.V., Sharma, J., Ghonia, D.N., Desai, M., Bansal, G., Gupta, A., 2020. Orbiter high resolution camera onboard Chandrayaan-2 orbiter. Curr. Sci. 118 (4), 560–565. https://www.jstor.org/stable/27138702.

Corley, L.M., McGovern, Patrick J., Kramer, G.Y., et al., 2018. Olivine-bearing lithologies on the Moon: constraints on origins and transport mechanisms from M^3 spectroscopy, radiative transfer modeling, and GRAIL crustal thickness. Icarus 300, 287–304. https://doi.org/10.1016/j.icarus.2017.09.012, 15 January 2018.

De Hon, R.A., 1974. Thickness of mare material in the Tranquillitatis and Nectaris basins. In: Proc. Lunar Sci. Conf. 5th, Vol.1, pp. 53–59.

Dhingra, D., Pieters, C.M., Boardman, J.W., Head, J.W., Isaacson, P.J., Taylor, L.A., 2011. Compositional diversity at Theophilus Crater: understanding the geological context of Mg-spinel bearing central peaks. Geophys. Res. Lett. 38, L11201. https://doi.org/10.1029/2011GL047314.

Elkins-Tanton, L.T., Burgess, S., Yin, Q.Z., 2011. The lunar magma ocean: reconciling the solidification process with lunar petrology and geochronology. Earth Planet. Sci. Lett. 304 (3–4), 326–336. https://doi.org/10.1016/j.epsl.2011.02.004.

Fortezzo, C.M., Spudis, P.D., Harrel, S.L., 2020. Release of the digital unified global geologic map of the moon At 1:5,000,000- scale. In: 51st Lunar and Planetary Science Conference. Lunar and Planetary Institute, Houston, TX. https://www.hou.usra.edu/meetings/lpsc2020/pdf/2760.pdf.

Ghent, R.R., Leverington, D.W., Campbell, B.A., Hawke, B.R., Campbell, D.B., 2005. Earth-based observations of radar-dark crater haloes on the Moon: implications for regolith properties. J. Geophys. Res. 110, E02005. https://doi.org/10.1029/2004JE002366.

Goswami, J.N., Annadurai, M., 2009. Chandrayaan-1: India's first planetary science mission to the moon. Curr. Sci. 96 (4), 486–491. https://www.jstor.org/stable/24105456.

Green, R.O., Pieters, C., Mouroulis, P., Eastwood, M., et al., 2011. The Moon Mineralogy Mapper (M^3) imaging spectrometer for lunar science: Instrument description, calibration, on-orbit measurements, science data calibration and on-orbit validation. J. Geophys. Res. 116 https://doi.org/10.1029/2011JE003797. E00G19.

Haruyama, J., Matsunaga, T., Ohtake, M., et al., 2008. Global lunar-surface mapping experiment using the Lunar Imager/Spectrometer on SELENE. Earth Planet Sp. 60, 243–255. https://doi.org/10.1186/BF03352788.

Head, J.W., Wilson, L., 2017. Generation, ascent and eruption ofmagma on the Moon: 837 new insights into source depths, magma supply, intrusions and effusive/explosive eruptions (part 2: 838 predicted emplacement processes and observations). Icarus 283. https://doi.org/10.1016/j.icarus.2016.05.031, 176 223. 839.

Head, J.W., Wilson, L., Hiesinger, H., van der Bogert, C.H., Chen, Y., Dickson, J.L., Gaddis, L.R., Haruyama, J., Jawin, E.R., Jozwiak, L.M., Li, C., Liu, J., Morota, T., Needham, D.H., Ostrach, L.R., Pieters, C.M., Prissel, T.C., Qian, Y., Qiao, L., Rutherford, M.R., Scott, D.R., Whitten, J.L., Xiao, L., Zhang, F., Ziyuan, O., 2023. Lunar Mare basaltic volcanism: volcanic features and emplacement processes. Rev. Mineral. Geochem. 89 (1), 453–507. https://doi.org/10.2138/rmg.2023.89.11.

Hiesinger, H., Jaumann, R., Neukum, G., Head III, J.W., 2000. Ages of mare basalts on the lunar nearside. J. Geophys. Res. 105 (E12), 29239–29275. https://doi.org/10.1029/2000JE001244.

Hiesinger, H., Head III, J.W., Wolf, U., Jaumann, R., Neukum, G., 2011. Ages and stratigraphy of lunar mare basalts: a synthesis. Spec. Pap. Geol. Soc. Am. 477, 1–51. https://doi.org/10.1130/2011.2477(01).

Housen, K.R., Schmidt, R.M., Holsapple, K.A., 1983. Crater ejecta scaling laws: fundamental forms based on dimensional analysis. J. Geophys. Res. Solid Earth 88 (B3), 2485–2499. https://doi.org/10.1029/JB088iB03p02485.

Ivanov, M.A., Abdrakhimov, A.M., Basilevsky, A.T., Demidov, N.E., Guseva, E.N., Head, J.W., Hiesinger, H., Kohanov, A.A., Krasilnikov, S.S., 2018. Geological characterization of the three high-priority landing sites for the Luna-Glob mission. Planet. Space Sci. 162, 190–206. https://doi.org/10.1016/j.pss.2017.08.004.

Jeffrey Taylor, G., Warren, P., Ryder, G., Delano, J., Pieters, C., Lofgren, G., 1991. Lunar Rocks. Lunar Sourcebook, A User's Guide to the Moon. Cambridge University Press, pp. 183–284.

Kaur, P., Chauhan, P., Rajawat, A.S., Kiran Kumar, A.S., 2015. Study of olivine-rich dark halo crater – Beaumont L in Mare Nectaris using high resolution remote sensing data. Planet. Space Sci. 109–110, 92–105. https://doi.org/10.1016/j.pss.2015.02.001.

Kneissl, T., Gasselt, S.V., Neukum, G., 2011. Map-projection-independent crater size-frequency determination in GIS environments—new software tool for ArcGIS. Planet. Space Sci. 59 (11–12), 1243–1254. https://doi.org/10.1016/j.pss.2010.03.015.

Kramer, G.Y., Jolliff, B.L., Neal, C.R., 2008. Distinguishing high-alumina mare basalts using Clementine UVVIS and Lunar Prospector GRS data: Mare Moscoviense and Mare Nectaris. J. Geophys. Res. 113, E01002. https://doi.org/10.1029/2006JE002860.

Krasilnikov, S.S., Ivanov, M.A., Head, J.W., Krasilnikov, A.S., 2023. Geologic history of the south circumpolar region (SCR) of the Moon. Icarus 394, 115422. https://doi.org/10.1016/j.icarus.2022.115422.

Krishna, N., Kumar, P.S., 2016. Impact spallation processes on the Moon: a case study from the size and shape analysis of ejecta boulders and secondary craters of Censorinus crater. Icarus 264, 274–299. https://doi.org/10.1016/j.icarus.2015.09.033.

Kumar, P.S., Prasanna Lakshmi, K.J., Krishna, N., Menon, R., Sruthi, U., Keerthi, V., Sen, M.K., 2014. Impact fragmentation of Lonar Crater, India: implications for impact cratering processes in basalt. J. Geophys. Res. Planets 119 (9), 2029–2059. https://doi.org/10.1002/2013JE004543.

Kumar, P.S., Sruthi, U., Krishna, N., Lakshmi, K.J.P., Menon, R.A., et al., 2016. Recent shallow moonquake and impact-triggered boulder falls on the Moon: new insights from the Schrödinger basin. J. Geophys. Res. Planets 121, 147–179. https://doi.org/10.1002/2015JE004850.

Kumar, P.S., Mishra, A., Krishnan, V., 2024. The dataset for the Icarus paper "crustal origin for olivine in the lunar Shioli crater ejecta boulders: insights from the geological setting of Theophilus crater and Nectaris basin" [dataset]. Zenodo. https://doi.org/10.5281/zenodo.12163230.

Lakshmi, K.J.P., Kumar, P.S., 2020. Physical properties of basalt ejecta boulders at Lonar crater, India: insights into the target heterogeneity and impact spallation processes in basalt with application to Mars. J. Geophys. Res. Planets 125. https://doi.org/10.1029/2020JE006593 e2020JE006593.

Lemelin, M., Lucey, P.G., Miljković, K., Gaddis, L.R., Hare, T.M., Ohtake, M., 2019. The compositions of the lunar crust and upper mantle: spectral analysis of the inner rings of lunar impact basins. Planet. Space Sci. 165, 230–243. https://doi.org/10.1016/j.pss.2018.10.003.

Lucey, P.G., 2004. Mineral maps of the Moon. Geophys. Res. Lett. 31, L08701. https://doi.org/10.1029/2003GL019406.

McGetchin, T.R., Settle, M., Head, J.W., 1973. Radial thickness variation in impact crater ejecta: implications for lunar basin deposits. Earth Planet. Sci. Lett. 20 (2), 226–236. https://doi.org/10.1016/0012-821X(73)90162-3.

McKay, D.S., Heiken, G., Basu, A., Blanford, G., Simon, S., Reedy, R., French, B.M., Papike, J., 1991. The lunar regolith, in Lunar Sourcebook edited by Grant H. Heiken, David T. Vaniman, Bevan M. French, pp. 285–356.

Melosh, H.J., 1984. Impact ejection, spallation, and the origin of meteorites. Icarus 59 (2), 234–260. https://doi.org/10.1016/0019-1035(84)90026-5.

Melosh, H.J., 1989. Impact Cratering: A Geologic Process, vol. 245. Oxford Univ. Press, New York.

Meyer, H.M., Denevi, B.W., Robinson, M.S., Boyd, A.K., 2020. Impact ejection, spallation, and the origin of meteorites. Icarus 125, e2019JE006073. https://doi.org/10.1029/2019JE006073.

Michael, G.G., Neukum, G., 2010. Planetary surface dating from crater size–frequency distribution measurements: partial resurfacing events and statistical age uncertainty. Earth Planet. Sci. Lett. 294 (3–4), 223–229. https://doi.org/10.1016/j.epsl.2009.12.041.

Mohanty, R., Kumar, P.S., Raghukanth, S.T.G., Lakshmi, K.J.P., 2020. The long-lived and recent seismicity at the lunar Orientale Basin: evidence from morphology and formation ages of Boulder avalanches, tectonics, and seismic ground motion. J. Geophys. Res. Planets 125. https://doi.org/10.1029/2020JE006553 e2020JE006553.

Mohanty, R., Senthil Kumar, P., Lakshmi, K.J.P., Krishnan, V., Mishra, A., Karthik, G.S.S., 2023. Evidence for trail forming ejecta boulder falls around fresh simple impact craters at the lunar Orientale multi-ring basin and implications for ballistic ejecta sedimentation on the Moon. Icarus 405, 115723. https://doi.org/10.1016/j.icarus.2023.115723.

Moriarty III, D.P., Pieters, C.M., 2018. The character of South Pole-Aitken Basin: patterns of surface and subsurface composition. J. Geophys. Res. Planets 123, 729–747. https://doi.org/10.1002/2017JE005364.

Mustard, J.F., Pieters, C.M., Isaacson, P.J., Head, J.W., et al., 2011. Compositional diversity and geologic insights of the Aristarchus crater from Moon Mineralogy Mapper data. J. Geophys. Res. 116, E00G12 https://doi.org/10.1029/2010JE003726.

Nakauchi, Y., Saiki, K., Ohtake, M., Shiraishi, H., Honda, C., Sato, H., Ishihara, Y., Maeda, T., Otsuki, M., Sakai, S., Sawai, S., Fukuda, S., Kushiki, K., Arakawa, T., 2019. Multi-band camera on SLIM to investigate Mg# of lunar mantle materials. In: 50th Lunar and Planetary Science Conference#1522.

Narendranath, S., Pillai, N.S., Bhatt, M., Vadodariya, K., Vatedka, R., Tadepalli, S.P., Sarwade, A., Tyagi, A., Sharan, V., 2024. Lunar elemental abundances as derived from Chandrayaan-2. Icarus 410, 115898. https://doi.org/10.1016/j.icarus.2023.115898.

Neukum, G., 1983. Meteoritenbombardement und Datierung planetarer Oberfl ächen, Habilitationsschrift. Universität München, München, Germany, 186 p. https://search.worldcat.org/en/title/258552255.

Neukum, G., Ivanov, B.A., 1994. Crater size distributions and impact probabilities on earth from lunar, terrestrial planet, and asteroid cratering data. In: Gehrels, T. (Ed.), Hazards Due to Comets and Asteroids. Univ. Arizona Press, Tucson, pp. 359–416.

Neukum, G., Ivanov, B.A., Hartmann, W.K., 2001. Cratering records in the inner solar system in relation to the lunar reference system. Space Sci. Rev. 96 (1–4), 55–86. https://doi.org/10.1023/A:1011989004263.

Ohtake, M., Matsunaga, T., Haruyama, J., et al., 2009. The global distribution of pure anorthosite on the Moon. Nature 461, 236–240. https://doi.org/10.1038/nature08317.

Ohtake, M., Saiki, K., Nakauchi, Y., Shiraishi, H., Ishihara, Y., Sato, H., Honda, C., Maeda, T., Sakai, S., Sawai, S., Fukuda, S., Kushiki, K., 2019. Geology of the crater Theophilus on the moon: landing site of the smart lander for investigating the Moon. In: 50th Lunar and Planetary Science Conference#2342.

Petro, N.E., Pieters, C.M., 2006. Modeling the provenance of the Apollo 16 regolith. J. Geophys. Res. 111, E09005. https://doi.org/10.1029/2005JE002559.

Pieters, C.M., Besse, S., Boardman, J., Buratti, B., Cheek, L., Clark, R.N., Combe, J.P., Dhingra, D., Goswami, J.N., Green, R.O., et al., 2011. Mg-spinel lithology: a new rock type on the lunar farside. J. Geophys. Res. Planets 116. https://doi.org/10.1029/2010JE003727. E00G08.

Pieters, C.M., Hanna, K.D., Cheek, L., Dhingra, D., Prissel, T., Jackson, C., Moriarty, D., Parman, S., Taylor, L.A., 2014. The distribution of Mg-spinel across the Moon and constraints on crustal origin. Am. Mineral. 99 (10), 1893–1910. https://doi.org/10.2138/am-2014-4776.

Pike, R.J., 1974. Ejecta from large craters on the Moon: comments on the geometric model of McGetchin et al. Earth Planet. Sci. Lett. 23 (3), 265–271. https://doi.org/10.1016/0012-821X(74)90114-9.

Potter, R.W.K., Collins, G.S., Kiefer, W.S., McGovern, P.J., Kring, D.A., 2012. Constraining the size of the South Pole-Aitken basin impact. Icarus 220 (2), 730–743. https://doi.org/10.1016/j.icarus.2012.05.032.

Prettyman, T.H., Hagerty, J.J., Elphic, R.C., Feldman, W.C., Lawrence, D.J., McKinney, G.W., Vaniman, D.T., 2006. Elemental composition of the lunar surface: analysis of gamma ray spectroscopy data from Lunar Prospector. J. Geophys. Res. Planets 111, E12007. https://doi.org/10.1029/2005JE002656.

Radhakrishna, V., Tyagi, A., Narendranath, S., Vadodariya, K., Yadav, R., Singh, B., Balaji, G., Satya, N., Shetty, A., Kumar, H.N.S., Kumar, Vaishali, Pillai, N.S., Tadepalli, S., Raghavendra, V., Sreekumar, P., Agarwal, A., Valarmathi, N., 2020. Chandrayaan-2 large area soft X-ray spectrometer. Curr. Sci. 118 (2), 219–225. https://www.jstor.org/stable/27226324.

Richardson, J.E., Abramov, O., 2020. Modeling the formation of the lunar upper Megaregolith layer. Planet. Sci. J. 1 (2) https://doi.org/10.3847/PSJ/ab7235, 18pp.

Robinson, M.S., Brylow, S.M., Tschimmel, M., Humm, D., Lawrence, S.J., Thomas, P.C., et al., 2010. Lunar reconnaissance orbiter camera (LROC) instrument overview. Space Sci. Rev. 150 (1–4), 81–124. https://doi.org/10.1007/s11214-010-9634-2.

Saiki, K., Ohtake, M., Nakauchi, Y., Shiraishi, H., Ishihara, Y., Sato, H., Honda, C., Maeda, T., Yamanaka, C., Nagoka, H., Sakai, S., Sawai, S., Fukuda, S., Kushiki, K., Ebizuka, N., Sasaki, M., Okamoto, T., Kayama, M., Demura, M., Kitazato, K., Ogawa, Y., Mikouchi, T., Hirano, T., 2021. Development of two types of NIR spectral camera for lunar missions SLIM and LUPEX. 52nd Lunar and Planetary Science Conference #2303.

Sharpton, V.L., 2014. Outcrops on lunar crater rims: implications for rimconstruction mechanisms, ejecta volumes and excavation depths. J. Geophys. Res. Planets 119, 154–168. https://doi.org/10.1002/2013JE004523.

Shearer, C.K., Elardo, S.M., Petro, N.E., Borg, L.E., McCubbin, F.M., 2015. Origin of the lunar highlands mg-suite: an integrated petrology, geochemistry, chronology, and remote sensing perspective. Am. Mineral. 100 (1), 294–325. https://doi.org/10.2138/am-2015-4817.

Spudis, P.D., 1984. Apollo 16 site geology and impact melts: implications for the geologic history of the lunar highlands. J. Geophys. Res. 89 (S01), C95–C107. https://doi.org/10.1029/JB089iS01p00C95.

Spudis, P.D., Hawke, B.R., Lucey, P.G., 1989. Geology and deposits of the Lunar Nectaris basin. In: Proceedings of the 19th Lunar and Planetary Science Conference, pp. 51–59.

Spudis, P.D., Martin, D.J.P., Kramer, G., 2014. Geology and composition of the Orientale Basin impact melt sheet. J. Geophys. Res. Planets 119, 19–29. https://doi.org/10.1002/2013JE004521.

Stöffler, D., Ryder, G., 2001. Stratigraphy and isotope ages of lunar geologic units: chronological standard for the inner solar system. Space Sci. Rev. 96, 9–54. https://doi.org/10.1023/A:1011937020193.

Thompson, T.W., 1987. High-resolution lunar radar map at 70 cm wave-length. Earth Moon Planet. 37, 59–70. https://doi.org/10.1007/BF00054324.

Thompson, T.W., Ustinov, E.A., Heggy, E., 2011. Modeling radar scattering from icy lunar regoliths at 13 cm and 4 cm wavelengths. J. Geophys. Res. 116, E01006. https://doi.org/10.1029/2009JE003368.

Tompkins, S., Pieters, C.M., 1999. Mineralogy of the lunar crust: results from Clementine. Meteorit. Planet. Sci. 34, 25–41. https://doi.org/10.1111/j.1945-5100.1999.tb01729.x.

Vaughan, W.M., Head, J.W., Wilson, L., Hess, P.C., 2013. Geology and petrology of enormous volumes of impact melt on the Moon: A case study of the Orientale basin impact melt sea. Icarus 223, 749–765. https://doi.org/10.1016/j.icarus.2013.01.017.

Wang, Y., Xiao, Z., Ma, P., Ouyang, H., Cao, W., 2024. Geological context of the SLIM landing site. J. Earth Sci. 35, 708–711. https://doi.org/10.59717/j.xinn-geo.2023.100014.

Whitford-Stark, J., 1981. The evolution of the lunar nectaris multiring basin. Icarus 48, 393–427. https://doi.org/10.1016/0019-1035(81)90053-1.

Wieczorek, M.A., Neumann, G.A., Nimmo, F., Kiefer, W.S., Jeffrey, G., et al., 2013. The crust of the moon as seen by GRAIL. Science 339, 671–675. https://doi.org/10.1126/science.1231530.

Wilhelms, D.E., 1987. The geologic history of the Moon. US Geol. Surv. Prof. Pap. 1348, 302.

Yamamoto, S., Nakamura, R., Matsunaga, T., et al., 2010. Possible mantle origin of olivine around lunar impact basins detected by SELENE. Nat. Geosci. 3, 533–536. https://doi.org/10.1038/ngeo897.

Yamamoto, S., Nagaoka, H., Ohtake, M., Kayama, M., Karouji, Y., Ishihara, Y., Haruyama, J., 2023. Lunar mantle composition based on spectral and geologic analysis of low-Ca pyroxene- and olivine-rich rocks exposed on the lunar surface. J. Geophys. Res. Planets 128. https://doi.org/10.1029/2023JE007817 e2023JE007817.

Yue, Z., Johnson, B.C., Minton, D.A., Melosh, H.J., Di, K., Hu, W., Liu, Y., 2013. Projectile remnants in central peaks of lunar impact craters. Nat. Geosci. 6 (6), 435–437. https://doi.org/10.1038/ngeo1828.

Zeigler, R.A., Korotev, R.L., Haskin, L.A., Jollif, B.L., Gillis, J.J., 2006. Petrography and geochemistry of five new Apollo 16 mare basalts and evidence for post-basin deposition of basaltic material at the site. Meteorit. Planet. Sci. 41, 263–284. https://doi.org/10.1111/j.1945-5100.2006.tb00209.x.

Zuber, M.T., Smith, D.E., Neumann, G.A., Goossens, S., Andrews-Hanna, J.C., Head, J.W., et al., 2016. Gravity field of the Orientalebasin from the gravity recovery and interior laboratory mission. Science 354 (6311), 438–441. https://doi.org/10.1126/science.aag0519.